

The Pennsylvania State University

The Graduate School

Department of Geosciences

SOIL CARBON DIOXIDE FLOW ASSOCIATED WITH
THE SAN ANDREAS AND CALAVERAS FAULTS,
CALIFORNIA

A Thesis in

Geosciences

by

Jennifer L. Lewicki

Submitted in Partial Fulfillment
of the Requirements
for the Degree of

Doctor of Philosophy

May 2002

We approve the thesis of Jennifer L. Lewicki.

Date of Signature

Susan L. Brantley
Professor of Geosciences
Thesis Adviser
Chair of Committee

Lee R. Kump
Professor of Geosciences

Michael A. Arthur
Professor of Geosciences

Derek Elsworth
Professor of Energy and Geo-Environmental Engineering

Katherine H. Freeman
Associate Professor of Geosciences
Special Signatory

Peter Deines
Professor of Geosciences
Associate Head of the Graduate Program in Geosciences

ABSTRACT

Seismic activity may create highly fractured fault zones, providing permeable pathways for the transport of gases from depth to the atmosphere. Also, the flow of deeply derived fluids within fault zones may generate high pore fluid pressures and contribute to fault zone weakness. The spatial and temporal variability, origin, and transport of CO₂ in fractured terrain are evaluated from the perspective of field observations along the San Andreas fault (SAF) system, CA, and numerical modeling. In a preliminary soil CO₂ study conducted (July-August, 1998) along the Parkfield segment of the SAF, single or double-peak CO₂ flux anomalies were observed along fault-crossing transects at five sites. Values of $\delta^{13}\text{C}$ (-23.7 to -21.6 ‰) and $\Delta^{14}\text{C}$ (98.4 to 112.4 ‰) for soil CO₂ were characteristic of CO₂ of biogenic origin. These observations suggest that anomalously high CO₂ fluxes are due to enhanced biogenic CO₂ flow along fault-related fractures. Soil CO₂ surveys were conducted (February-May, 2000) along the SAF in Parkfield and the Calaveras fault (CF) in Hollister, CA. CO₂ flux was measured within grids with portable instrumentation, and continuously with meteorological parameters at a fixed station, in both faulted and unfaulted areas. Areal trends observed within grids suggest that zones of elevated CO₂ flux may be related to subsurface fracturing on small spatial scales. Greater spatial and temporal variability of surface CO₂ fluxes was observed at SAF and CF sites, relative to corresponding background areas. $\delta^{13}\text{C}$ (-23.3 to -16.4 ‰) and $\Delta^{14}\text{C}$ (75.5 to 94.4 ‰) values of soil CO₂ are indicative of biogenic CO₂. SAF CO₂

flux and meteorological parameter time series indicate that effects of temperature variations on soil CO₂ respiration and wind speed variations on atmospheric airflow through fractures modulate surface CO₂ flux. Profiles of soil CO₂ concentration ([CO₂]) as a function of depth were measured at multiple sites within SAF and CF grids and indicate that advective CO₂ flow accounts for up to 85% of the surface flux. Decrease in [CO₂] with depth observed in some profiles suggests atmospheric air flow through soil fractures. The relatively high spatial and temporal variability of surface CO₂ fluxes observed at SAF and CF sites is therefore interpreted to be due to wind-driven atmospheric air flow through more highly fractured soils at these sites, relative to corresponding background areas. The response of soil gas transport processes and resulting soil gas concentration profiles to changing soil physical properties, biological respiration rates, and boundary conditions was tested using one-dimensional finite difference models of diffusive CO₂ flow and advective-diffusive CO₂ and air flow. When transport is purely diffusive, the shape of [CO₂] profiles is sensitive to soil CO₂ production rates, CO₂ flux at the base of the soil column, and soil diffusivity. When advective and diffusive transport of CO₂ and air are considered, transport processes operating through the soil column and the geometry of gas concentration profiles are most sensitive to the basal gas flux, followed by soil diffusivity, permeability and CO₂ production rate. The time required for conditions in [CO₂] and [air] profiles to approximate steady state decreases as the relative advective contribution to flow increases. Results suggest that small magnitude basal gas fluxes can produce total pressure gradients sufficient to drive advective gas flow through soil columns. Therefore, interpretations of soil gas data collected in faulted/fractured

terrain should consider the effects of wind-driven air flow through soils on gas transport and resulting soil gas concentration profiles and surface fluxes.

Table of Contents

List of Tables	ix
List of Figures	x
Preface	xiv
Acknowledgments	xv
Chapter 1. CO ₂ Degassing along the San Andreas Fault, Parkfield, California	1
1.1 Abstract	1
1.2 Introduction	1
1.3 Field and Analytical Methods	3
1.4 Results	5
1.5 Discussion and Conclusions	6
Chapter 2. Soil CO ₂ Flow in Fractured Terrain I: Observations from the San An-	
dreas and Calaveras Faults, CA	16
2.1 Abstract	16
2.2 Introduction	17
2.3 Survey Sites	19
2.4 Methods	20
2.4.1 Field Measurements	20
2.4.2 Laboratory Analyses	22

2.4.3	Data Analyses	23
2.5	Results	25
2.5.1	Surface CO ₂ flux	25
2.5.1.1	Spatial variation	25
2.5.1.2	Temporal variation	27
2.5.2	Soil gas chemistry and isotopic composition	28
2.5.3	Soil [CO ₂] profiles	29
2.5.3.1	Spatial variation	29
2.5.3.2	Temporal variation	30
2.6	Discussion	31
2.6.1	Fault zone CO ₂ flux	31
2.6.2	CO ₂ source	32
2.6.3	Soil gas transport	34
2.6.4	Conceptual gas flow model	43
2.7	Conclusions	45
Chapter 3. Soil CO ₂ Flow in Fractured Terrain II: Modeling Advective and Diffusive Transport of CO ₂ and Air Through Soils		
3.1	Abstract	64
3.2	Introduction	65
3.3	Gas Transport Models	68
3.3.1	General formulation	69
3.3.1.1	Diffusive transport	69

3.3.1.2	Advective-diffusive transport	71
3.3.2	Solution methods	72
3.3.2.1	Analytical solution for steady state diffusion model	72
3.3.2.2	Numerical solution of steady state advection-diffusion and transient diffusion and advection-diffusion models	75
3.3.3	Model Parameters	77
3.4	Results	80
3.4.1	Diffusion-only models	80
3.4.2	Advection-diffusion models	81
3.4.2.1	Effect of soil diffusivity	82
3.4.2.2	Effect of soil permeability	83
3.4.2.3	Effect of basal gas flux	83
3.4.2.4	Effect of soil CO ₂ production	84
3.4.2.5	Effect of model parameters on response time	85
3.5	Discussion	86
3.5.1	Comparison of model results to field observations	86
3.5.2	Implications for fault zone soil gas studies	91
3.6	Conclusions	93
3.7	Appendix I	97
	References	121

List of Tables

1.	Carbon isotopic compositions of soil gas CO ₂	8
2.	Mean and standard deviation of SAF, PB, CF, and HB CO ₂ flux populations	47
3.	Chemical and isotopic compositions of Parkfield and Hollister soil gases	48
4.	CF and SAF grid CO ₂ concentration profile measurement date and time, distance from fault trace, soil temperature, and surface CO ₂ flux	49
5.	Notation of model parameters.	101
6.	Gas parameters used in models.	102
7.	Range of parameter values used in models	102

List of Figures

1.	Map of CO ₂ flux survey sites along the Parkfield segment of the SAF	9
2.	Plot of CO ₂ flux vs. distance from the SAF trace	10
3.	Transects a-c at MM showing CO ₂ flux and concentration vs. distance from the SAF trace	11
4.	Transects a-c at OR showing CO ₂ flux vs. distance from the SAF trace	12
5.	Transects a and b at PO showing CO ₂ flux vs. distance from the SAF trace	13
6.	Transect at WR showing CO ₂ flux and CO ₂ concentration vs. distance from the SAF trace	14
7.	Transect at JR showing CO ₂ flux and CO ₂ concentration vs. distance from the SAF trace	15
8.	Shaded relief map of central California	50
9.	Plot of CO ₂ flux versus distance from fault traces	51
10.	Maps of SAF and PB grid surface CO ₂ flux and flux spatial correlation coefficients	52
11.	Maps of CF and HB grid surface CO ₂ flux and flux spatial correlation coefficients	53
12.	Maps of SAF and PB grid time-adjusted surface CO ₂ flux and flux spatial correlation coefficients	54

13.	Maps of CF grid time-adjusted surface CO ₂ flux and flux spatial correlation coefficients	55
14.	Time series and power spectra for CCFMS CO ₂ flux, atmospheric temperature and pressure, and wind speed measurements	56
15.	Plots of correlation coefficients as a function of time lag for CCFMS CO ₂ flux and meteorological parameter measurements	57
16.	$\delta^{13}\text{C}$ versus $1/\text{CO}_2$ concentration for soil gases	58
17.	Soil CO ₂ concentration profiles for SAF and CF survey sites	59
18.	Temporal variability of permanent soil CO ₂ concentration profile SAFB	60
19.	Temporal variability of permanent soil CO ₂ concentration profile SAFA	61
20.	Plot of correlation coefficients as a function of time lag for permanent soil CO ₂ concentration profiles SAFB and SAFA	62
21.	Schematic of gas flow in fractured terrain	63
22.	Soil CO ₂ concentration profiles measured within SAF and CF grids . . .	103
23.	Schematic of gas flow in fractured terrain	104
24.	Boundary conditions for model of one-dimensional (a) diffusive gas flow and (b) combined advective and diffusive gas flow through a soil column	105
25.	Effect of varying diffusion-only model parameters on soil CO ₂ concentration profile shape	106
26.	Average rate of change of CO ₂ mass in diffusion model domains as a function of model run time for cases where soil diffusivity, ϕ_1 for $L_1=20$ cm, and ϕ_1 for $L_1=40$ cm were varied	107

27.	Average rate of change of CO ₂ mass in diffusion model domains as a function of model run time for cases where ϕ from 100 cm to the soil surface, basal CO ₂ flux without soil ϕ , and basal CO ₂ flux with soil ϕ were varied	108
28.	Effect of varying soil diffusivity on shape of soil CO ₂ and air concentration profiles and magnitude of total, advective, and diffusive fluxes through soil column	109
29.	Effect of varying B_k on shape of soil CO ₂ and air concentration profiles and magnitude of total, advective, and diffusive fluxes through soil column	110
30.	Effect of basal gas flux on shape of soil CO ₂ and air concentration profiles and magnitude of total, advective, and diffusive fluxes through soil column	111
31.	Effect of varying CO ₂ concentration of basal gas flux on shape of soil CO ₂ and air concentration profiles and magnitude of total, advective, and diffusive fluxes through soil column	112
32.	Effect of varying ϕ_1 for $L_1 = 20$ cm on shape of soil CO ₂ and air concentration profiles and magnitude of total, advective, and diffusive fluxes through soil column	113
33.	Effect of varying ϕ_1 for $L_1 = 40$ cm on shape of soil CO ₂ and air concentration profiles and magnitude of total, advective, and diffusive fluxes through soil column	114
34.	Effect of varying ϕ_1 for $L_1 = 40$ cm and ϕ_2 for $L_2 = 60$ cm on shape of soil CO ₂ and air concentration profiles and magnitude of total, advective, and diffusive fluxes through soil column	115

35. Effect of varying ϕ_1 for $L_1 = 40$ cm in the absence of basal gas flux on shape of soil CO_2 and air concentration profiles and magnitude of total, advective, and diffusive fluxes through soil column 116
36. Effect of varying ϕ_1 for $L_1 = 40$ cm and ϕ_2 for $L_2 = 60$ cm (without basal gas flux) on shape of soil CO_2 and air concentration profiles and magnitude of total, advective, and diffusive fluxes through soil column 117
37. Average rate of change of mass of gas i in two-component advection-diffusion model domains as a function of model run time for cases where soil diffusivity, permeability, basal gas flux, and CO_2 concentration of basal gas flux were varied 118
38. Average rate of change of mass of gas i in two-component advection-diffusion model domains as a function of model run time for cases where ϕ_1 for $L_1 = 20$ cm, ϕ_1 for $L_1 = 40$ cm, ϕ_1 for $L_1 = 40$ cm and ϕ_2 for $L_2 = 60$ cm with basal gas flux, and ϕ_1 for $L_1 = 40$ cm without basal gas flux were varied 119
39. Average rate of change of mass of gas i in two-component advection-diffusion model domains as a function of model run time for case where ϕ_1 for $L_1 = 40$ cm and ϕ_2 for $L_2 = 60$ cm were varied without basal gas flux 120

Preface

The majority of Chapter One of this thesis was published as a multiple-authored work: Lewicki, J.L. and S.L. Brantley, CO₂ degassing along the San Andreas fault, Parkfield, California, *Geophys. Res. Lett.*, 27, 5-8, 2000. Chapter Two was submitted for review as a multiple-authored work: Lewicki, J.L., W.C. Evans, G.E. Hilley, M.L. Sorey, J.D. Rogie, and S.L. Brantley, Soil CO₂ flow in fractured terrain I: observations along the San Andreas and Calaveras faults, CA, *J. Geophys. Res.*, in review. Jennifer Lewicki was the first author of both of these manuscripts and was responsible for the majority of the related data collection and analysis and manuscript preparation.

Acknowledgments

I am grateful to my thesis advisor, Susan Brantley, for the encouragement and guidance she has given me during my time at Penn State. I am also grateful to George Hilley, Bill Evans, Mike Sorey, Rich Liechti, John Rogie, and Mack Kennedy for invaluable advice, reviews of this work in its various forms, and assistance in the field. I greatly appreciate the helpful suggestions of my thesis committee, Lee Kump, Derek Elsworth, Katherine Freeman, and Michael Arthur. Doug White, John Southon, Dave Stonestrom, and Kathy Akstin provided carbon isotopic and soil porosity analyses critical to this research. I also thank Cindy Werner and Don Voigt for important assistance with instrumentation as I began my research at Penn State. I credit the American Geophysical Union for permission to include Lewicki, J.L. and S.L. Brantley, "CO₂ degassing along the San Andreas fault, Parkfield, California," *Geophysical Research Letters* 27, 5-8, copyright by the American Geophysical Union, in this thesis. I am indebted to the U.S. Geological Survey (Menlo Park), the Penn State Biogeochemical Research Initiative for Education (BRIE) sponsored by NSF (IGERT) grant DGE-9972759, the Department of Geosciences (Penn State), the Center for Environmental Chemistry and Geochemistry (Penn State), and the NASA Earth System Science Fellowship for partial funding of this research. Finally, I am very thankful for the constant support and encouragement shown to me by George Hilley, Marilyn, John, and John Lewicki, and Annia Fayon throughout my graduate career.

Chapter 1

CO₂ Degassing along the San Andreas Fault, Parkfield, California

1.1 Abstract

The fluxes, concentrations, and carbon isotopic compositions of soil CO₂ were measured along the Parkfield segment of the San Andreas fault (SAF). Single or double-peak CO₂ flux anomalies ($> 18 \text{ g m}^{-2}\text{d}^{-1}$) were observed along 12 of 16 fault-crossing transects at five sites. Flux anomalies did not coincide with concentration anomalies. Flux anomalies paralleled the fault trace, suggesting that the enhanced flux was related to zones of high diffusivity/permeability. One flux anomaly may have been accentuated by a 0.3 mm creep event. However, values of $\delta^{13}\text{C}$ (-23.7 to -21.6 ‰) and ^{14}C (110.5 to 111.9 pmC) for soil gas CO₂ are characteristic of CO₂ of biogenic origin. The CO₂ flux anomalies are therefore consistent with fault-related biogenic gas flow and do not yield evidence for degassing of deeply derived CO₂.

1.2 Introduction

One mechanism that may explain the weakness of the SAF is the generation of high pore fluid pressures within the fault zone [e.g., *Zoback et al.*, 1987]. Since areas of CO₂ discharge globally coincide with regions of seismic activity, it has been suggested that CO₂ may increase pore fluid pressures within fault zones [e.g., *Irwin and*

Barnes, 1975; Barnes et al., 1978]. Current models for weakening of faults by pore fluid pressurization rely on fluid flux from deep crustal and mantle [*Rice, 1992*] or entirely crustal sources [*Byerlee, 1990*]. Calculations of pore fluid pressurization by degassing of deeply derived CO₂ assume a source of free CO₂ in the mantle or crust [*Bredehoeft and Ingebritsen, 1990*].

Recently, *Kennedy et al. [1997]* presented helium concentrations and isotopic data for fluids from SAF system springs and wells and used Varian-Phillips well (Figure 1) data to estimate a ³He flux averaged over the SAF system of approximately 2×10^{-15} mol cm⁻²yr⁻¹, and, assuming a mantle molar CO₂/³He = 10¹⁰, a mantle-derived CO₂ flux of approximately 0.02 g m⁻²d⁻¹. *Kennedy et al. [1997]* hypothesized that the CO₂ flux may generate fault-weakening pore fluid pressures. *Kharaka et al. [1999]* presented surficial and dissolved CO₂ fluxes of approximately 0.086 to 86 g m⁻²d⁻¹ for two drainage areas within the SAF system. Using these flux values, they modeled pore fluid pressurization and suggested that their highest measured CO₂ fluxes may regenerate lithostatic pressures following fault rupture on time scales consistent with SAF earthquake cycles. Anomalously high CO₂ concentrations ([CO₂]) have been measured in soils along the Calaveras fault, California [*King et al., 1996*]; however, no measurements of CO₂ flux on the SAF have been published.

To determine the magnitude and source of CO₂ fluxes along the SAF, we measured CO₂ flux and collected soil gases along the Parkfield segment of the SAF (Figure 1). The Parkfield segment was chosen because: 1) This segment is creeping at the surface (1.8 cm yr⁻¹) and has been the site of five moderately sized earthquakes since 1857 [*Bakun and Lindh, 1985*]. 2) Seismicity at Parkfield may be related to a highly

fractured fault zone with anomalously high fluid content [e.g., *Johnson and McEvilly*, 1995; *Unsworth et al.*, 1997]. 3) *Kennedy et al.* [1997] reported a $^3\text{He}/^4\text{He}$ ratio of 2 Ra in the Varian-Phillips well (Figure 1), indicating contribution of mantle-derived helium. 4) This segment of the fault is well monitored as part of the Parkfield prediction experiment [e.g., *Bakun and Lindh*, 1985].

1.3 Field and Analytical Methods

CO_2 flux (F , $\text{g m}^{-2}\text{d}^{-1}$) was measured using a cylindrical open-bottomed accumulation chamber placed on the soil surface (see *Norman et al.* [1992]). The contained air was circulated through the chamber and a LI-COR 6262 infrared gas analyzer (IRGA). $[\text{CO}_2]$ was recorded every 1 s. Pressure (P , kPa) and temperature (T , K) were measured by a pressure transducer and a thermocouple, respectively. The air was desiccated with $\text{Mg}(\text{ClO}_4)_2$ before entering the IRGA.

To measure flux when the gradient in $[\text{CO}_2]$ at the soil-air interface was relatively undisturbed, the scrubbing protocol of *Norman et al.* [1992] was followed. The rate of change of $[\text{CO}_2]$ in the chamber ($d[\text{CO}_2]/dt$, ppmv s^{-1}) was then measured at the point when $[\text{CO}_2]$ equaled ambient $[\text{CO}_2]$. The flux of CO_2 was calculated according to

$$F = k \left(\frac{V}{A} \right) \left(\frac{T_o}{T} \right) \left(\frac{P}{P_o} \right) \left(\frac{d[\text{CO}_2]}{dt} \right) \quad (1.1)$$

where k is a constant ($155.87 \text{ g s m}^{-3}\text{d}^{-1}$), P_o and T_o are standard P and T , respectively, V is the volume of the system (m^3), and A is the area of the chamber footprint (m^2) [e.g., *Koepenick et al.*, 1996]. Based on laboratory measurements of imposed CO_2 fluxes,

systematic bias associated with the accumulation chamber method is estimated to be -12.5 % [Evans *et al.*, 2001] and measurement reproducibility is ± 10 % [Chiodini *et al.*, 1998].

[CO₂] was measured in the field in soil gases collected at 30 cm (MM c and d and WR transects) or 50 cm (JR transect) depth with a Bacharach 2810 IRGA (measurement accuracy = ± 5 vol.% or ± 50 ppm). Soil gas samples were collected for carbon isotopic analyses at 50 cm depth in pre-evacuated 2 L Pyrex flasks. Stable carbon isotope ratios for CO₂ were measured by conventional gas-ratio mass spectrometry (analytical precision = ± 0.15 ‰), relative to the PDB reference standard. The ¹⁴C of CO₂ samples was measured at the Lawrence Livermore National Laboratory (L.L.N.L.) Center for Accelerator Mass Spectrometry (measurement errors reported in Table 1).

Fluxes (and in some cases concentrations) of CO₂ were measured at 2 to 10 m intervals along 16 transect lines (100 to 130 m long) that crossed approximately normal to the fault trace during July and August, 1998. Sites (Figure 1) were selected based on accessibility, geomorphic expression of the fault trace, and/or the presence of geophysical instrumentation. The fault trace was located to within ± 5 m. At most sites, measurements were made along multiple parallel transects located 5 to 20 m apart.

During the survey, no rain fell and daytime temperatures ranged from 27 to 46°C. Annual grasses (e.g., farmer's foxtail and wild oat) dominate vegetation types at survey sites.

1.4 Results

In this study, 387 measurements of CO₂ flux (1 to 63 g m⁻²d⁻¹) were made along transects at the MM (five transects), OR (three transects), PO (two transects), WR (three transects), and JR (three transects) sites (Figure 1), and 105 measurements of [CO₂] (0.1 to 2.6 vol.%) were made along four of these transects at the MM, WR, and JR sites. Flux measurements were repeated along MM transects c (c1 and c2) and d (d1, d2, and d3). Flux measurements along all transects belong to a single lognormal population for which the mean (μ) and standard deviation (σ) were calculated for the log-transformed data [David, 1977]. Measured soil gas concentrations $> \mu + n\sigma$ for a survey population are commonly considered anomalously high; however, the choice of the value of n varies [Klusman, 1993]. Here, anomalous CO₂ flux values are defined as $> \mu + 2\sigma$ of the entire population (> 18 g m⁻²d⁻¹) (Figure 2). Anomalously high CO₂ fluxes were measured along 12 of the 16 transects, always within 45 m of the fault trace.

Along all transects at the MM site, anomalously high CO₂ fluxes were measured 25 to 40 m SW of the fault trace (Figure 3). A fault-straddling double-peak anomaly was observed along MM line a. The CO₂ flux anomaly observed along MM line c (40 m SW of the fault trace), as well as a peak in [CO₂] 30 m SW of the fault trace, increased from July 31 (transect c1) to August 3 (transect c2). The xmm1 creepmeter recorded 0.3 mm of right lateral movement on August 1, between approximately 9:00 AM and 5:00 PM at site MM [R. Leichti, U.S.G.S., pers. commun.]. Along MM lines c1 and c2, peaks in [CO₂] SW of the fault trace are offset (located closer to the fault trace) from CO₂ flux anomalies.

Along all three transects at the OR site, anomalously high CO₂ fluxes were measured 5 to 25 m SW of the fault trace (Figure 4). A single-peak CO₂ flux anomaly was measured along each of the two transects at the PO site within 0 to 10 m NE of the fault trace (Figure 5). At the WR site, anomalous CO₂ fluxes displaying a double-peak feature were measured within 25 m of the fault trace along one transect (Figure 6). However, measured [CO₂] showed little variation. A single-peak CO₂ flux anomaly was measured at the JR site 30 m SW of the fault trace (Figure 7). Again, measured [CO₂] along this line was relatively constant.

Carbon isotopic compositions were measured on five soil gas samples, three of which were from sites with anomalously high CO₂ flux (Table 1); $\delta^{13}\text{C}$ values for soil gas CO₂ range from -23.7 to -21.6 ‰ (PDB). ¹⁴C contents of soil gas CO₂ range from 110.5 to 111.9 pmC.

1.5 Discussion and Conclusions

Double and single-peak CO₂ flux anomalies (Figures 3-7) are similar to those observed in radon concentration surveys along the SAF system [King *et al.*, 1993, 1996]. At the MM, OR, and PO sites, flux anomalies are observed sub-parallel to the fault trace and may be related to high-permeability fault-related fracture zones. For example, the increase in CO₂ flux and [CO₂] measured on August 3 along MM line c2 may have resulted from deformation-enhanced permeability of the fault zone. However, MM lines c1 and c2 were measured at different times: c1 at 7:30 to 10:30 AM and c2 at 2:45 to 5:45 PM. Therefore, flux and [CO₂] may also have changed due to diurnal variations in biological activity [e.g., Amundson and Davidson, 1990, and references therein].

$\delta^{13}\text{C}$ values for soil gas CO_2 at Parkfield fall within the range of values typical of bulk organic carbon of C_3 plants [O'Leary, 1988] and do not indicate significant contribution of CO_2 from sources such as marine carbonates ($\delta^{13}\text{C} = 0 \pm 4 \text{ }^{\circ}/_{\text{oo}}$, Ohmoto and Rye [1979]) or the mantle ($\delta^{13}\text{C}$ of MORB $\text{CO}_2 = -9$ to $-4 \text{ }^{\circ}/_{\text{oo}}$, e.g., Pineau and Javoy [1983]). Root respiration of grasses should yield CO_2 with ^{14}C content near that of the atmosphere (e.g., ^{14}C content of 1998 clean air = $109.5 \pm 0.5 \text{ pmC}$, J. Southon, L.L.N.L., pers. commun.). The ^{14}C contents of most soil gas samples (Table 1) are greater than this, indicating admixture of CO_2 derived from decay of young (post-bomb testing) organic matter. Given that the lowest measured ^{14}C value = 110.5 pmC , the flux of mantle-derived CO_2 reaching the soil surface at Parkfield must be $\leq 0.03 \text{ g m}^{-2}\text{d}^{-1}$ if we can assume flux and ^{14}C content of biogenic $\text{CO}_2 = 6 \text{ g m}^{-2}\text{d}^{-1}$ and 111.0 pmC (Table 1), respectively, and no contribution of CO_2 from decarbonation. However, the samples as a group show a weak ($R^2 = 0.53$) trend toward lighter $\delta^{13}\text{C}$ values with decreasing ^{14}C content, opposite to the trend expected for mixing of young biogenic CO_2 with CO_2 derived from marine carbonates or the mantle. The anomalously high CO_2 fluxes along the Parkfield segment are therefore consistent with fault-related effects on biogenic gas flow.

Table 1. Carbon isotopic compositions of soil gas CO₂.

Sample site	Distance from fault trace	CO ₂ flux (g m ⁻² d ⁻¹)	[CO ₂] (vol. %)	$\delta^{13}\text{C}_{\text{CO}_2}$ (‰)	$^{14}\text{C}_{\text{CO}_2}$ (pmC)
MMd3	40 m SW	19	1.04	-21.6	111.9±0.5
MMc1	40 m SW	20	2.09	-21.6	111.1±0.5
ORc	25 m NE	12	1.03	-23.0	111.2±0.7
WRb	0 m	6	1.14	-22.2	111.0±0.8
JR	30 m SW	19	0.88	-23.7	110.5±0.5

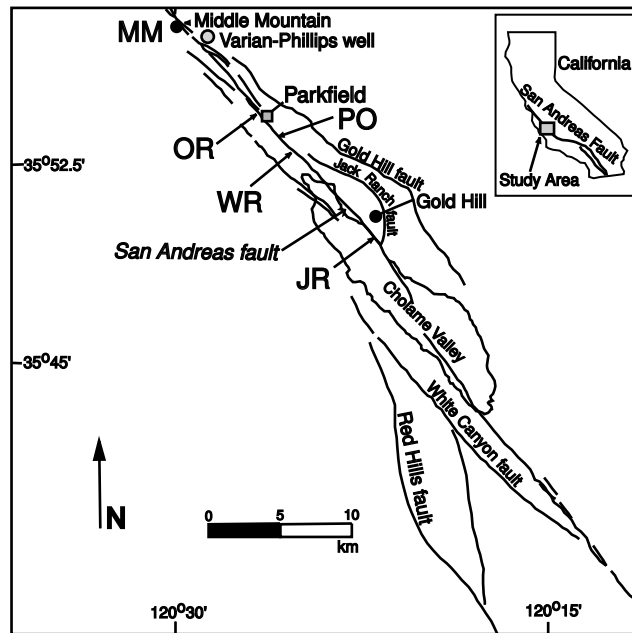


Fig. 1. Map of CO₂ flux survey sites along the Parkfield segment of the SAF (modified from *Thompson and White* [1991] and references therein). Sites include MM (Middle Mountain, at U.S.G.S. xmm1 creepmeter), OR (Owens Ranch, on NE side of Vineyard Canyon road), PO (U.S.G.S. Parkfield Office, at U.S.G.S. xta1 creepmeter), WR (Work Ranch, at U.S.G.S. wkr1 creepmeter), and JR (Jack Ranch, at U.S.G.S. xgh1 creepmeter).

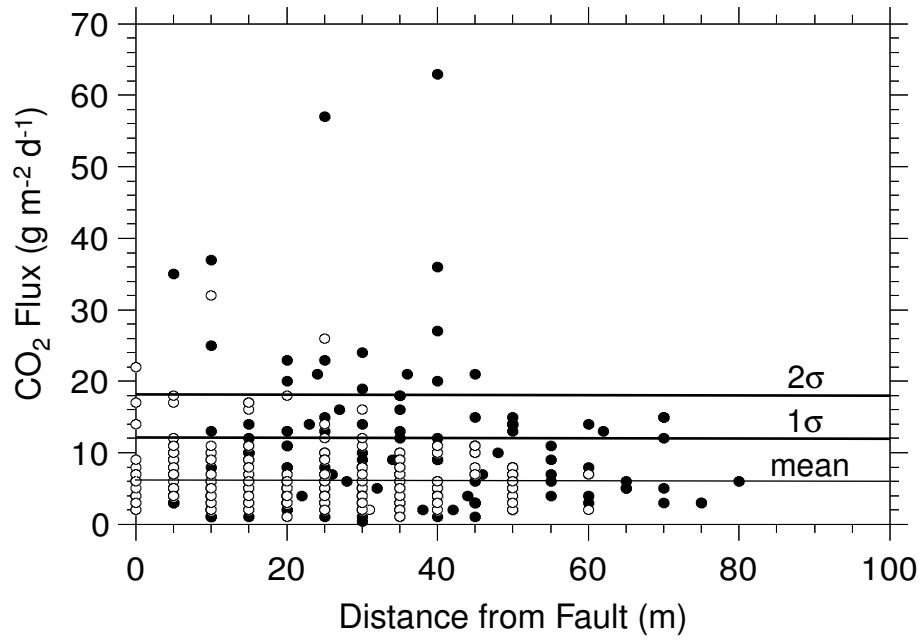


Fig. 2. Plot of CO₂ flux (measured along 16 transects at MM, OR, PO, WR, and JR sites) vs. distance from the SAF trace. Solid and open circles represent fluxes measured SW of and NE of or on the fault trace, respectively. The light and dark lines represent the mean, μ , ($6 \text{ g m}^{-2}\text{d}^{-1}$) and $> \mu + 1\sigma$ ($12 \text{ g m}^{-2}\text{d}^{-1}$) and 2σ ($18 \text{ g m}^{-2}\text{d}^{-1}$) of the entire population of CO₂ flux measurements, respectively.

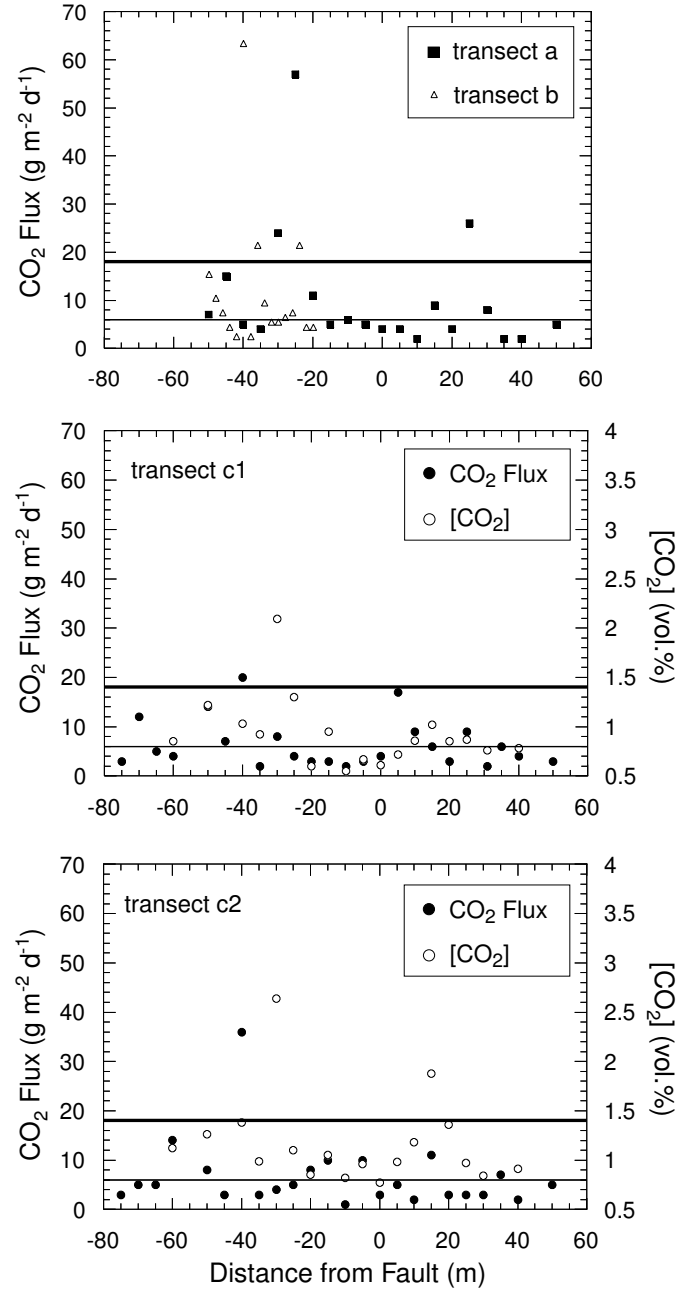


Fig. 3. Transects a-c at MM showing CO₂ flux in g m⁻²d⁻¹ and [CO₂] in vol.% vs. distance from the SAF trace. Zero indicates the fault trace (± 5 m). Negative values indicate distance SW of the fault trace. MM a, b, and c are parallel transects located 17, 5, and 10 m NW of the xmm1 creepmeter, respectively. The light and dark lines represent μ and $\mu + 2\sigma$ of the entire population of CO₂ flux measurements, respectively.

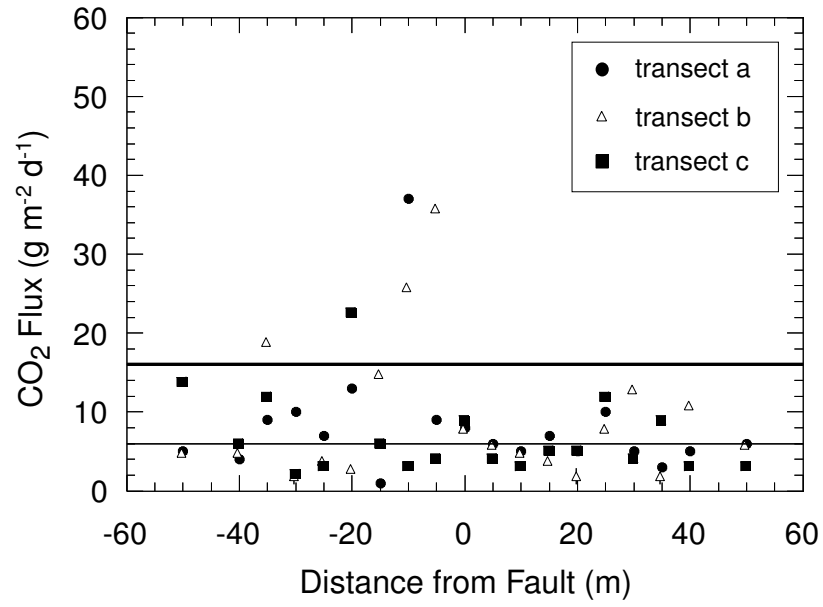


Fig. 4. Transects a-c at OR showing CO₂ flux vs. distance from the SAF trace (see Figure 3). OR b and c are parallel transects located 20 and 35 m SE of a, respectively.

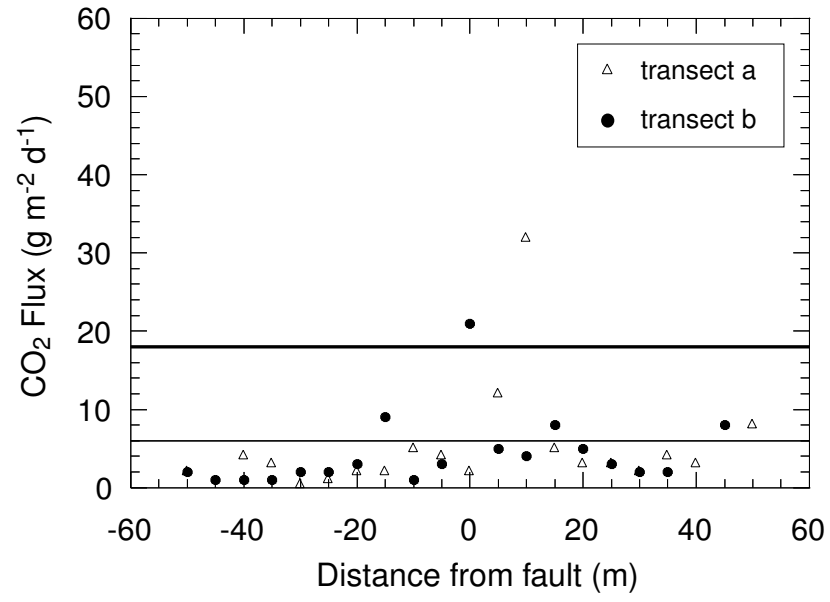


Fig. 5. Transects a and b at PO showing CO₂ flux vs. distance from the SAF trace (see Figure 3). PO a and b are parallel transects located 0.5 and 14 m NW of the xta1 creepmeter, respectively.

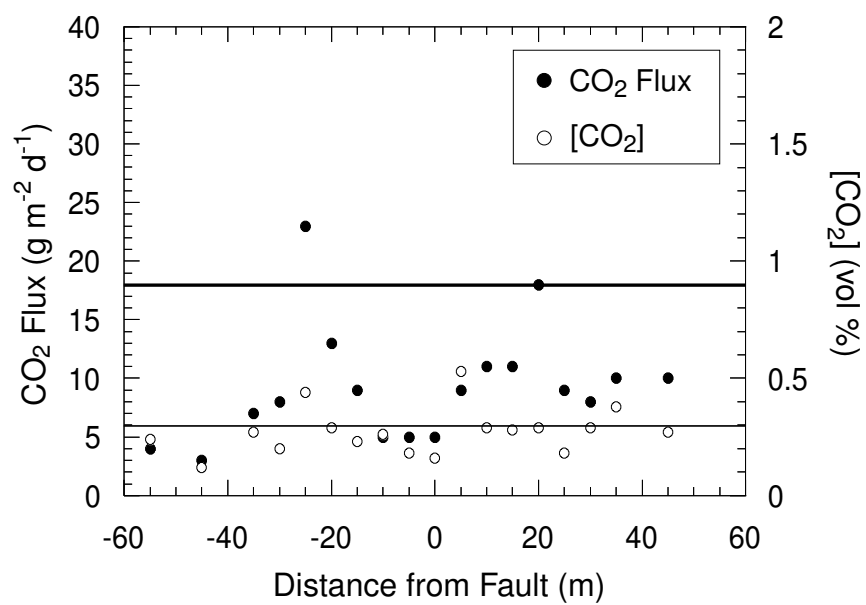


Fig. 6. Transect at WR showing CO₂ flux and [CO₂] vs. distance from the SAF trace (see Figure 3).

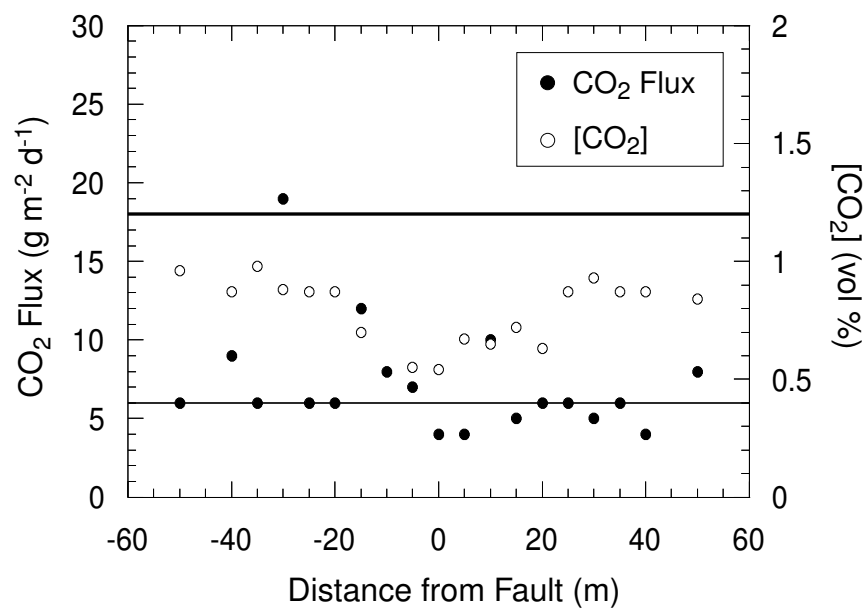


Fig. 7. Transect at JR showing CO₂ flux and [CO₂] vs. distance from the SAF trace (see Figure 3).

Chapter 2

Soil CO₂ Flow in Fractured Terrain I: Observations from the San Andreas and Calaveras Faults, CA

2.1 Abstract

We evaluate a comprehensive soil CO₂ survey along the San Andreas fault (SAF) in Parkfield, and the Calaveras fault (CF) in Hollister, CA in the context of spatial and temporal variability, origin, and transport of CO₂ in fractured terrain. CO₂ flux was measured within grids with portable instrumentation, and continuously with meteorological parameters at a fixed station, in both faulted and unfaulted areas. Greater spatial and temporal variability of surface CO₂ fluxes was observed at faulted SAF and CF sites, relative to corresponding background areas. Areal trends observed within the SAF grid suggest that zones of elevated CO₂ flux may be related to tectonic fractures; however, $\delta^{13}\text{C}$ (-23.3 to -16.4‰) and $\Delta^{14}\text{C}$ (75.5 to 94.4‰) values of soil CO₂ in all areas are indicative of biogenic CO₂. Spectral and correlation analysis of SAF CO₂ flux and meteorological parameter time series indicate that effects of temperature variations on soil CO₂ respiration and wind speed variations on atmospheric airflow through fractures modulate surface CO₂ flux over diurnal cycles. Profiles of soil CO₂ concentration as a function of depth were measured at multiple sites within SAF and CF grids and repeatedly at two locations at the SAF grid. These profiles suggest a surprisingly high component of advective CO₂ flow in soil columns, accounting for up to 85% of the surface

flux. We propose a generalized model of soil CO₂ transport where biogenic CO₂ flow is focused in tectonic and non-tectonic fractures and modulated by temporal variations in meteorological parameters.

2.2 Introduction

The chemical composition and transport of soil gases in fractured terrain have important implications for a broad range of studies including seismotectonics, volcano monitoring, natural resource exploration, and environmental problems. Researchers have measured soil gas concentration and flux anomalies along one-dimensional transects crossing faults [e.g., *Duddridge et al.*, 1991; *Klusman*, 1993; *King et al.*, 1996; *Toutain and Baubron*, 1999; *Lewicki and Brantley*, 2000] and, more rarely, over two-dimensional areas surrounding faults [e.g., *Sorey et al.*, 1998; *Ciotoli et al.*, 1998; *Etiope*, 1999]. These studies suggest that faults and fractures are highly permeable pathways for transport of gases from depth to the atmosphere.

Fault zone soil gas studies have mainly focused on correlation of the location of soil gas concentration or flux anomalies and faults or fractures. Separately, extensive work has been conducted to investigate unsaturated zone gas transport based on laboratory, numerical, and field experiments (see *Scanlon et al.* [1999] for a review of this work), and the influence of meteorological parameters on this transport [e.g., *Massmann and Farrier*, 1992; *Holford et al.*, 1993; *Chen et al.*, 1995; *Pinault and Baubron*, 1996; *Ouyang and Zheng*, 2000]. However, few investigations have integrated these studies using spatial and temporal field measurements of soil gas fluxes and chemistry to understand fault-zone

soil gas transport processes (a notable exception was the study of structurally controlled volcanic CO₂ degassing by *Rogie et al.* [2001] at Mammoth Mountain, CA).

The study of deeply derived fluids (e.g., ³He and CO₂) within the San Andreas fault (SAF) system has been of interest due to the potential role of pore fluid pressurization in the weakness of the SAF [e.g., *Kennedy et al.*, 1997]. To investigate the magnitude and origin of SAF zone soil CO₂ fluxes, *Lewicki and Brantley* [2000] conducted a preliminary soil CO₂ survey along the Parkfield segment of the SAF in which they observed anomalously high CO₂ fluxes of biogenic origin along fault-crossing traverses. They concluded that CO₂ flux anomalies were consistent with fracture-related biogenic gas flow, rather than degassing of deeply derived CO₂. However, the CO₂ flux and soil gas chemical and isotopic data set was of limited scope in that study and therefore did not allow for detailed characterization of the spatial and temporal variability of surface CO₂ fluxes and transport mechanisms of soil CO₂ to the atmosphere.

Expanding upon the work of *Lewicki and Brantley* [2000], we present a comprehensive soil CO₂ flux and soil gas chemical and isotopic data set collected (February-May, 2000) along the SAF in Parkfield, and the Calaveras fault (CF) in Hollister, CA (Figure 8). We investigate 1) spatial correlation between CO₂ fluxes measured within detailed grids and fault location, 2) temporal variation of CO₂ flux relative to meteorological parameters, 3) CO₂ origin, and 4) soil gas transport. Based on our field observations, we propose a generalized model of soil CO₂ transport where biogenic CO₂ flow is focused in highly permeable tectonic and non-tectonic fractures and modulated by temporal fluctuations in meteorological parameters.

2.3 Survey Sites

Our study sites along the SAF and CF are shown in Figure 8. The SAF soil gas survey was conducted in Parkfield on the Taylor ranch at the U.S. Geological Survey (U.S.G.S.) xta1 creepmeter ($35^{\circ}54.1'N$, $120^{\circ}25.5'W$). The Parkfield segment of the SAF is creeping at the surface and has been the site of five moderately sized earthquakes since 1857 [*Bakun and Lindh*, 1985]. Northeast of the SAF, basement rock is Franciscan Complex, a melange composed mainly of weakly metamorphosed accretionary prism deposits. Southwest of the SAF, basement rock is Salinian granite. Depth to the water table at the SAF site (measured in U.S.G.S. well HR in Spring, 2000) is ~ 16 m [*E. Roeloffs*, U.S.G.S., pers. commun.]. The Parkfield background (PB) study site is located ~ 1.5 km northeast of the SAF site on the Taylor ranch, away from the fault zone. Soil textures at SAF and PB sites are silty clay loam and clay, respectively [*Cook*, 1978]. SAF and PB sites host similar annual grass communities (e.g., farmer’s foxtail and wild oat).

The CF soil gas survey was conducted in Hollister at Dunne Park between Sixth and Seventh streets ($36^{\circ}51.1'N$, $121^{\circ}24.2'W$). The sidewalk adjacent to Seventh street has been right-laterally offset by fault creep. Basement rock is Great Valley sequence (marine sandstone, mudstone, and conglomerate), underlain by Coast Range ophiolite and Franciscan Complex rocks. The Hollister background (HB) site is located ~ 2.5 km southeast of the CF site, away from the fault zone. Soil textures are unknown at the CF and HB sites. Turf grass is the main vegetation type at both CF and HB sites.

2.4 Methods

2.4.1 Field Measurements

CO₂ flux was measured over grids using a cylindrical open-bottomed accumulation chamber placed on the soil [e.g., *Norman et al.*, 1992; *Lewicki and Brantley*, 2000]. The contained air was circulated through the chamber and a LI-COR 6262 infrared gas analyzer (IRGA). CO₂ concentration ([CO₂]) was recorded every 1 s, along with pressure (P , kPa) and temperature (T , K), measured by a pressure transducer and a thermocouple, respectively. The air was desiccated with Mg(ClO₄)₂ before entering the IRGA.

The scrubbing protocol of *Norman et al.* [1992] was followed to ensure that the gradient in [CO₂] at the soil-air interface was relatively undisturbed. The rate of change of [CO₂] in the chamber ($d[\text{CO}_2]/dt$, ppmv s⁻¹) was then measured at the point when [CO₂] equaled ambient [CO₂]. The flux of CO₂ (F , g m⁻² day⁻¹) was calculated according to

$$F = k \left(\frac{V}{A} \right) \left(\frac{T_o}{T} \right) \left(\frac{P}{P_o} \right) \left(\frac{d[\text{CO}_2]}{dt} \right) \quad (2.1)$$

where k is a constant (155.87 g s m⁻³ day⁻¹), P_o and T_o are standard P and T , respectively, V is the volume of the system (m³), and A is the area of the chamber footprint (m²). The IRGA was checked for instrumental drift and recalibrated when necessary, every three weeks. Based on laboratory measurements of imposed CO₂ fluxes, systematic bias associated with the accumulation chamber method is estimated to be -12.5 % [*Evans et al.*, 2001] and measurement reproducibility is ± 10 % [*Chioldini et al.*, 1998].

CO₂ flux measurement locations were sited on evenly spaced grid points using a compass and tape measure. Fluxes were measured at 5 m intervals within SAF and PB grids, and at 2.5 m intervals within CF and HB grids. In addition, CO₂ flux was measured at 5 m intervals along six parallel fault crossing transects, parallel to, and 5 to 50 m NW of, the SAF grid. Spacing between these transects varied from 3 to 15 m. During any given day, we measured fluxes sequentially along traverses oriented perpendicular to the SAF and CF fault traces. San Andreas and Calaveras fault traces were located to within ± 5 and 2 m, respectively.

A WEST Systems Continuous CO₂ Flux Monitoring Station (CCFMS) was installed on fractured soil at a distance of 50 m perpendicular to the SAF trace (NE side), adjacent to the SAF flux grid (05-01-00 to 05-13-00) and unfractured soil at a background site ~ 1.5 km north of the SAF grid (03-25-00 to 03-28-00). The CCFMS measured CO₂ flux with a LI-COR GasHound Model LI-800 IRGA contemporaneously with atmospheric pressure (± 0.15 hPa), air temperature (± 0.1 °C, respectively), and wind speed (± 0.1 m s⁻¹) and direction every 30 minutes over the measurement periods. The CCFMS accumulation chamber was automatically lowered onto a fixed collar in the soil and CO₂ flux measurements were made as described above for the portable CO₂ flux instrument (with the exception of the scrubbing protocol). At the SAF grid site, a ground crack (22.0 x 3.5 cm, unknown depth) was located in the accumulation chamber footprint. Soil was assumed to be unfractured at the background site because it was located away from the fault zone and there were no apparent ground cracks.

Soil gas CO₂ concentrations were measured in the field at 10 to 80 cm depth (hereafter this technique is referred to as soil [CO₂] profile measurement) using a perforated soil probe and a Drager polytron or Geotechnical Instruments CD 1/8 IRGA (measurement precision = ± 0.15 and 0.1%, respectively). Soil [CO₂] profiles were measured at different locations within SAF and CF grids by driving a perforated soil probe incrementally into the soil and pumping the soil gas to the [CO₂] analyzer. Surface CO₂ flux above each [CO₂] profile and soil temperature at 20 cm depth were measured within several minutes of profile measurement. SAF profiles were measured from 03-20-00 to 05-03-00, over which time ground cracks (presumably caused by soil drying) were observed in SAF and PB grids, and there were light and heavy rain events on 04-14-00 and 04-16-00 to 04-17-00, respectively. There was no rainfall in Hollister during CF profile measurement time (04-21-00 to 04-22-00) and few ground cracks were observed in CF and HB grids. Soil [CO₂] profiles were also measured repeatedly from 04-13-00 to 05-10-00 at two permanent sites, located adjacent to the SAF grid. At each of these sites, a “nest” of steel points with perforated ends attached to tubing was installed in the soil at 10 cm depth intervals and [CO₂] was monitored at each depth over time. Soil gas samples were collected for chemical and carbon isotopic analyses at 20 – 70 cm depth from soil [CO₂] profiles in SAF and CF grids and at Parkfield background sites in pre-evacuated Pyrex flasks.

2.4.2 Laboratory Analyses

Soil gas chemistry was determined by gas chromatography at the U.S. Geological Survey, Menlo Park, CA, and analytical precision errors are estimated as: [CO₂],

$\pm 1\%$; [Ar], $\pm 2\%$; [N₂] and [O₂], $\pm 0.2\%$. Stable isotope ratios for CO₂ were measured by dual-inlet gas-isotope mass spectrometry. Isotopic abundances are reported in the standard delta notation, calculated relative to the PDB standard using the 18, 19, and 20 NBS standards (measurement accuracy and precision = $\pm 0.15^\circ/\text{oo}$ and $0.05^\circ/\text{oo}$, respectively). The $\Delta^{14}\text{C}$ values of CO₂ samples (± 4.4 to $5.9^\circ/\text{oo}$) were measured at the Lawrence Livermore National Laboratory Center for Accelerator Mass Spectrometry [Southon *et al.*, 1992]. Total porosity was determined for one soil sample collected from Dunne park in Hollister and for two soil samples collected from the SAF site in Parkfield using the clod and pycnometer techniques for bulk density and mean-harmonic particle density, respectively [Klute and Page, 1986].

2.4.3 Data Analyses

Soil CO₂ flux is known to show diurnal variations following a sinusoidal pattern, which has been attributed primarily to changes in meteorological and biological conditions [e.g., Osozawa and Hasegawa, 1995; Ouyang and Zheng, 2000]. Flux transects and grids measured over several hours must account for these diurnal changes in order to fully investigate areal CO₂ flux variability. To subtract diurnal trends from SAF, CF, and PB CO₂ flux grid data sets, we assumed a sinusoidal fluctuation in flux measured over each day (i.e., in plots of flux versus measurement time for each day) and used a least-squares inversion to find the best-fit sine wave to each grid dataset. Daily mean CO₂ flux was constrained to be ≥ 0 . In addition, the frequency and phase shift of the sinusoidal fluctuation was required to be constant throughout each grid dataset. However, for those grids collected over several diurnal cycles, the daily mean flux and amplitude

were allowed to vary over each day for the SAF, CF, and PB grids. The best-fit sine wave was subtracted from each data point at time t . Results are reported as time-adjusted CO₂ flux.

Correlation coefficients (C_k) were calculated for 1) CO₂ flux grid data as a function of separation distance ($C_{\Delta X}$), 2) CCFMS data as a function of time lag ($C_{\Delta t}$), and 3) soil [CO₂] profiles as a function of time lag according to

$$C_k = \frac{\sum_{i=1}^n (x_{i,j,k} - \bar{x})(y_{i,j,k} - \bar{y})}{\left[\sum_{i=1}^n (x_{i,j,k} - \bar{x})^2 \sum_{i=1}^n (y_{i,j,k} - \bar{y})^2 \right]^{1/2}} \quad (2.2)$$

where x and y are two series of observations for which the correlation coefficient is calculated and i , j , and k are measurement indices in space and time.

$$y_{X,\theta,\Delta X} = x_{X+\Delta X,\theta,\Delta X} \quad (2.4)$$

$$y_{t,\theta,\Delta t}, x_{t+\Delta t,\theta,\Delta t} \quad (2.5)$$

$$y_{X,t,\Delta t} = x_{X,t+\Delta t,\Delta t} \quad (2.6)$$

Equations 2.4, 2.5, and 2.6 refer to calculation of the correlation coefficient for the CO₂ flux grid, CCFMS, and soil [CO₂] profile data, respectively. For example, we calculated the correlation coefficient for soil [CO₂] profiles measured at different times (t and $t + \Delta t$)

by comparing $[\text{CO}_2]$ measurements made at corresponding locations in space (i.e., soil depth). Best-fit lines to soil $[\text{CO}_2]$ profile correlation coefficients as a function of time lag were constrained to equal one at zero time lag.

Power spectra for CCFMS CO_2 flux, air and soil temperature, wind speed, and atmospheric pressure data were estimated as the square of the coefficients of the fast Fourier transform with a Hanning window. For power spectra estimations, the mean was removed from each of the CCFMS time series by subtracting from each data point the average of the time series.

2.5 Results

2.5.1 Surface CO_2 flux

2.5.1.1 Spatial variation

We made 646, 287, 436, and 97 CO_2 flux measurements at the SAF (4 to $107 \text{ g m}^{-2} \text{ d}^{-1}$), PB (1 to $59 \text{ g m}^{-2} \text{ d}^{-1}$), CF (10 to $428 \text{ g m}^{-2} \text{ d}^{-1}$), and HB (21 to $97 \text{ g m}^{-2} \text{ d}^{-1}$) sites, respectively. The 646 SAF flux measurements include measurements made within a grid at 5 m spacing and those made at 5 m intervals along six transect lines adjacent and parallel to the NW side of the grid. Statistics were calculated for this entire SAF population; however, the SAF CO_2 flux maps presented below do not include the six transects. Flux measurements for SAF, PB, and CF grids belong to lognormal populations, whereas HB grid flux measurements belong to a normal population. We estimated the mean, μ , and standard deviation, σ , for the SAF, PB, and CF log-transformed flux grid data using Minimum Variance Unbiased estimators [*Finney*, 1941; *Sichel*, 1952] and for the

non-transformed flux data sets for all four grids. For SAF, PB, and CF data sets, these methods yield similar results (Table 2); we therefore focus consideration hereafter on μ and σ values estimated for non-transformed data. After *Lewicki and Brantley* [2000], we define anomalously high CO₂ flux for each data set as $> \mu + 2\sigma$ of the population of flux measurements. Anomalously high CO₂ fluxes were measured in SAF and CF grids within 95 and 27.5 m of the fault traces, respectively (Figure 9). Figure 9 shows that μ and σ of both SAF and CF data sets are greater than PB and HB data sets, respectively. There is a systematic increase in σ with μ for all grid data sets; however, when this trend was removed from data, σ of all on-fault data sets remained greater than that of corresponding off-fault data sets.

Temporally unadjusted SAF and PB grids show no clear trend in spatial distribution of areal CO₂ degassing (Figure 10a, d). Image and contour maps of correlation coefficients for SAF and PB grids show low spatial correlation overall (Figure 10b, c, e, f); however, relatively elevated correlation coefficients ($C_{\Delta X} = 0.2$ to 0.3) are evident for distance > 5 m (i.e., $>$ the measurement interval), with NE-trending direction of anisotropy, perpendicular to the fault trace. The CF grid exhibits a zone of enhanced CO₂ flux approximately perpendicular to the CF trace (Figure 11a). Also, CO₂ fluxes are moderately spatially correlated (up to $C_{\Delta X} = 0.4$) at distances > 2.5 m, with E-trending direction of anisotropy (Figure 11b, c). There is no evident spatial trend in the HB CO₂ flux grid and CO₂ fluxes are poorly spatially correlated (Figure 11d-f).

Time-adjusted SAF $C_{\Delta X}$ image and contour maps (Figure 12b, c) show similar magnitude of spatial correlation of CO₂ fluxes as observed in temporally unadjusted data. However, NE-trending direction of anisotropy oriented $\sim 45^\circ$ to the fault trace is more

clearly evident for distance > 5 m in time-adjusted data (Figure 12b, c). Time-adjusted PB $C_{\Delta X}$ maps (Figure 12e, f) show lower overall $C_{\Delta X}$, relative to temporally unadjusted data. The CF time-adjusted grid shows no trend in areal degassing (Figure 13a) and exhibits a lesser degree of spatial correlation than evident in temporally unadjusted data (Figure 13b, c). We did not observe a temporal trend in the HB grid data and therefore do not report time-adjusted HB grid results.

To test the effect of grid geometry on spatial correlation of CO_2 flux, we generated random synthetic data sets with the same measurement spacing, μ , and σ of SAF and CF data sets and varied grid aspect ratios from 1:1 to 1:10. $C_{\Delta X}$ values for each grid geometry showed no grid shape bias on spatial correlation of CO_2 flux.

2.5.1.2 Temporal variation

The CCFMS deployed on fractured soil 5 m from the SAF grid (Figure 10a) measured CO_2 flux, atmospheric temperature and pressure, and wind speed every 30 minutes from 05-01-00 to 05-13-00 (Figure 14). Over this period of time, there was no rainfall in Parkfield. Our CO_2 flux time series record indicates that change in flux over the sampling period was characterized by irregular variability (i.e., flux spikes), superimposed on sinusoidal variability. The μ and σ of the flux population ($n = 573$) are 6 and $7 \text{ g m}^{-2} \text{ d}^{-1}$, respectively. We confine spectral and correlation analysis of CCFMS time series to diurnal time scales due to the relatively short (~ 13 day) CCFMS sampling duration. Power spectra for CO_2 flux and meteorological parameters (Figure 14) show peaks at one cycle d^{-1} (24-hour period), as well as at lower frequencies. We calculated correlation coefficients as a function of time lag (up to ± 12 hours) between CCFMS time

series (Figure 15). Results show that CO₂ flux is moderately positively correlated ($C_{\Delta t} = 0.4$ to 0.5) with atmospheric temperature and wind speed at ~ 2 to 3 and 0.5 -hour time lags, respectively, and poorly correlated with atmospheric pressure. Atmospheric temperature displays maximum positive correlation with wind speed at 0.5 -hour time lag. Atmospheric pressure and wind speed are poorly correlated, whereas atmospheric temperature and pressure are poorly positively correlated and moderately ($C_{\Delta t} \approx 0.4$) negatively correlated at -4 -hour time lag.

The CCFMS was also deployed on unfractured soil at a background site in Parkfield (03-25-00 to 03-28-00) where CO₂ flux and meteorological parameters were measured every 30 minutes. The mean and σ of the flux population ($n = 125$) are 7 and $1 \text{ g m}^{-2}\text{d}^{-1}$, respectively. Variability of the CO₂ flux data set measured on fractured soil at the SAF site is greater than that of CO₂ flux data set measured on unfractured soil at the Parkfield background site. Relatively short sampling duration (~ 3 days) did not allow for spectral and correlation analysis of the Parkfield background data sets, due to poor spectral resolution.

2.5.2 Soil gas chemistry and isotopic composition

Table 3 shows measured chemical and carbon isotopic compositions of soil gases collected from CF and SAF grids and background sites in Parkfield. Chemical and stable carbon isotopic compositions of an atmospheric air sample from Parkfield were also measured. Relative to atmospheric air, soil gases are CO₂-enriched and O₂-depleted; however, CF grid samples CF1, 3, and 5 are also N₂-depleted.

$\delta^{13}\text{C}$ and $\Delta^{14}\text{C}$ values of soil CO_2 range from -23.3 to $-16.4^\circ/\text{oo}$ and 75.5 to $94.4^\circ/\text{oo}$, respectively. $\delta^{13}\text{C}$ values of Parkfield background soil CO_2 fall within the range of SAF grid soil CO_2 values. The $\delta^{13}\text{C}$ value of Parkfield atmospheric CO_2 is $-8.29^\circ/\text{oo}$. A plot of soil gas $\delta^{13}\text{C}$ versus $1/[\text{CO}_2]$ (Figure 16) shows that gas samples collected from 10, 20, 40, 60 and 70 cm depth in $[\text{CO}_2]$ profile SAFA lie along a mixing line between the compositions of Parkfield atmospheric air (PBatm) and the soil gas collected from 70 cm depth. With the exception of sample SAFA60, soil gases show $\delta^{13}\text{C}$ depletion and $[\text{CO}_2]$ increase with depth; SAFA60, collected at 60 cm depth, is $\delta^{13}\text{C}$ enriched and has lower $[\text{CO}_2]$, relative to SAFA40, collected at 40 cm depth. CF1, 3, and 5 soil gases collected from 50 cm depth in CF1, 3, and 5 $[\text{CO}_2]$ profiles display progressive $\delta^{13}\text{C}$ depletion with increasing surface CO_2 flux.

2.5.3 Soil $[\text{CO}_2]$ profiles

2.5.3.1 Spatial variation

Eleven and five soil $[\text{CO}_2]$ profiles were measured within SAF and CF grids, respectively (Figure 17). Table 4 shows the location, date, and time of profile measurement and the measured surface CO_2 flux above each profile. We grouped soil $[\text{CO}_2]$ profiles into three categories, according to profile shape. Category I profiles exhibit $[\text{CO}_2]$ increase with depth. These profiles show a break in slope ($\partial[\text{CO}_2]/\partial z$), usually between 20 and 40 cm depth, with greater $\partial[\text{CO}_2]/\partial z$ at shallow depth. Category II profiles exhibit $[\text{CO}_2]$ increase then decrease with depth. Category III profiles display a complicated pattern, with repeated increase and decrease in $[\text{CO}_2]$ with depth. The distinction between categories is not always definite; for example, SAF10 and CF1 are considered here

as Category III profiles, but they exhibit only a minor decrease in $[\text{CO}_2]$ with depth and could also be Category I. We do not observe a consistent relationship between profile category and distance from the fault trace, measurement date, soil temperature, rainfall event, or vegetation density and type.

2.5.3.2 Temporal variation

We monitored permanent $[\text{CO}_2]$ profiles SAFB and SAFA (Figure 10a) and associated surface CO_2 fluxes from 04-13-00 to 05-10-00. Profile SAFB (Figure 18) shows $[\text{CO}_2]$ increase with depth (Category I) over the measurement period; however, profile $\partial[\text{CO}_2]/\partial z$ varies from day to day and over the course of individual days (e.g., 04-13-00, 04-26-00, 04-28-00). Profile SAFB variability from morning to afternoon measurement time is often characterized by $\partial[\text{CO}_2]/\partial z$ increase. Following a heavy rain event (04-16-00 to 04-17-00), profiles measured on 04-18-00 and 04-19-00 display both $\partial[\text{CO}_2]/\partial z$ increase from 0 to 20 cm depth and surface flux increase, relative to earlier profiles. $[\text{CO}_2]$ below 20 cm on 04-18-00 and 04-19-00 is relatively constant with depth. From 04-19-00 to 05-10-00, profile $\partial[\text{CO}_2]/\partial z$ decreases, along with a general decrease in associated surface flux. Permanent profile SAFA (Figure 19) displays Category III behavior from 04-13-00 to 04-28-00, with $[\text{CO}_2]$ increase, decrease, then increase with soil depth, and Category I behavior from 05-08-00 to 05-10-00, with $[\text{CO}_2]$ increase with soil depth. Similar to profile SAFB, profile SAFA $\partial[\text{CO}_2]/\partial z$ increased from morning to afternoon measurement times; however, from 04-13-00 to 04-28-00, $[\text{CO}_2]$ concentration at 50 to 60 cm depth remained relatively low. SAFA profiles measured from 04-18-00 to 04-26-00 following the heavy rain event display both $\partial[\text{CO}_2]/\partial z$ increase from 0 to 40 cm depth

and surface flux increase, relative to earlier measurements. Profile $\partial[\text{CO}_2]/\partial z$ decreases from 04-28-00 to 05-10-00.

We calculated correlation coefficients as a function of time lag for SAFB and SAFA profiles (Figure 20). Best-fit lines to correlation coefficients indicate high temporal correlation ($C_{\Delta t} \approx 0.8$ to 1) of SAFB profiles over the entire measurement period and moderate to high temporal correlation ($C_{\Delta t} = 0.5$ to 1) of SAFA profiles up to ~ 15 -day time lag. SAFA profiles are moderately to poorly correlated at greater time lags.

2.6 Discussion

2.6.1 Fault zone CO_2 flux

Mean CO_2 fluxes for the SAF and PB grid data sets fall within the mean rates of soil CO_2 respiration in temperate grasslands ($13 \text{ g m}^{-2}\text{d}^{-1}$), croplands ($16 \text{ g m}^{-2}\text{d}^{-1}$), and tropical savannas and grasslands ($19 \text{ g m}^{-2}\text{d}^{-1}$) [*Raich and Schlesinger, 1992*]. Mean CO_2 flux of both CF and HB data sets is greater than the range for natural grasslands; however, we lack information on average respiration rates from areas where turf grass dominates vegetation type, which may be significantly higher. Mean CO_2 flux for the on-fault SAF data set is greater than the off-fault PB data set, whereas mean CO_2 fluxes are similar for CF and HB populations. Greater μ for the SAF flux population relative to the PB flux population may indicate relatively high SAF zone CO_2 production rate. CO_2 production may be elevated at the SAF site due to higher water content in fractured fault zone media, enhancing biological respiration rates.

We do not observe clear spatial trends in CO₂ flux within the CF grid, convincing of structurally related enhanced degassing. Although the CF grid displays a zone of moderately correlated elevated CO₂ flux oriented perpendicular to the fault trace, the time-adjusted CF grids show poorly correlated fluxes (on spatial scale greater than the sampling interval) without spatial trends. The time-adjusted PB grid similarly shows decreased magnitude and degree of anisotropy of spatial correlation of CO₂ flux, relative to the temporally unadjusted grid. These observations emphasize the influence of diurnal CO₂ flux variations on spatial data sets and the need for consideration of these variations in sampling strategy. Poor spatial correlation of CO₂ fluxes at distances \geq our sampling interval also indicates that our sampling interval was greater than the scale of spatial heterogeneity of our study sites; factors controlling spatial flux variability (e.g., CO₂ production rate, soil diffusivity/permeability) operate on spatial scales less than the sampling interval.

Relative to temporally unadjusted data, the time-adjusted SAF grid shows slightly enhanced magnitude and correlation of CO₂ fluxes on spatial scales greater than the sampling interval, with NE-trending direction of anisotropy oriented $\sim 45^\circ$ to the fault trace. Fractures with similar orientation would be consistent with dextral shear along the SAF. Correcting the spatial CO₂ flux data set for temporal variance may therefore have allowed for detection of a tectonic fracture-related signature in CO₂ degassing.

2.6.2 CO₂ source

Power spectral estimates for CCFMS time series indicate that variation in CO₂ flux and atmospheric temperature measured on and above fractured soil, respectively, at

the SAF site is dominated by diurnal periodicity. CO_2 flux is correlated with atmospheric temperature, a finding which may be consistent with solar heating of the soil and resulting soil CO_2 production by root respiration and/or heterotrophic bacteria [e.g., *Dörr and Münnich*, 1987; *Wood et al.*, 1993].

Assuming a 1:1 relationship between biogenic O_2 consumption and CO_2 production in the soil, we compare $[\text{N}_2]$ of soil gas samples ($[\text{N}_2]_{\text{soil}}$) with $[\text{N}_2]$ of atmospheric air ($[\text{N}_2]_{\text{atm}}$) to evaluate possible addition of CO_2 to soil gases from sources other than root respiration and oxidative decay of organic matter. If soil gas CO_2 is derived exclusively from soil biogenic sources and there is no soil N_2 loss and gain from N_2 fixation and denitrification processes, respectively, we expect $[\text{N}_2]_{\text{soil}}$ to be similar to $[\text{N}_2]_{\text{atm}}$. If CO_2 is present in excess of soil biogenic sources, we expect soil gases to be $[\text{N}_2]$ -depleted relative to atmospheric air. Although all soil gas samples from SAF, Parkfield background, and CF sites are $[\text{N}_2]$ -depleted relative to atmospheric air, with the exception of CF samples, $[\text{N}_2]$ depletion is \leq analytical error associated with the measurement ($\pm 0.2\%$). CF1, 3, and 5 samples, however, exhibit greater $[\text{N}_2]$ depletion, which may be explained by a respiration quotient of less than one. Alternatively, $[\text{N}_2]$ depletion may reflect addition of CO_2 to CF1, 3, and 5 samples from processes such as CO_2 exsolution from the water table or vadose zone water at the beginning of the dry season.

$\delta^{13}\text{C}$ values for CF5, SAF3, SAF10, and SAFA40, 60, and 70 soil gas CO_2 fall within the range of values typical of bulk organic carbon of C_3 plants ($\delta^{13}\text{C} = -34$ to -22 ‰, *O’Leary* [1988]). All other CF, SAF, and Parkfield background soil CO_2 samples are relatively $\delta^{13}\text{C}$ enriched. $\delta^{13}\text{C}$ values for Parkfield background soil CO_2 fall within the range of SAF grid soil CO_2 values and do not suggest a unique CO_2 source.

Observed $\delta^{13}\text{C}$ enrichment may be due to one or a combination of the following: 1) contribution of CO_2 derived from C_4 plants ($\delta^{13}\text{C} = -20$ to -10 ‰, *O’Leary* [1988]); 2) contribution of atmospheric air-derived CO_2 ($\delta^{13}\text{C}$ of Parkfield atmospheric air = -8.29 ‰); 3) admixture of CO_2 from isotopically enriched sources such as the mantle or marine carbonates.

Based on direct measurement of the ^{14}C content of 1996 atmospheric air ($\Delta^{14}\text{C} = 97 \pm 1$ ‰, *Gaudinski et al.* [2000]) and ~ 8 ‰ decline in $\Delta^{14}\text{C}$ per year [*Levin and Kromer*, 1997], the ^{14}C content of 2000 atmospheric air is estimated to be 65 ‰. We expect the ^{14}C content of soil CO_2 derived from root respiration of annual grasses to be similar to that of the atmosphere. $\Delta^{14}\text{C}$ values of SAF and CF soil CO_2 samples are slightly enriched relative to that of the 2000 atmosphere and likely reflect admixture of CO_2 derived from oxidative decay of young (post-bomb testing) organic matter. $\Delta^{14}\text{C}$ values do not suggest contribution of CO_2 to soil gases from mantle or marine carbonate sources, consistent with the findings of *Lewicki and Brantley* [2000] for Parkfield SAF soil gas CO_2 . In addition, $\Delta^{14}\text{C}$ values of CF1, 3, and 5 soil gases support addition of CO_2 from a young source, such as seasonal groundwater degassing.

2.6.3 Soil gas transport

Soil CO_2 transport to the atmosphere may be diffusive (concentration gradient driven), as described by Fick’s first law:

$$F_D = -D_{\text{CO}_2\text{-air}} n_a \tau \nabla [\text{CO}_2] \quad (2.6)$$

where F_D is mass diffusive CO_2 flux ($\text{g cm}^{-2}\text{s}^{-1}$), $D_{\text{CO}_2\text{-air}}$ is the binary diffusion coefficient of CO_2 in air at measured soil temperature (cm^2s^{-1}), n_a is air-filled porosity, τ is tortuosity, and $\nabla[\text{CO}_2]$ is the $[\text{CO}_2]$ gradient (g cm^{-4}), and/or advective (total pressure gradient driven), as described by Darcy's law:

$$F_A = -\frac{B_k P_{\text{CO}_2}}{\mu} \frac{\nabla P}{RT} \quad (2.7)$$

where F_A is molar advective CO_2 flux ($\text{mol L}^{-2}\text{t}^{-1}$), B_k is the intrinsic permeability of the medium (L^2), P_{CO_2} is CO_2 partial pressure ($\text{M L}^{-1}\text{t}^{-2}$), μ is dynamic gas viscosity ($\text{M L}^{-1}\text{t}^{-1}$), ∇P is the total pressure gradient ($\text{M L}^{-2}\text{t}^{-2}$), T is absolute temperature, and R is the gas constant ($\text{M L}^2\text{t}^{-2}\text{T}^{-1}\text{mol}^{-1}$). Small total pressure gradients (at present detection limits) can produce advective fluxes greater than diffusive fluxes [e.g., *Thorstenson and Pollock*, 1989]. Meteorological parameters may modulate soil CO_2 flow to the atmosphere by influencing concentration and/or total pressure gradients either directly (e.g., barometric pumping effect) or indirectly (e.g., atmospheric and soil temperature effects on soil CO_2 respiration).

To estimate the maximum extent to which Fickian diffusion accounts for surface CO_2 fluxes measured above soil $[\text{CO}_2]$ profiles in SAF and CF grids, we calculated diffusive CO_2 fluxes based on near-surface $[\text{CO}_2]$ gradients and inferred soil diffusivities (Equation 2.6). Calculated $D_{\text{CO}_2\text{-air}}$ values ranged from 0.14807 to 0.16384 cm^2s^{-1} [*Marrero and Mason*, 1972], depending on measured soil temperatures. Total porosity values, n_T , for a soil collected from the CF grid and two soils collected at permanent profile SAFB and SAFA sites are 0.52, 0.36, and 0.38, respectively; however, we lack n_T ,

water content, and τ data for most CF and SAF profile sites. Therefore, we made the following assumptions: 1) measured n_T values for SAF and CF soils are representative of soils over their entire respective grids; 2) $n_T = n_a$; 3) $\tau = 0.66$ [Penman, 1940a, b]. In addition, maximum near-surface $\partial[CO_2]/\partial z$ values were used in calculations. In cases where profile $[CO_2]$ at 10 cm depth was approximately equal to surface $[CO_2]$ (e.g., SAFB profiles), likely due to atmospheric airflow through shallow soil, maximum $\partial[CO_2]/\partial z$ values were considered from depth to 10 cm over linear segments of profiles. These conditions yield maximum estimates of F_D values.

Results of diffusive flux calculations suggest that Fickian diffusion accounts at most for 39, 79, and 15% of measured surface CO_2 flux above CF1, 3, and 5 profiles, respectively, and 39, 85, 52, 43, 58, and 71% of surface flux above SAF9, 1, 7, 3, 10, and 5 profiles, respectively. For profiles CF2, CF4, SAF2, SAF4, SAF6, SAF8, and SAF11, diffusion may account entirely for associated surface fluxes. Diffusion accounts at most for 46 to 92% of measured surface fluxes above permanent profile SAFA on 04-13-00, 04-14-00, 04-26-00 (09:52 to 16:00), 04-28-00 (15:15), 05-08-00, and 05-10-00 (14:00), whereas it may account entirely for all measured surface fluxes above permanent profile SAFB. For those profiles where maximum estimated diffusive flux accounts for less than 100% of associated surface flux, advection is likely an important process in the transport of soil CO_2 to the atmosphere. Advection may also be important for other profiles if soil water content is considered in calculations. In addition, the spatial and temporal variability of estimated F_D values indicates that mode of soil CO_2 transport varies not only from site to site within SAF and CF areas, but also over time at individual sites (e.g., profile SAFA).

Power spectral estimates for CCFMS time series indicate that variation in wind speed measured by the CCFMS deployed on fractured soil at the SAF site is dominated by diurnal periodicity, whereas atmospheric pressure shows a dominant PSD peak at lower frequency. Atmospheric pressure changes can strongly influence advective flow of soil gas to the atmosphere [e.g., *Massmann and Farrier*, 1992] via the barometric pumping effect, whereby pressure increase and decrease at the surface will force atmospheric air into the soil and soil air to the atmosphere, respectively. However, our observations show CO₂ flux and atmospheric pressure are poorly correlated on diurnal time scales. The high PSD peak observed for atmospheric pressure at low frequency is consistent with a stronger control of low frequency events such as slow moving weather fronts on atmospheric pressure fluctuations than that of diurnal thermal and gravitational effects. CO₂ flux and atmospheric pressure may therefore show higher correlation over cycles > 24 hours. Longer CO₂ flux and atmospheric pressure time series records are necessary to resolve low frequency atmospheric pressure effects on surface CO₂ flux.

Positive correlation of CO₂ flux with wind speed at ~0.5-hour time lag suggests that CO₂ flux may rapidly respond to changes in wind speed. Wind speed variability may create local fluctuations in air pressure, influencing soil aeration [e.g., *Reimer*, 1980]. In particular, correlation between wind speed and radon flux from soils has been observed and attributed to wind speed related variations in subsurface pressure gradients [*Schery et al.*, 1984; *Schery and Siegel*, 1986]. We suggest that elevated wind speed may cause enhanced atmospheric airflow through fractured soil, allowing for air to serve as a carrier gas for soil-respired CO₂, which results in enhanced surface CO₂ flux. Wind speed itself is poorly correlated with atmospheric pressure and displays a complex

relationship with atmospheric temperature variation. We propose that wind speed may be primarily responsible for the flux spikes observed in the SAF CCFMS time series due to the irregular nature of wind speed variability over diurnal cycles, relative to other more smoothly varying meteorological parameters. This effect on CO₂ flux variability may be enhanced at the SAF fractured soil CCFMS site, relative to the unfractured soil site, as suggested by the greater estimated σ of the fractured soil CO₂ flux times series. In addition, greater σ for SAF and CF grid CO₂ flux data sets, relative to PB and HB data sets, respectively, may also reflect fault and/or fracture enhanced atmospheric airflow through soils.

Although we do not consider the relationship between CO₂ flux and soil water content here, soil water exerts an important control CO₂ transport by influencing biological respiration and soil air-filled porosity. Future work should include regular soil water content measurements in conjunction with CO₂ flux and meteorological parameters.

Researchers have observed that CO₂ occupying soil pore space (expressed as [CO₂]) is $\delta^{13}\text{C}$ -enriched relative to that of corresponding CO₂ flux passing through the soil (assumed to equal the $\delta^{13}\text{C}$ of the source organic matter) [e.g., *Dörr and Münnich*, 1980; *Cerling et al.*, 1991]. This minimum observed $\delta^{13}\text{C}$ enrichment is close to the 4.4‰ difference in diffusion coefficients of ¹²CO₂ and ¹³CO₂ and is predicted by diffusion equations [*Cerling et al.*, 1991; *Davidson*, 1995]. Their results indicate that at a given site, soil CO₂ shows increasing $\delta^{13}\text{C}$ enrichment from depth to the surface, due to admixture of atmospheric air. Our results for SAF grid permanent profile SAFA (Figure 16) are consistent with previous studies [e.g., *Cerling et al.*, 1991], showing that compositions of soil CO₂ lie along a mixing line between atmospheric air and sample

SAFA70, collected at 70 cm depth. However, sample SAFA60, collected at 60 cm depth, is $\delta^{13}\text{C}$ -enriched and has lower $[\text{CO}_2]$ relative to SAFA40, collected at 40 cm depth. We interpret these observations to reflect addition of atmospheric air at 60 cm depth by means of lateral advection (possibly wind-driven) through fractured soil. The estimated maximum per-cent contribution of diffusive to total surface CO_2 flux for profile SAFA at 15:15 on 04-28-00 is 80%, supporting a component of advective flow.

CF3, 1, and 5 samples exhibit $\delta^{13}\text{C}$ depletion with increasing surface flux. We infer that both diffusive and advective CO_2 transport are important at these CF profile sites. Interestingly, we observe $4.3^\circ/\text{oo}$ difference between CF3 and 5 $\delta^{13}\text{C}$ values, very close to the $4.4^\circ/\text{oo}$ isotopic fractionation associated with diffusion. These samples suggest two endmembers derived from a similar source organic mass $\delta^{13}\text{C}$ value: a relatively high flux, advection dominated (no isotopic fractionation) site (CF5) and a relatively low flux, diffusion dominated site (CF3). CO_2 transport in the CF1 column may then be some combination of the two transport mechanisms. This interpretation is supported by the observed trend of decreasing per-cent contribution of diffusive to total surface flux for CF3, 1, and 5 profiles (79, 39, and 15%, respectively). Also, CF1 and 5 $[\text{N}_2]$ suggest greater contribution of CO_2 derived from sources other than biological respiration than does CF. This CO_2 may be transported by means of advection through fractured media.

$[\text{CO}_2]$ profile shape may provide information on gas transport in the soil environment at SAF and CF study sites. However, the pattern and behavior of $[\text{CO}_2]$ with soil depth depends on parameters such as CO_2 production rate and distribution, soil physical properties, influence of meteorological parameters on soil gas flow, and whether the profile results from transient or steady-state gas flow. To definitively evaluate mode of

gas transport from $[\text{CO}_2]$ profiles, these parameters must be constrained. Because many of these parameters are poorly known at our sampling sites, we present our preferred interpretations of SAF and CF profiles based on the cumulative body of evidence in this study, but acknowledge that alternative transport models may also explain our profile data.

Category I profiles likely reflect diffusion of soil CO_2 to the atmosphere. Observed break in $\partial[\text{CO}_2]/\partial z$ slope in these profiles (at 20 to 40 cm) may mark the depth of the base of the root zone. Also, we can not rule out a component of advective CO_2 flow in Category I profiles; estimated maximum per-cent diffusive of total surface fluxes for Category I profiles SAF1, SAF3, and CF3 (85, 43, and 79%, respectively) indicate that a component of advective transport is important.

Category II-type $[\text{CO}_2]$ profiles have been previously described in the literature and interpreted to represent a transient state where diffusive transport dominates CO_2 flow [e.g., *DeJong and Schappert*, 1972; *Osozawa and Hasegawa*, 1995]. In this case, Category II profiles may occur after periods of heavy rainfall, causing a decrease in air-filled pore space available for CO_2 flow, and/or during the growing season, when biogenic CO_2 production increases. Under these circumstances, CO_2 accumulates in the shallow soil where pathways for gas flow are limited and/or production rate is high, generating a Category II-type profile.

We alternatively suggest that both diffusion and advection contribute to gas flow in Category II profiles at SAF and CF sites. $[\text{CO}_2]$ may be lowered at depth in the soil column due to wind-driven atmospheric airflow through fractures. CO_2 may be transported up through the column as the base of the column is aerated by atmospheric

air. Superimposed on this flow driven by a total pressure gradient is diffusive transport from high to low $[\text{CO}_2]$. This transport model may be appropriate for our study areas because extensive ground cracking was observed in SAF grid soil that could promote wind-driven air flow through highly permeable soil during profile measurement time. Also, SAF and CF profile categories show no consistent relationship with rain events, soil temperature, observed vegetation density and type, and measurement date (e.g., all three categories were observed at the SAF site on 04-29-00 and 05-03-00). Furthermore, the maximum per-cent of total surface flux that is diffusive estimated for profiles SAF7, SAF5, and CF5 (52, 71, and 15%, respectively) indicates a component of advective CO_2 transport. It should be noted that diffusive flux may also not account for total surface fluxes above other Category II profiles if we account for reduced soil diffusivity due to soil water content in F_D calculations. We hypothesize that all three profile shapes were observed over single days due to heterogeneous soil structure within the SAF and CF study areas.

The irregular "saw-tooth" pattern observed in Category III profiles may also be explained by contribution of both diffusion and advection to gas flow in soil columns. In this case, relatively low $[\text{CO}_2]$ measured at various profile depths may be generated by lateral atmospheric airflow through soil fractures at those depths. For the reasons presented above for Category II profiles, we favor the diffusion-advection transport model for Category III profiles. In addition, $[\text{CO}_2]$ and $\delta^{13}\text{C}$ values measured for soil gases with depth in permanent profile SAFA (a Category III profile) suggest addition of atmospheric air at the point of $[\text{CO}_2]$ decrease with depth.

Over the measurement period, profile SAFB exhibits Category I behavior; we therefore invoke a similar gas transport model to that presented above for Category I profiles. We attribute observed increase in profile SAFB $\partial[\text{CO}_2]/\partial z$ from morning to afternoon measurement times (e.g., on 04-13-00, 04-26-00, 04-28-00) to increasing soil CO_2 production as soil temperature rises. Following the heavy rain event (04-16-00 to 04-17-00), it is likely that soil CO_2 production increased (as suggested by doubling of surface CO_2 flux relative to 04-14-00) and air-filled porosity decreased. SAFB profiles measured on 04-18-00 and 04-19-00 show increased profile $\partial[\text{CO}_2]/\partial z$ in the shallow soil, which may be attributed to one or both of these factors. It is likely that from 04-19-00 to 05-08-00, CO_2 production decreased and/or accumulated CO_2 in the shallow soil was transported to the atmosphere, leading to profile straightening and lower $\partial[\text{CO}_2]/\partial z$. It should be recognized that following the rain event SAFB profiles do not display Category II behavior, further supporting our proposed gas flow model for Category II profiles.

We hypothesize that relatively low $[\text{CO}_2]$ measured at 50 to 60 cm in permanent profile SAFA from 04-13-00 to 04-28-00 was due to lateral atmospheric air flow through the soil column at this depth. We also suggest that the change in shape of profile SAFA from 04-28-00 to 05-10-00 may be due to a change in soil permeability structure over this time, with possible fracture closing at 60 cm depth. In this scenario, the low $[\text{CO}_2]$ condition imposed by atmospheric air flow is no longer present, allowing for diffusion of CO_2 to 60 cm depth from above and below in the soil column until profile straightening occurs.

High correlation of measurements of permanent profile SAFB over the ~one month measurement period indicates that a relatively stable process controls the shape

of SAFB profiles. We suggest that this process is soil CO_2 respiration and that it shows relatively little variation over the measurement period and/or properties of the soil media act to buffer changes in $[\text{CO}_2]$ due to respiration rate variability. Well-correlated SAFA profiles on time scales up to \sim five days may also indicate that soil respiration (or a similarly stable process) controls profile shape over relatively short time scales. However, moderate to poor correlation of SAFA profiles at time lag up to one month indicates that additional processes may be acting to control $[\text{CO}_2]$ variation with depth on these longer time scales. An important process influencing SAFA profile shape is probably change in soil permeability structure (e.g., fracture opening and closing). The different behavior we observe for SAFB and SAFA profiles, located within only 15 m of each other, may reflect heterogeneous soil structure at the SAF study site. Diffusion accounts for only 46 to 92% of surface fluxes above the majority of measured SAFA profiles over time, whereas it accounts entirely for all surface fluxes above permanent profile SAFB. Variability of soil structure (e.g., permeability) may therefore influence the relative importance of diffusive and advective transport mechanisms in the soil column.

2.6.4 Conceptual gas flow model

We summarize our observations of soil CO_2 at SAF and CF study sites with a conceptual model for CO_2 flow through fractured soils (Figure 21). CO_2 may be derived from root respiration (upper 40 cm of soil at SAF and CF sites), heterotrophic bacteria (possibly through the entire soil column), atmospheric air, and, in the case of the CF site, from biogenic source(s) such as seasonal groundwater degassing. Highly permeable tectonic and non-tectonic fractures are hypothesized to focus and enhance

fault zone CO₂ flow. Wind, atmospheric and soil temperature, and atmospheric pressure fluctuations may modulate soil diffusive and advective CO₂ transport to the atmosphere by disturbing [CO₂] and total pressure gradients, respectively. Specifically, temporal effects of meteorological parameters on soil CO₂ flow at the SAF (and possibly the CF) site include influence of diurnal variations in atmospheric (and therefore soil) temperature on soil CO₂ production rate and diurnal wind speed variations on soil atmosphere total pressure gradients. In particular, wind-driven atmospheric airflow through fractures may act to "flush" soil CO₂ through fractures, enhancing magnitude and variability of surface CO₂ flux. Although we did not collect soil water content data, we infer that soil water influences CO₂ production rate and air-filled pore space, therefore modulating CO₂ transport to the atmosphere. Total pressure gradients are most sensitive to variability of meteorological parameters in highly permeable fractured soils. We therefore suggest that the greater spatial and temporal variability of surface CO₂ fluxes observed at SAF and CF study areas, relative to corresponding background areas, is due to more highly fractured (tectonic and/or non-tectonic) soils at the SAF and CF sites.

Our generalized model does not specifically distinguish between tectonic and non-tectonic fracture density and distribution, nor does it require that tectonic fractures reach the soil surface at our study sites. Based on our observations of spatial distribution of surface CO₂ flux at the SAF site, high permeability/diffusivity NE-trending fault-related fractures may exist close to the surface separate from, or connected to, non-tectonic soil fractures. At the CF site, high surface fluxes and evidence of advective biogenic CO₂ flow may be related to subsurface fracturing. Since no clear trend in fracture orientation is

evident in our surface flux observations, tectonic fractures may not reach the soil surface due to soil/sediment overburden.

2.7 Conclusions

Conclusions drawn from the above observations and discussion include:

1. We find that the areal distribution of soil CO₂ flux is complex and highly variable at and between our study sites. Regions of enhanced flux appear to derive from subsurface fracturing; however, areal trends may not consistently reflect regional tectonics and soil CO₂ is of shallow, biogenic origin.
2. Typical soil gas flux and concentration surveys along transects or grids on active faults may be inaccurately interpreted unless the pattern of temporal fluctuations and scale of spatial heterogeneity are considered.
3. Both diffusion and advection are important modes of soil CO₂ transport to the atmosphere at SAF and CF study sites, the relative importance of which varies spatially within study areas and temporally at individual locations.
4. Surface wind, not barometric pumping, seems to be the main factor driving advective soil gas flow over diurnal cycles at study sites. Greater spatial and temporal variability of surface CO₂ fluxes observed at SAF and CF sites, relative to corresponding background areas, is likely due to wind-driven atmospheric airflow through more highly fractured soils at SAF and CF sites.
5. To better characterize the relative importance of specific physical processes and soil properties in soil gas transport in fractured terrain, it is necessary to conduct

additional field studies, supplemented by laboratory and numerical experiments in simple systems where the number of variables influencing gas transport can be controlled.

Table 2. Mean (μ) and standard deviation (σ) of SAF, PB, CF, and HB CO₂ flux populations. μ and σ were calculated for log-transformed and non-transformed data.

flux grid	log-transformed		non-transformed	
	μ	σ	μ	σ
	(g m⁻² d⁻¹)			
SAF	19	11	19	11
PB	13	8	13	8
CF	55	23	56	29
HB	na	na	55	15

Table 3. Chemical and isotopic compositions of Parkfield and Hollister soil gases. CF, SAFA, SAF, and PB refer to soil gas samples collected from CF grid, SAF grid permanent [CO₂] profile SAFA, SAF grid, and Parkfield background areas, respectively. With the exception of SAF12, CF and SAF samples were collected from 50 cm depth in CF and SAF [CO₂] profiles, respectively. SAFA10, 20, 40, 60, and 70 samples were collected from 10, 20, 40, 60, and 70 cm depth, respectively, in permanent [CO₂] profile SAFA. Distance refers to distance from fault trace. Gas concentrations are reported on a water-free basis.

Sample	Distance	CO ₂ flux (g m ⁻² d ⁻¹)	[CO ₂] (vol. %)	[O ₂] (vol. %)	[N ₂] (vol. %)	[Ar] (vol. %)	$\delta^{13}\text{C}_{\text{CO}_2}$ ($^{\circ}/_{\text{oo}}$)	$\Delta^{14}\text{C}_{\text{CO}_2}$ ($^{\circ}/_{\text{oo}}$)
CF1	15 m W	111	2.52	19.2	77.3	0.931	-19.88	81.8
CF3	17.5 m E	84	2.10	19.4	77.5	0.945	-17.22	92.3
CF5	12.5 m E	428	2.35	19.4	77.3	0.919	-21.52	84.9
SAFA10	45 m NE	18	0.0915	21.0	77.9	0.924	-16.84	nd.
SAFA20	45 m NE	18	0.442	20.7	77.9	0.936	-21.35	nd.
SAFA40	45 m NE	18	0.815	20.5	77.8	0.930	-22.55	nd.
SAFA60	45 m NE	18	0.315	20.7	78.0	0.924	-21.66	nd.
SAFA70	45 m NE	18	1.04	20.2	77.8	0.940	-22.87	75.5
SAF3	5 m SW	34	1.12	20.2	77.7	0.920	-23.22	93.3
SAF10	20 m SW	25	0.868	20.4	77.9	0.929	-23.25	nd.
SAF12	55 m NE	50	0.0797	21.0	78.0	0.934	-16.42	nd.
SAF8	80 m NE	14	0.669	20.5	77.9	0.924	-21.45	nd.
PB1	background	9	0.814	20.3	77.9	0.926	-20.49	94.4
PB2	background	9	0.681	20.5	77.8	0.935	-20.14	nd.
PB3	background	18	0.477	20.6	78.0	0.922	-19.03	nd.
PBatm	atmospheric air	na	0.376	21.0	78.0	0.927	-8.29	nd.

Table 4. CF and SAF grid [CO₂] profile measurement date and time, distance from fault trace (Distance), soil temperature, and corresponding surface CO₂ flux.

Profile	Date	Time	Distance	Soil Temp. °C	Surface flux (g m ⁻² d ⁻¹)
CF1	04-21-00	11:26	15 m W	16.8	111
CF2	04-21-00	17:30	42.5 m W	18.0	60
CF3	04-22-00	12:29	17.5 m W	16.0	84
CF4	04-22-00	13:35	50 m E	16.8	50
CF5	04-22-00	15:20	2.5 m E	17.7	428
SAF1	04-29-00	13:15	20 m SW	15.2	43
SAF2	05-03-00	09:30	5 m NE	20.2	10
SAF3	05-03-00	13:00	5 m SW	24.3	34
SAF4	03-20-00	09:40	45 m NE	14.0	27
SAF5	03-20-00	10:10	50 m NE	14.0	50
SAF6	04-29-00	09:25	30 m NE	17.8	13
SAF7	05-03-00	10:26	55 m NE	21.6	53
SAF8	03-20-00	10:35	80 m NE	10.0	14
SAF9	04-29-00	12:45	on fault	18.3	41
SAF10	05-03-00	14:10	20 m SW	22.0	25
SAF11	04-29-00	08:11	50 m SW	14.6	12

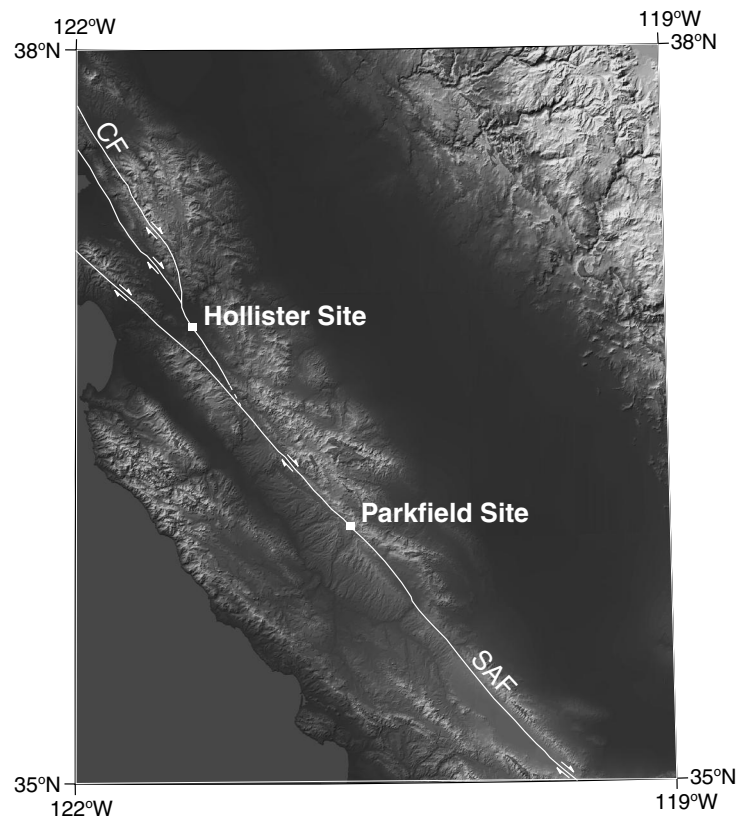


Fig. 8. Shaded relief map of central California showing study site locations along the San Andreas fault (SAF) in Parkfield and Calaveras fault (CF) in Hollister.

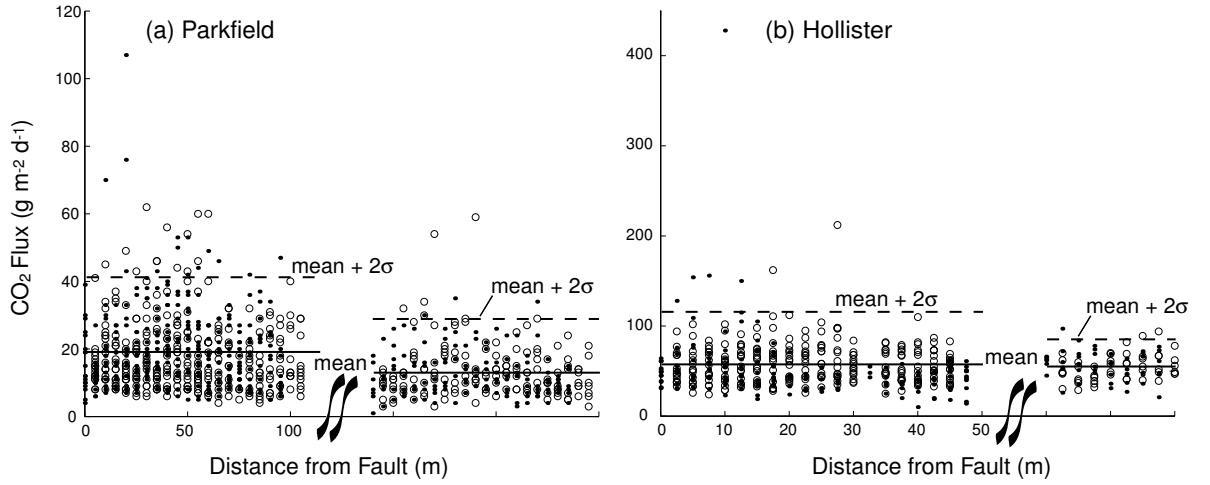


Fig. 9. (a) Plot of CO_2 flux versus distance from the SAF fault trace for SAF (left side of break in x-axis) and PB (right side of break in x-axis) grids. PB grid is located ~ 1.5 km northeast of the SAF grid. SAF grid black dots and open circles are measurements made on northeast and southwest sides of fault trace, respectively. PB grid symbols represent measurements made on either side of a line drawn through the middle of grid. Solid and dashed horizontal lines represent the mean, μ , and $\mu + 2\sigma$, respectively, of SAF and PB grid populations calculated for non-transformed data. (b) Plot of CO_2 flux versus distance from CF fault trace for CF (left side of break in x-axis) and HB (right side of break in x-axis) grids. The HB grid is located ~ 2.5 km southeast of HF grid. CF grid black dots and open circles are measurements made on east and west sides of fault trace, respectively. HB grid symbols represent measurements made on either side of a line drawn through the middle of grid. Solid and dashed horizontal lines represent μ and $\mu + 2\sigma$, respectively, of CF and HB grid populations calculated for non-transformed data.

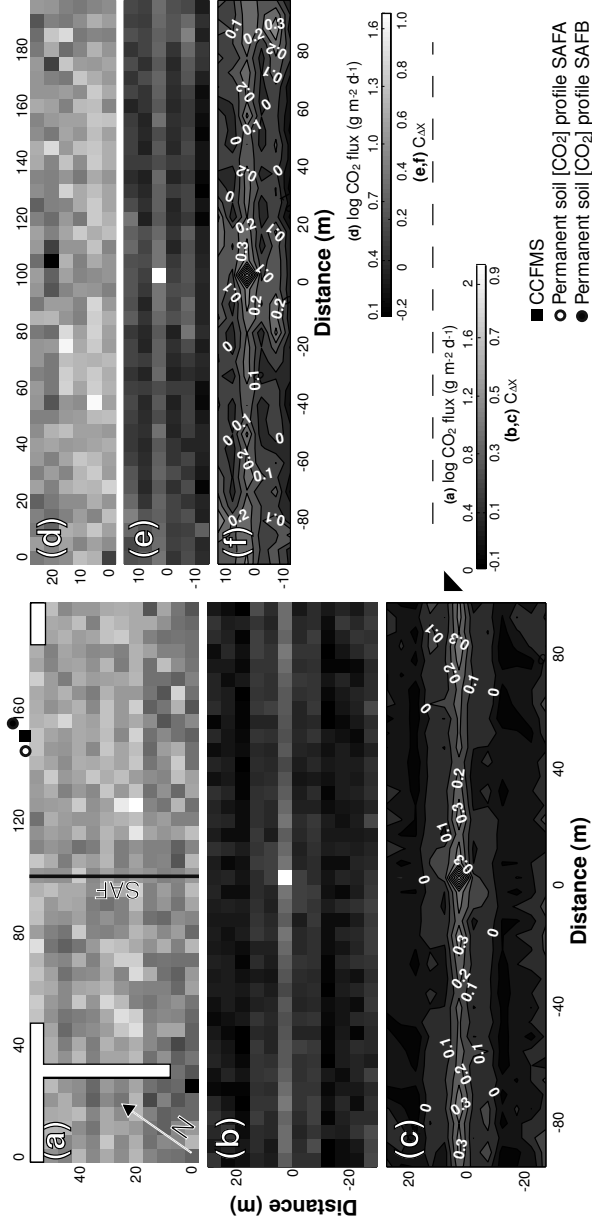


Fig. 10. (a) Image map of SAF grid surface CO₂ flux. Each 5x5 m block represents an flux measurement. White outlined areas show where flux was not measured. (b) Image map of SAF grid CO₂ flux $C_{\Delta X}$. Each block represents a $C_{\Delta X}$ value (Equation 2.2). (c) Map contoured for CO₂ flux $C_{\Delta X}$. (d) Image map of PB grid surface CO₂ flux. (e) Image map of PB grid CO₂ flux $C_{\Delta X}$. (f) Map contoured for CO₂ flux $C_{\Delta X}$.

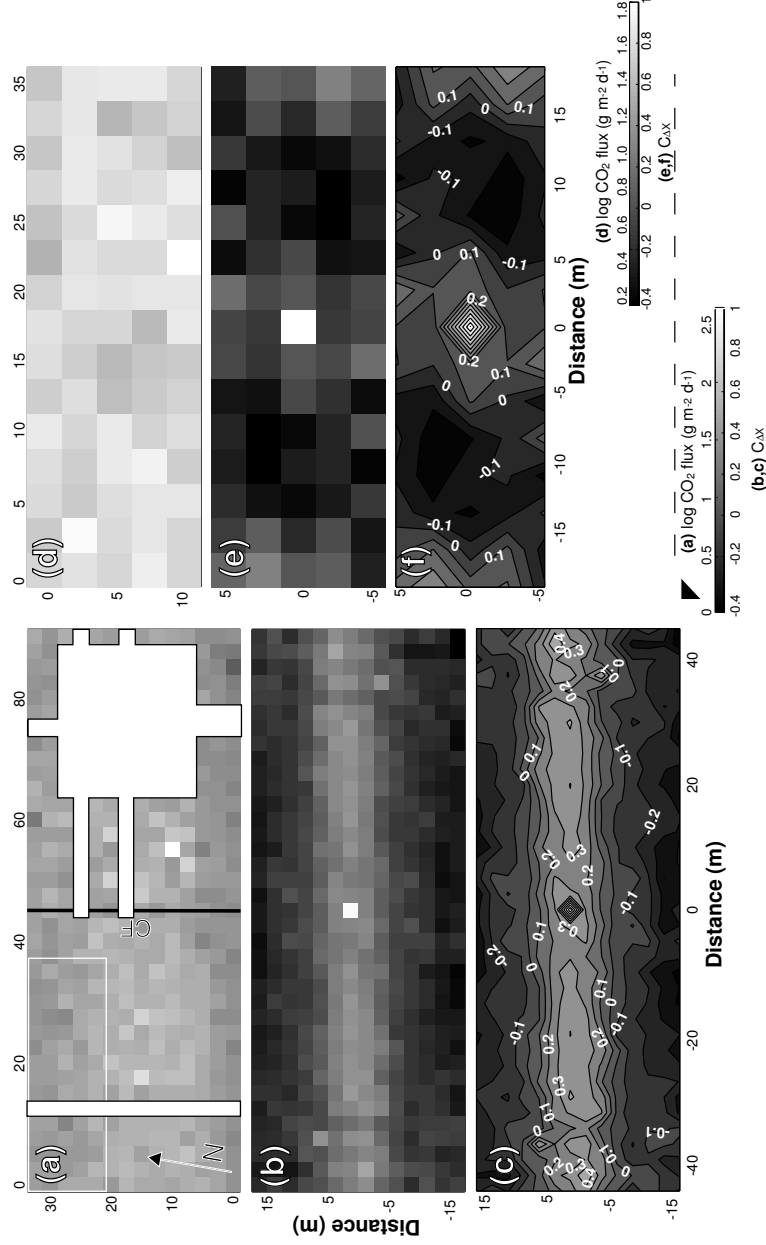


Fig. 11. (a) Image map of CF grid surface CO₂ flux. White outlined areas show where flux was not measured. The white rectangle in the northwest corner of the map represents the HB grid spatial scale. (b) Image map of CF grid CO₂ flux $C_{\Delta X}$. (c) Map contoured for CO₂ flux $C_{\Delta X}$. (d) Image map of HB grid surface CO₂ flux. (e) Image map of HB grid CO₂ flux $C_{\Delta X}$. (f) Map contoured for CO₂ flux $C_{\Delta X}$.

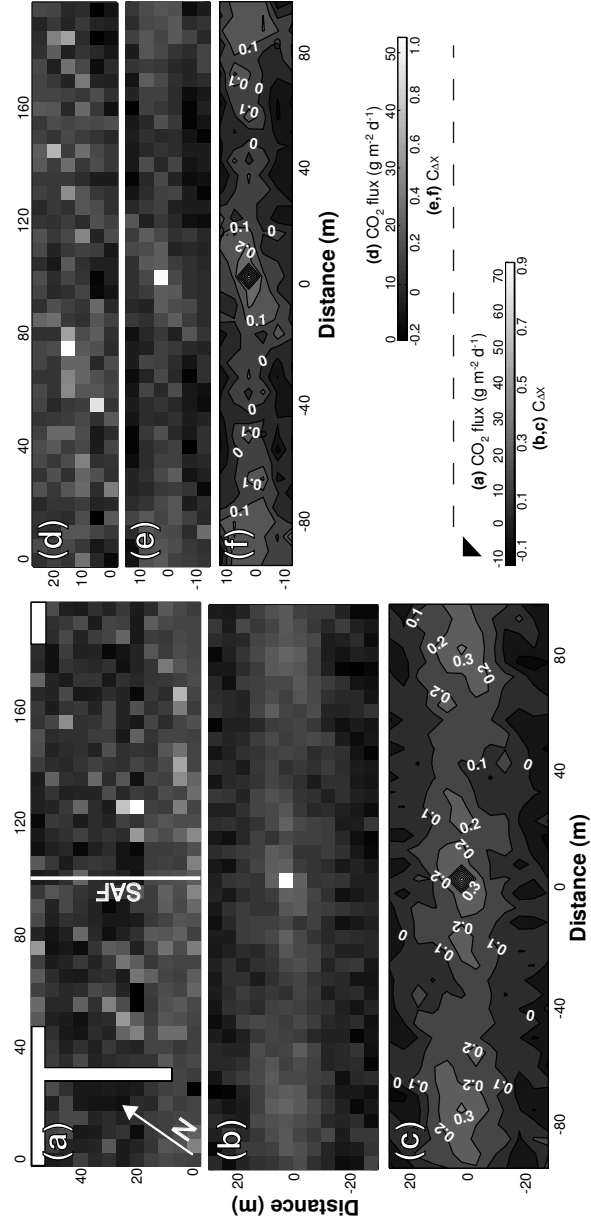


Fig. 12. (a) Image map of SAF grid time-adjusted surface CO_2 flux (see Figure 10a). (b) Image map of SAF grid time-adjusted CO_2 flux $C_{\Delta X}$. (c) Map contoured for time-adjusted CO_2 flux $C_{\Delta X}$. (d) Image map of PB grid time-adjusted surface CO_2 flux. (e) Image map of PB grid time-adjusted CO_2 flux $C_{\Delta X}$. (f) Map contoured for time-adjusted CO_2 flux $C_{\Delta X}$.

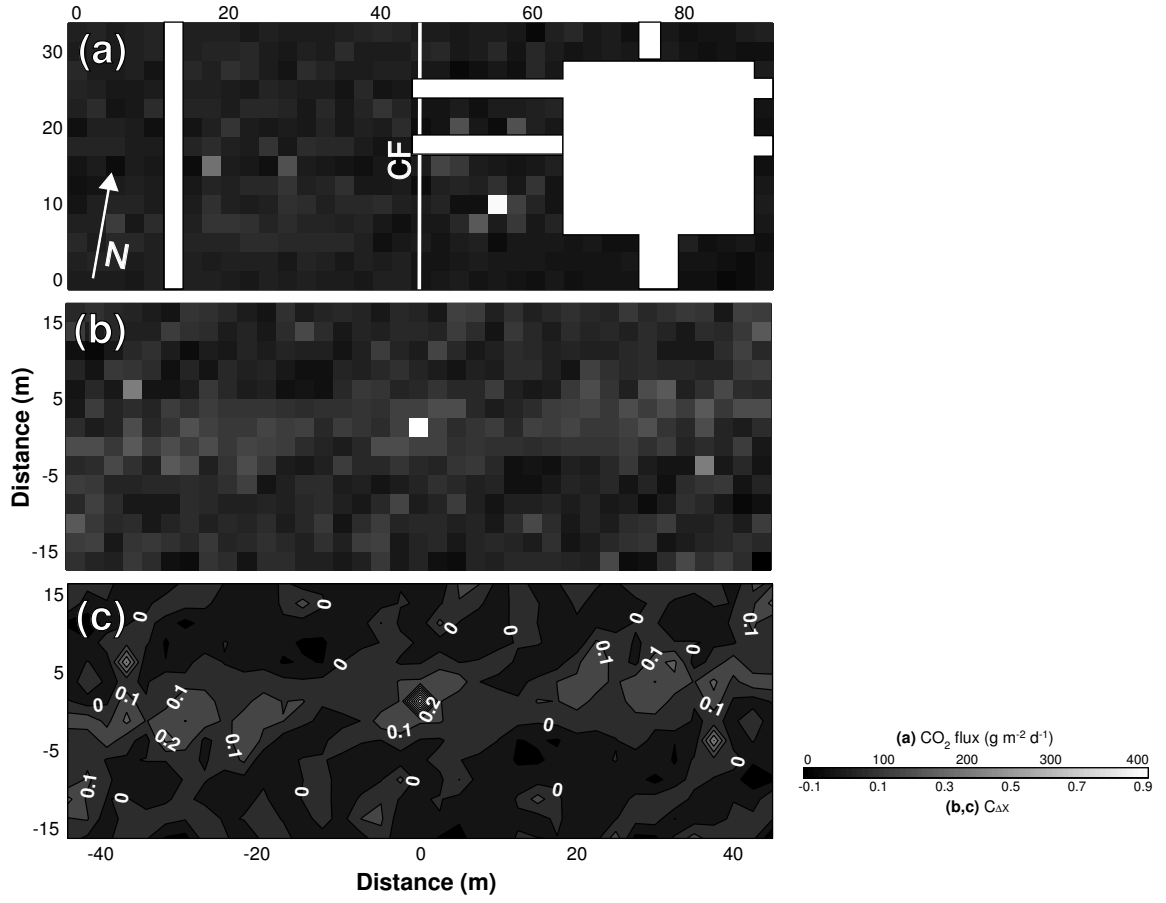


Fig. 13. (a) Image map of CF grid time-adjusted surface CO₂ flux (see Figure 11a). (b) Image map of CF grid time-adjusted CO₂ flux $C'_{\Delta X}$. (c) Map contoured for time-adjusted CO₂ flux $C'_{\Delta X}$.

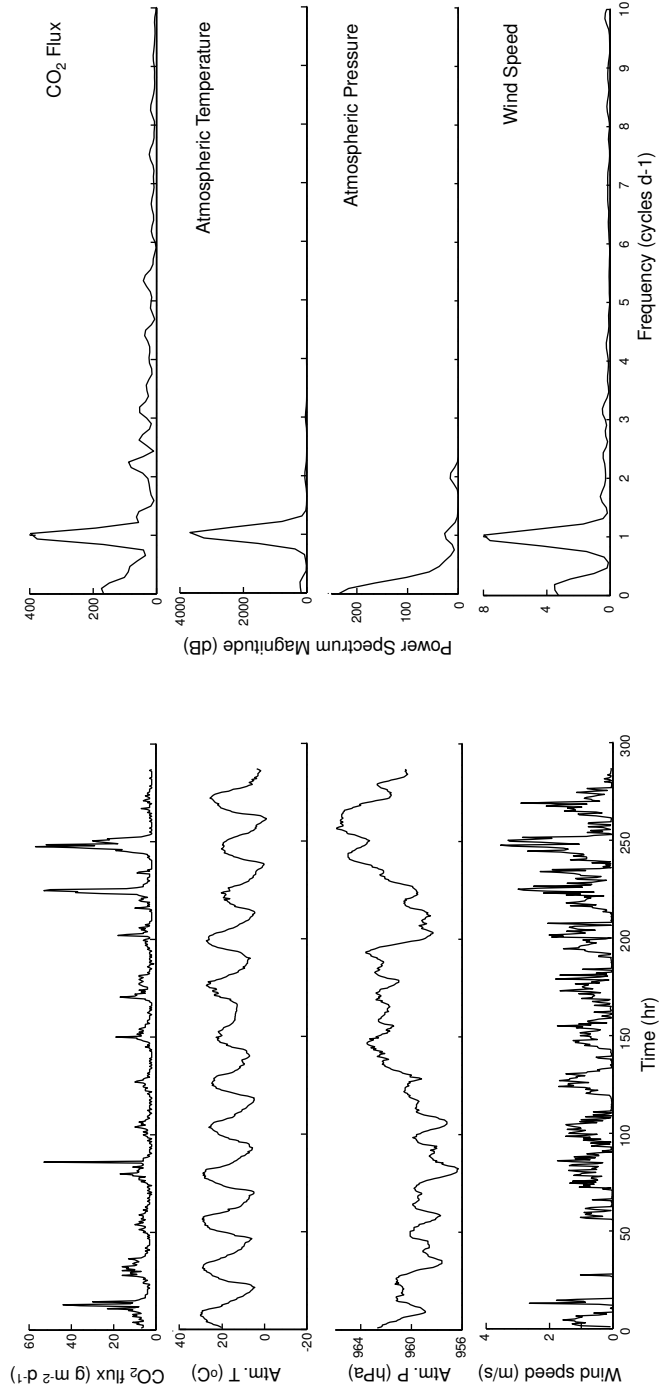


Fig. 14. Time series and power spectra for CCFMS CO₂ flux, atmospheric temperature and pressure, and wind speed measurements at the SAF fractured soil site.

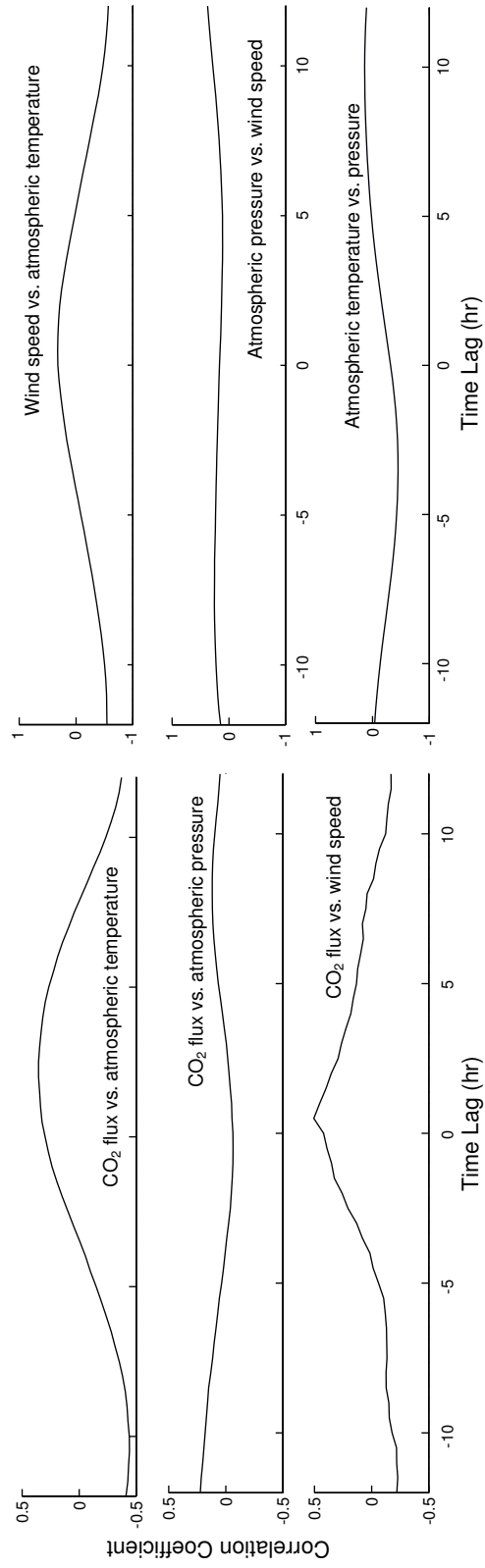


Fig. 15. Plots of correlation coefficients as a function of time lag for CCFMS CO₂ flux and meteorological parameter measurements at the SAF fractured soil site.

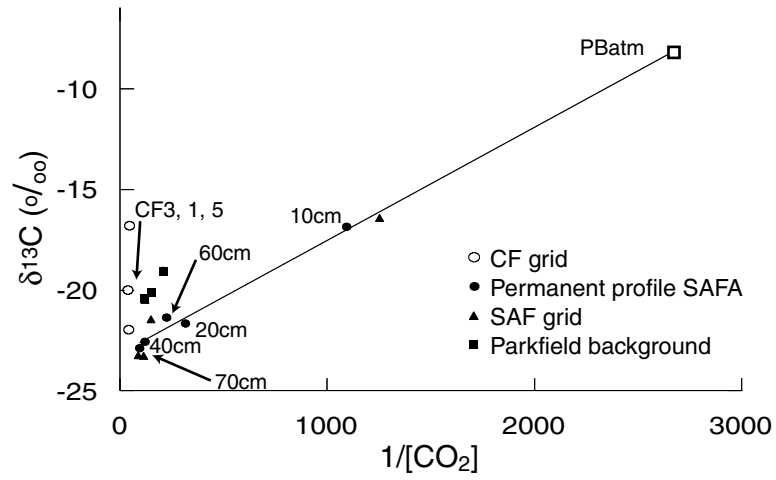


Fig. 16. $\delta^{13}\text{C}$ versus $1/[\text{CO}_2]$ for soil gases collected from SAF and CF grids and Parkfield background area. Permanent $[\text{CO}_2]$ profile SAFA samples were collected from 10 to 70 cm depth on 04-28-00 at 15:15 and lie on a mixing line between the compositions of Parkfield atmospheric air (PBatm) and the soil gas collected at 70 cm depth.

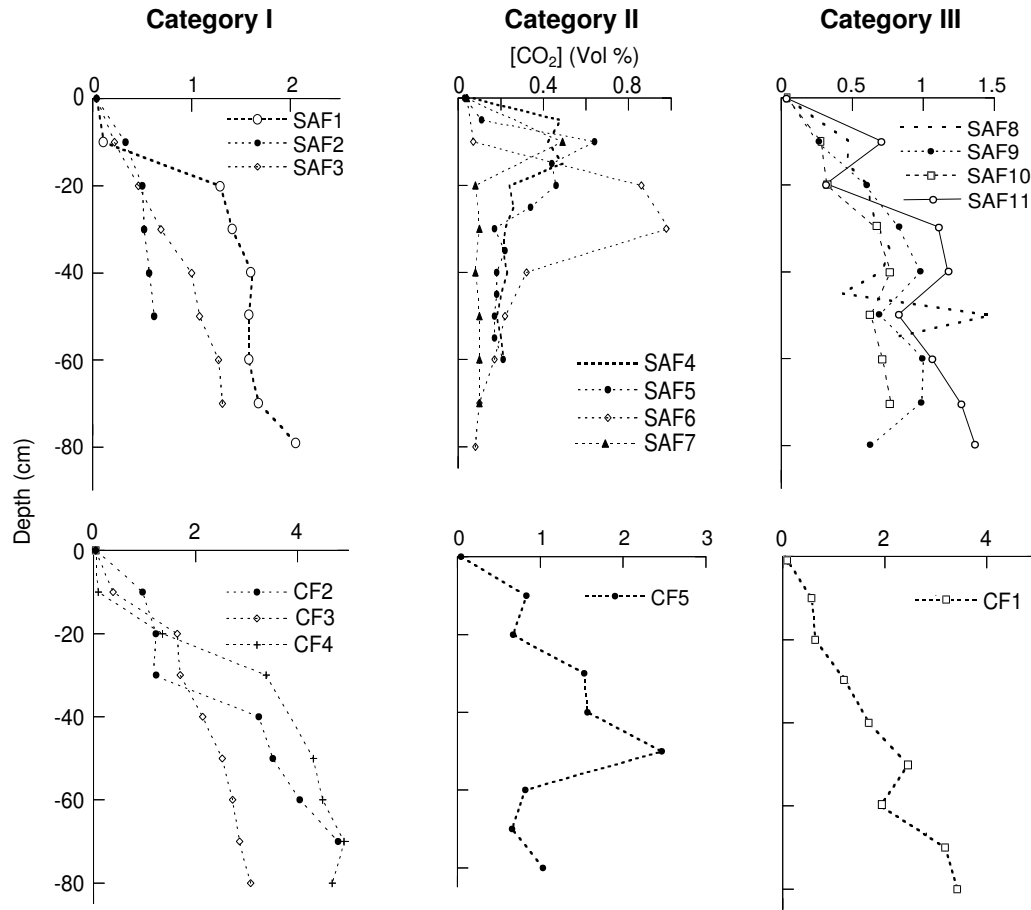


Fig. 17. Soil [CO₂] profiles for SAF and CF survey sites (see Table 4 for profile location, date, time, soil temperature, and corresponding surface CO₂ flux). Category I profiles show [CO₂] increase with depth. Category II profiles exhibit [CO₂] increase followed by decrease with depth. Category III profiles exhibit a "saw-tooth" pattern with repeated increase and decrease in [CO₂] with depth.

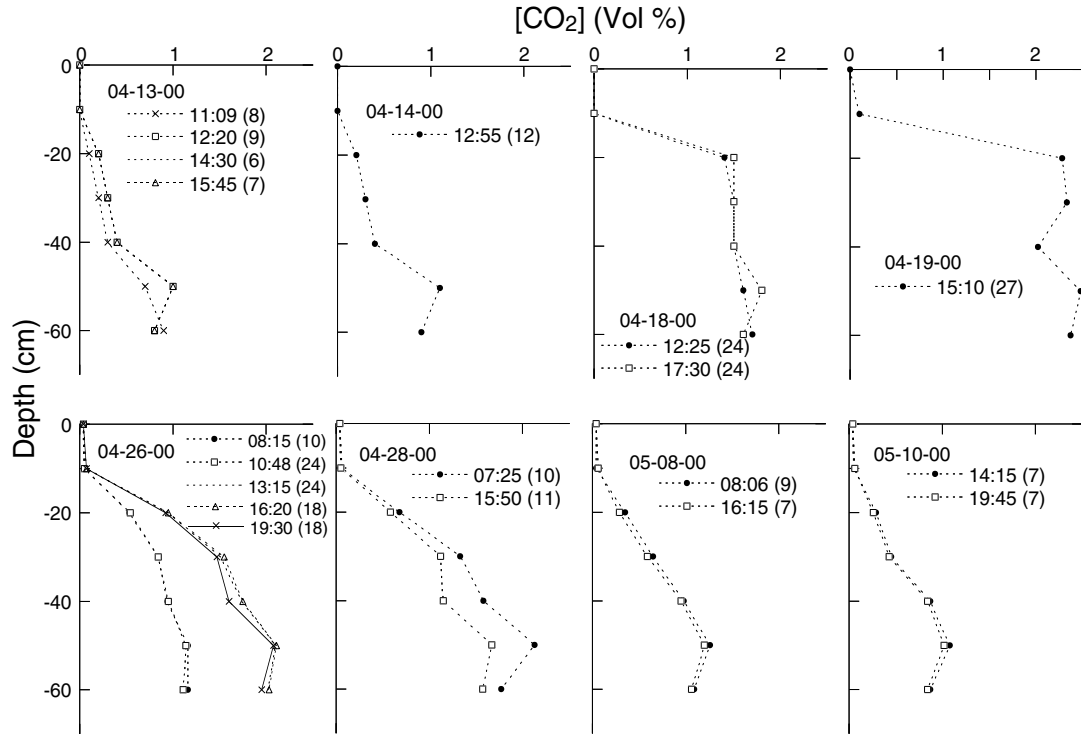


Fig. 18. Temporal variability (04-13-00 to 05-10-00) of permanent soil $[CO_2]$ profile SAFB. Measurement times are shown and corresponding surface CO_2 fluxes, in $g\ m^{-2}\ d^{-1}$, are in parentheses.

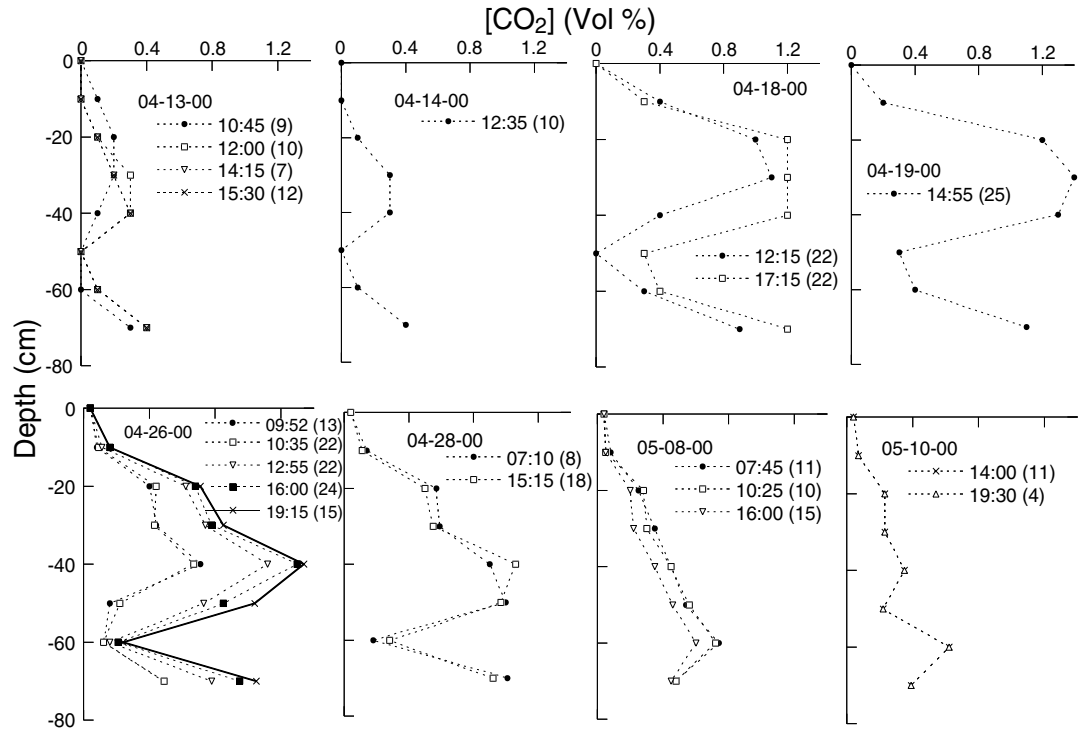


Fig. 19. Temporal variability (04-13-00 to 05-10-00) of permanent soil $[\text{CO}_2]$ profile SAFA. Measurement times are shown and corresponding surface CO_2 fluxes, in $\text{g m}^{-2}\text{d}^{-1}$, are in parentheses. $\delta^{13}\text{C}$ values were measured for soil CO_2 collected from 10 to 70 cm depth at 15:15 on 04-28-00 (see Figure 16).

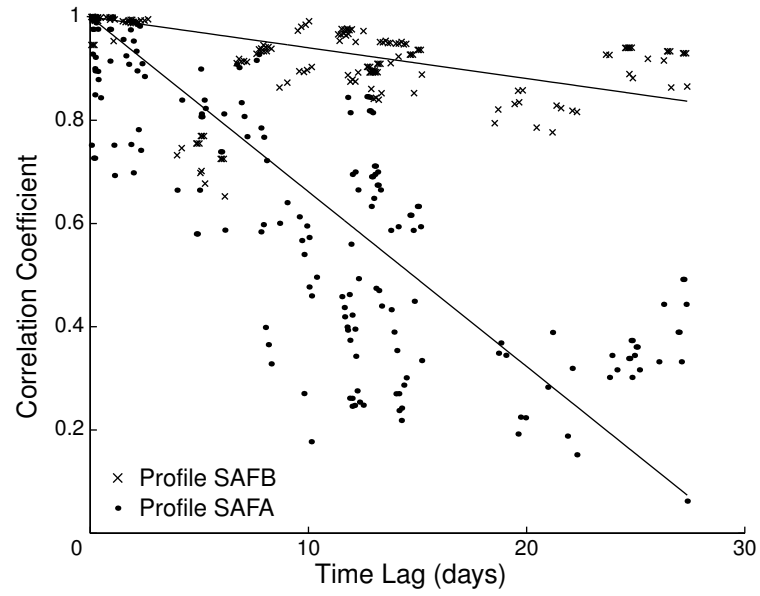


Fig. 20. Plot of correlation coefficients as a function of time lag for permanent soil $[\text{CO}_2]$ profiles SAFB and SAFA. For best-fit lines to SAFB and SAFA profile data, correlation is constrained to be one at zero time lag.

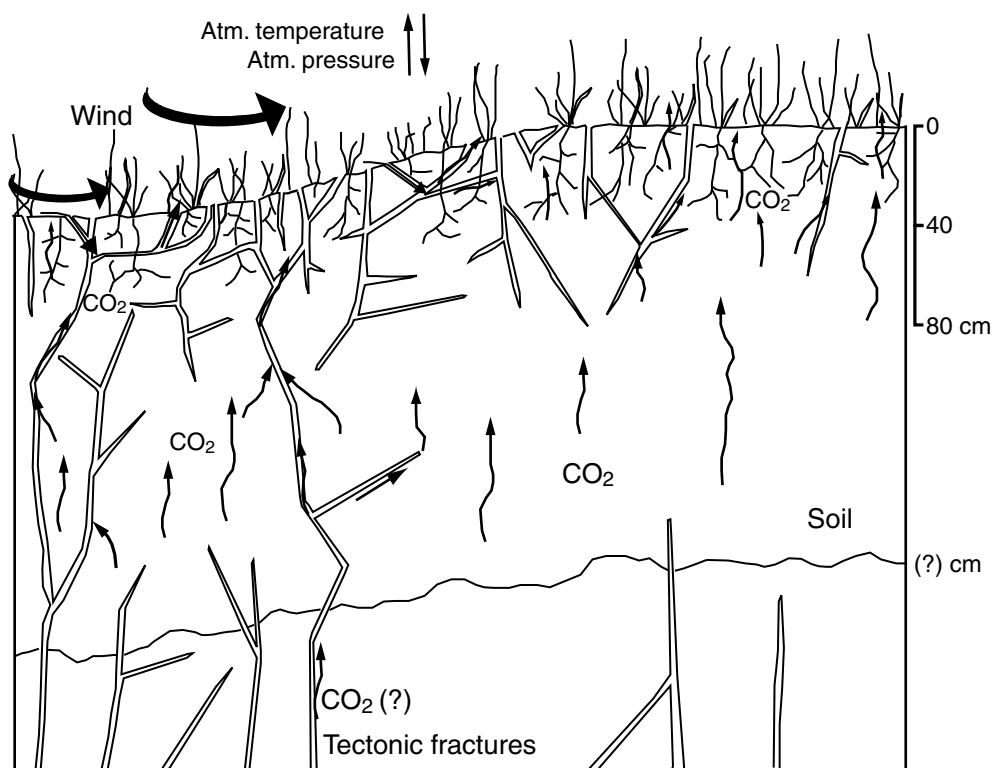


Fig. 21. Schematic of gas flow in fractured terrain showing movement of soil CO₂ to the atmosphere. CO₂ may be derived from root respiration (upper 40 cm at SAF and CF sites), heterotrophic bacteria (through the entire soil column), and, in the case of the CF site, possibly from seasonal groundwater degassing. Highly permeable fractures (tectonic and non-tectonic) are hypothesized to focus and enhance CO₂ flow. Wind, atmospheric and soil temperature, and atmospheric pressure fluctuations may modulate soil diffusive and advective CO₂ transport to the atmosphere by disturbing [CO₂] and total pressure gradients, respectively. In particular, wind-driven atmospheric air flow through fractures is proposed to act as a carrier gas for soil CO₂, enhancing surface CO₂ flux. Soil depth is unknown at SAF and CF sites. Fracture width and density are not to scale.

Chapter 3

Soil CO₂ Flow in Fractured Terrain II: Modeling Advective and Diffusive Transport of CO₂ and Air Through Soils

3.1 Abstract

We tested the response of soil gas transport processes and resulting concentrations as a function of soil depth (referred to hereafter as soil concentration profiles) to changing soil physical properties, biological respiration rates, and boundary conditions using one-dimensional finite difference models of diffusive CO₂ flow and advective-diffusive CO₂ and air flow. When transport is purely diffusive, the shape of CO₂ concentration ([CO₂]) profiles is sensitive to soil CO₂ production rates, CO₂ flux at the base of the soil column, and soil diffusivity. When advective and diffusive transport of CO₂ and air are considered, transport processes operating through the soil column and the geometry of gas concentration profiles are most sensitive to the magnitude and chemical composition of the basal gas flux. These factors are also sensitive to soil diffusivity and permeability; however, when soil permeabilities are large, concentration profile shape is relatively insensitive to changes in permeability. Relative to other model parameters, the processes driving CO₂ transport are less sensitive to soil CO₂ production rate; however, the shape of concentration profiles is highly sensitive to this parameter. The contribution of advective to total CO₂ flow across the soil/air interface is most sensitive to basal gas flux and soil diffusivity; at high basal gas fluxes and low soil diffusivities, advective surface CO₂

flux is important. Where basal gas fluxes with chemical compositions close to that of the atmosphere are maintained, transport of air through the soil column is dominantly advective. In general, the time required for conditions in $[\text{CO}_2]$ and air concentration ($[\text{air}]$) profiles to approximate steady state decreases as the relative advective contribution to flow increases. Because air transport through most soil columns is mainly advective and CO_2 transport is some combination of advection and diffusion, most $[\text{air}]$ profiles reach steady state in less time than $[\text{CO}_2]$ profiles. Results suggest that small magnitude basal gas fluxes (relative to surface wind speeds) can produce total pressure gradients sufficient to drive advective gas flow through soil columns. Therefore, interpretations of soil gas data collected in faulted/fractured terrain should consider the effects of wind-driven airflow through soils on gas transport and resulting soil gas concentration profiles and surface fluxes.

3.2 Introduction

The measurement of soil gas surface fluxes and concentration profiles can be used to evaluate soil gas transport processes in faulted/fractured environments [e.g., *Schery et al.*, 1984; *Etioppe*, 1999; *Rogie et al.*, 2001; *Lewicki et al.*, in review]. In turn, understanding of these processes is important to a variety of geologic and environmental problems. For example, many seismotectonic studies have focussed attention on the measurement of anomalously high soil gas concentrations and fluxes within fault zones, as these anomalies may reflect focussed gas flow from depth to the atmosphere along highly permeable faults and fractures [e.g., *King*, 1986; *Toutain and Baubron*, 1999; *Lewicki and Brantley*, 2000, and references therein]. However, interpretation of these field data may

be complicated by the range of factors that influence gas transport to the atmosphere including soil physical properties and meteorological and biological parameters, and their spatial and temporal variability, which are often poorly constrained in natural systems. As a result, the relative contributions of different transport mechanisms controlling soil gas flow to the atmosphere in fractured terrain are largely unknown.

Lewicki et al. [in review] presented the results of soil CO₂ surveys conducted along the San Andreas fault (SAF) in Parkfield, CA, and the Calaveras fault (CF) in Hollister, CA. They examined how soil CO₂ transport processes, and the resulting soil [CO₂] profiles and surface fluxes were affected by pervasively fractured soil and temporal variation of meteorological parameters. *Lewicki et al.* [in review] measured CO₂ flux within grids with portable instrumentation, and continuously at a fixed station with meteorological parameters, in both faulted and unfaulted background areas. In addition, they measured soil [CO₂] profiles at multiple sites within SAF and CF grids (Figure 22) and repeatedly over time at two locations at the SAF grid. *Lewicki et al.* [in review] found that the areal distribution of soil CO₂ flux was highly variable in space and time at their study sites and regions of enhanced flux appeared to be related to subsurface fracturing on small spatial scales. Soil [CO₂] profiles indicated a surprisingly high component of pressure-driven (advective) CO₂ flow in soil columns (accounting for up to 85% of total surface fluxes) that varied spatially within study areas and temporally at individual locations. Interestingly, time series of surface CO₂ fluxes and meteorological parameters showed CO₂ fluxes to be positively correlated with wind speed, suggesting that wind may strongly influence this pressure-driven soil CO₂ flow. Based on these field observations, *Lewicki et al.* [in review] proposed a conceptual model for soil gas flow at their study

sites (Figure 23), in which biogenic CO_2 flow is focused in highly permeable tectonic and non-tectonic fractures and modulated by temporal fluctuations in meteorological parameters. However, their work also illustrated the complexity of gas flow in fractured soils and the need to characterize the relative importance of specific physical processes and soil properties in this transport with numerical experiments where the number of variables influencing gas transport could be controlled.

We use one-dimensional steady state finite difference models of diffusive CO_2 flow and combined advective-diffusive two-component (CO_2 and air) flow to develop a fundamental understanding of the conditions under which diffusive and/or advective flow may be important agents of gas transport in the soil. We explore the effects of different soil physical properties, biological production rates, and boundary conditions on the relative importance of the gas transport mechanisms under a range of physically diverse conditions. In addition, we study the impact of these parameters on $[\text{CO}_2]$ profile geometry. In this way, we test the feasibility of *Lewicki et al.* [in review]’s basic interpretations by determining if their different field observations (e.g., surface CO_2 fluxes, $[\text{CO}_2]$ profiles, time-series of both, and isotopic measurements) are internally consistent and support a significant component of advective gas flow through the soil column. In addition, our results provide a guide for future soil gas field studies in faulted/fractured terrain to test the importance of advective flow and provide a basis for the development of multi-dimensional models that may be used to gain insight into the nature of soil gas flow in complex heterogeneous porous media typical of faulted/fractured areas.

3.3 Gas Transport Models

Extensive field, laboratory, and numerical work has been conducted to investigate unsaturated zone gas transport and the models developed for the study of this transport have varied in complexity, data requirements, and usefulness (see, e.g., *Thorstenson and Pollock* [1989], *Scanlon et al.* [1999] for reviews of this work). In our study, we use steady state, one-dimensional diffusive and advective-diffusive transport models to investigate gas flow in fractured media. Our one-dimensional modeling approach approximates gas flow in a soil column that has little or no lateral flow, and so all gas introduced at the base of or produced within the soil column may be only transported up or down. This simple model permits us to examine the basic properties of gas flow and the sensitivity of this flow to changing system parameters under conditions that limit the number of varying factors that may potentially influence transport processes. Also, measured soil $[\text{CO}_2]$ profiles [*Lewicki et al.*, in review] are themselves one-dimensional data and therefore provide limited information about lateral flow that may result from spatial variation in the soil system parameters. Our use of steady state models prevents us from considering the temporal development of gas concentrations and fluxes in soil profiles; however, it allows us to neglect the initial conditions in soil gas concentration profiles, which may be difficult to infer in natural soils. Also, it permits us to understand the state toward which all transient concentration profiles, fluxes, and transport mechanisms will evolve.

3.3.1 General formulation

3.3.1.1 Diffusive transport

The first soil gas transport process we consider is molecular diffusion. This transport occurs when equimolar pairs of gases (i, j) counterdiffuse to reduce their concentration gradients. Fick's law can be used to predict the molar diffusive flux of gas i (Q_i^D , mol L⁻²t⁻¹) resulting from molecular diffusion of i in j in an isothermal and isobaric system [e.g., *Bird et al.*, 1960] (see Table 5 for all parameter notation):

$$Q_i^D = -D_i^* \frac{\partial C_i}{\partial z} \quad (3.1)$$

where D_i^* is the diffusion coefficient for i in soil (L²t⁻¹), C_i is the molar density of i in soil air (mol L⁻³) and z is soil depth (L). According to Fick's law, the diffusive flux of gas i is proportional to its concentration gradient in the soil and D_i^* . D_i^* varies with the binary diffusion coefficient for gas i in j at a given soil temperature (D_{i-j} , L²t⁻¹), soil air-filled porosity (n_a), and soil tortuosity (τ):

$$D_i^* = D_{i-j} n_a \tau \quad (3.2)$$

When the total flux of gas i across a unit area (Q_i^T , mol L⁻²t⁻¹) in the soil increases along a flow path from point z to point $z + \partial z$, the concentration of i (C_i) must decrease, as more gas leaves the volume than enters. Conversely, when the flux decreases, the concentration must increase as gas accumulates in the volume. In addition, production of gas i in the soil column will increase C_i . Therefore, the mass conservation

law requires that the temporal change in C_i ($\partial C_i / \partial t$) is equal to the production rate of i in the soil column (ϕ , mol L⁻³t⁻¹) minus the spatial change in Q_i^T ($\partial Q_i^T / \partial z$):

$$\frac{\partial C_i}{\partial t} = -\frac{\partial Q_i^T}{\partial z} + \phi \quad (3.3)$$

When i is only transported by molecular diffusion, $Q_i^T = Q_i^D$ and we may combine Equations 3.1 and 3.3 to express the rate of change in i as a function of the second spatial derivative of i :

$$\frac{\partial C_i}{\partial t} = D_i^* \frac{\partial^2 C_i}{\partial z^2} + \phi \quad (3.4)$$

Equation 3.4 shows that the rate of change of C_i ($\partial C_i / \partial t$) is proportional to the curvature of the concentration profile ($\partial^2 C_i / \partial z^2$). Over time, molecular diffusion acts to minimize the curvature of the concentration profile. When boundary conditions and internal production are fixed for a long period of time, the system will reach a steady state condition, where the spatial changes in the diffusive fluxes in the soil column will be balanced by the production of gas in the column and the rate of change in concentration at all points will equal zero:

$$\frac{\partial C_i}{\partial t} = 0 = D_i^* \frac{\partial^2 C_i}{\partial z^2} + \phi \quad (3.5)$$

Equation 3.5 can be integrated with respect to time to solve for steady-state $C_i(z)$ soil profiles.

3.3.1.2 Advective-diffusive transport

If a total pressure gradient ($\partial P/\partial z$, $\text{M L}^{-2}\text{t}^{-2}$) exists in the soil as a result of external forces (e.g., fluctuations in barometric pressure, wind, or soil temperature), advective gas flow from high to low total pressure will occur [e.g., *Massmann and Farrier*, 1992; *Holford et al.*, 1993]. The total pressure gradient is the driving force of advective gas flow and studies have shown that the presence of small total pressure gradients in the soil may produce advective fluxes that overwhelm diffusive fluxes [e.g., *Thorstenon and Pollock*, 1989]. The advective flux of gas i is proportional to its partial pressure in the bulk gas (P_i , $\text{M L}^{-1}\text{t}^{-2}$) and the soil intrinsic permeability (B_k , L^2) and inversely proportional to its viscosity (μ , $\text{M L}^{-1}\text{t}^{-1}$). If both partial and total pressure gradients exist in the soil, combined advective and diffusive gas transport will result and may be described by the advection-diffusion equation [e.g., *Sleep and Skyes*, 1989; *Abriola et al.*, 1992]:

$$(RT)Q_i^T = -D_i^* \frac{\partial P_i}{\partial z} - \frac{B_k P_i}{\mu} \frac{\partial P}{\partial z} \quad (3.6)$$

where R is the ideal gas constant ($\text{M L}^2\text{t}^{-2}\text{T}^{-1}\text{mol}^{-1}$), T is temperature, and D_i^* is the diffusion coefficient (L^2t^{-1}) of the i^{th} component. Equation 3.6 states that the total flux of species i is the sum of the diffusive (left term) and advective (right term) gas flows. In a two-component (i, j) gas mixture, i and j will flow from points of high to low P . As $P = P_i + P_j$, the total pressure gradient explicitly links the flow of the two components. Superimposed on this advective gas flow is counterdiffusion of components i and j from points of high to low partial pressures. If the partial and total pressure

gradients are in opposite directions, the net magnitude and direction of the flux of a given gas component will depend on the relative magnitudes of these partial and total pressure-driven flows.

The mass conservation law can be expressed as in Equation 3.3 if the bulk gas is assumed incompressible (constant mass density). Using this assumption, we combine Equations 3.6 and 3.3 to yield:

$$\frac{\partial C_i}{\partial t} = \frac{\partial}{\partial z} \left[\frac{-D_i^* \frac{\partial P_i}{\partial z} - \frac{B_k P_i}{\mu} \frac{\partial P}{\partial z}}{RT} \right] + \phi \quad (3.7)$$

Equation 3.7 relates the relative contributions of diffusive and advective gas flow of component i through the soil column to the system initial and boundary conditions, soil ϕ , and time evolution of the gas flow. When the system reaches steady state, $\partial C_i / \partial t = 0$ and at any given point in the soil column, the sum of the diffusive and advective fluxes of i will equal the sum of the production rate of i integrated over the soil column below that point and the flux of i applied to the base of the soil column. We use equations 3.3, 3.6, and 3.7 to model two-component advective-diffusive gas transport.

3.3.2 Solution methods

3.3.2.1 Analytical solution for steady state diffusion model

In the case of diffusive transport of CO_2 , concentrations and fluxes within the soil column through time depend on the initial profile CO_2 concentrations (at $t = 0$), soil ϕ , the $[\text{CO}_2]$ at the soil surface ($C_{\text{CO}_2}^o$), and the CO_2 flux entering the base of the soil column ($F_{\text{CO}_2}^B$). Under steady state conditions, Equation 3.5 (written for diffusion of

CO₂ in air) is solved analytically to yield C_{CO_2} as a function of soil depth z in a soil column of thickness L (see Appendix I for complete derivation). In our diffusive steady state models, we consider the case in which CO₂ production rate (ϕ) may vary with depth. This represents the situation where soil ϕ is concentrated within a shallow grass root zone or extends deeper in the soil due to microbial respiration [e.g., *Amundson and Davidson*, 1990; *Wood et al.*, 1993]. We consider two soil layers that may have different production rates (ϕ_1 and ϕ_2 for the upper and lower layers, respectively). Variation of $F_{CO_2}^B$ approximates CO₂ flow derived from groundwater degassing, oxidation of organic matter in the subsoil, or atmospheric airflow through soil. In all models, we assume that $C_{CO_2}^o$ is constant and equal to atmospheric [CO₂], likely in the case of a well-mixed atmosphere above relatively low CO₂ emission terrain.

We solve Equation 3.5 for the case where CO₂ is produced in the soil at constant rates ϕ_1 and ϕ_2 through soil column layers with thickness L_1 and L_2 , respectively (Figure 24a), where

$$L = L_1 + L_2 \quad (3.8)$$

and the following boundary conditions exist

$$\text{at } z = 0, \quad C_{CO_2} = C_{CO_2}^o \quad (3.9)$$

$$\text{at } z = -L, \quad Q_{CO_2}^D = F_{CO_2}^B \quad (3.10)$$

We solve for $Q_{CO_2}^D$ as a function of z by piecewise integration of the mass conservation equation (Equation 3.3) from $-L$ to $-L_1$ and from $-L_1$ to the soil surface. To determine $Q_{CO_2}^D(z)$ in the lower soil layer, we integrate Equation 3.3, letting $\phi = \phi_2$, and solve for the constant of integration by requiring the flux at $-L$ to equal $F_{CO_2}^B$ (Equation 3.10):

$$Q_{CO_2,2}^D(z) = \phi_2 z + \phi_2(L_1 + L_2) + F_{CO_2}^B \quad (3.11)$$

To find $Q_{CO_2}^D(z)$ in the upper soil layer, we first integrate Equation 3.3, letting $\phi = \phi_1$. We then merge the top and bottom layers of the model by requiring the flux leaving the top of the bottom layer to equal that entering the bottom of the top layer:

$$Q_{CO_2,1}^D(z) = \phi_1(z + L_1) + \phi_2 L_2 + F_{CO_2}^B \quad (3.12)$$

Next, we solve for $C_{CO_2}(z)$ in the upper soil layer using Fick's law (Equation 3.1) by integrating, implementing the upper boundary condition (Equation 3.9), and combining this with the expression for the steady state flux (Equation 3.12):

$$C_{CO_2,1}(z) = -\frac{z}{D_i^*} \left[\frac{\phi_1}{2} z + \phi_1 L_1 + \phi_2 L_2 + F_{CO_2}^B \right] + C_{CO_2}^o \quad (3.13)$$

We then find $C_{CO_2}(z)$ in the lower soil layer by substituting Equation 3.11 into Fick's law (Equation 3.1) and integrating:

$$C_{CO_2,2}(z) = -\frac{z}{D_i^*} \left[\frac{\phi_2}{2} z + \phi_2(L_1 + L_2) + F_{CO_2}^B \right] + c_4 \quad (3.14)$$

We solve for the constant of integration (c_4) by requiring continuity of the concentrations within the profile ($C_{CO2,2} = C_{CO2,1}$ at $z = -L_1$) and then substituting into Equation 3.14:

$$C_{CO2,2}(z) = -\frac{z}{D_i^*} \left[\frac{\phi_2}{2}z + \phi_2(L_1 + L_2) + F_{CO2}^B \right] + \frac{L_1}{D_i^*} \left[\frac{\phi_1 L_1}{2} - \frac{\phi_2 L_1}{2} \right] + C_{CO2}^o \quad (3.15)$$

Equations 3.13 and 3.15 are used to calculate steady state soil $[CO_2]$ profiles for cases where ϕ_1 and ϕ_2 are constant within each soil layer, F_{CO2}^B is constant, and C_{CO2}^o is fixed at the soil surface.

3.3.2.2 Numerical solution of steady state advection-diffusion and transient diffusion and advection-diffusion models

In the case of combined advective and diffusive gas transport, one-dimensional equations (Equations 3.3, 3.6, and 3.7) for CO_2 and air are solved simultaneously by a forward finite difference adaptive time integration algorithm to yield $C_{air}(z)$ and $C_{CO2}(z)$. In this scheme, equations are differentiated with respect to space along even intervals in the model domain according to

$$\frac{\Delta A}{\Delta z} \left[z + \left(\frac{\Delta z}{2} \right) \right] \simeq \frac{[A(z + \Delta z) - A(z)]}{\Delta z} \quad (3.16)$$

[Shampine and Gordon, 1975] where $A = C_i$ or Q_i . Equations are integrated with respect to time depending on the rate of change of the solution at a given time. An explicit Runge-Kutta solution method is used to ensure model stability and accurate

solutions. The C_{air} and C_{CO_2} at the soil surface (C_{air}^o and $C_{CO_2}^o$, respectively) were fixed to atmospheric values (Figure 24b). At the base of the one m thick soil column, constant molar fluxes of air (F_{air}^B) and CO_2 ($F_{CO_2}^B$) were maintained. Initial model conditions were specified as C_{air} and C_{CO_2} equal to atmospheric values at each point in the column. Soil CO_2 was produced at constant rates ϕ_1 and ϕ_2 through soil column layers with thicknesses L_1 and L_2 , respectively.

Equations 3.3, 3.6, and 3.7 are solved for $C_{air}(z)$ and $C_{CO_2}(z)$ in several steps. The model domain space is divided into n nodes with initial condition C_i values at nodes. First, nodes are spatially differentiated and $n - 1$ fluxes between nodes are calculated according to Equation 3.6. The lower boundary condition is set to F_i^B . C_i^o is maintained at the model surface by setting the surface flux of gas i equal to the flux directly below the upper (surface) node, yielding $n + 1$ fluxes in the model domain space. Next, fluxes are differentiated in space to determine $\partial C_i / \partial t$ (Equation 3.3) and ϕ is added to these values at each time step. Third, we integrate Equation 3.7 with respect to time to find the change of C_i and determine $C_{air}(z)$ and $C_{CO_2}(z)$. Equations 3.3, 3.6, and 3.7 are solved for 10^{10} s (317.1 y) of model time to ensure steady state conditions.

To estimate the amount of time required for diffusion and advection-diffusion models to reach steady state, the average rate of change of mass of species i ($\partial M_i / \partial t$) for model domains as a function of model run time is calculated. At evenly spaced time intervals during each model run, the difference between M_i at time t and M_i at time $t + \partial t$ (∂M_i) is calculated at each node in the model domain and the root-mean-squared ∂M_i value is determined and normalized by ∂t . This value is used to gauge how quickly the model solution, and hence, the gas flow, changes in time. When $\partial M_i / \partial t$ values

are relatively high, concentrations and fluxes within the soil column reflect both the boundary and initial pressures in the column at $t = 0$, whereas when values are relatively low (i.e., approach zero) steady state conditions are likely approximated. We define the model response time as the model run time at which $\partial M_{CO_2}/\partial t = 10^{-10} \text{ g s}^{-1}$.

3.3.3 Model Parameters

Parameters used in diffusion and advection-diffusion gas flow models are given in units of g, cm, and s in Tables 6 and 7. For reference, the molecular weights of CO_2 and air used in calculations are shown in Table 6. The temperature of the gas system in all cases was 25°C . In the case of two-component (air and CO_2) advection-diffusion models, air was treated as a gas mixture of 78% N_2 , 21% O_2 , and 1% Ar, by volume. The total, partial air, and partial CO_2 surface (atmospheric) pressures were held constant at $1,013,250 \text{ g cm}^{-1}\text{s}^{-2}$ (approximately 1 atm), $1,012,845 \text{ g cm}^{-1}\text{s}^{-2}$, and $405 \text{ g cm}^{-1}\text{s}^{-2}$, respectively. Soil B_k and D_i^* , ϕ , $F_{CO_2}^B$, F_{air}^B , and $[CO_2]$ of the total basal gas flux (F_T^B) were varied over low, medium, and high values. Soil D_i^* values were varied from 0.00306 to $0.07662 \text{ cm}^2\text{s}^{-1}$ and correspond to $n_a\tau$ values from 0.02 to 0.5 ($D_{CO_2-air}=0.15323 \text{ cm}^2\text{s}^{-1}$ at 25°C , *Marrero and Mason* [1972]), the range most frequently quoted in the literature for air-dry soils [e.g., *Glinski and Stepniewski*, 1985]. Soil B_k was varied from 10^{-13} to 10^{-4} cm^2 . These values encompass the B_k range of most natural soils/sediments (i.e., from unweathered marine clay to gravel, *Freeze and Cherry* [1979]).

We varied $F_{CO_2}^B$ and F_{air}^B simultaneously from low to high values, fixing $[CO_2]$ of the air- CO_2 gas mixture to 0.04 vol.%. This simulates airflow through a soil

fracture with a top that ends at the base of our soil column. The mass flux of air through fractured soils at the SAF and CF study sites is unknown. We therefore varied F_T^B over a range of values that may contribute a reasonable corresponding range in $F_{CO_2}^B$ (2.31×10^{-10} to 2.31×10^{-8} g cm⁻²s⁻¹), when a gas with [CO₂] = 0.04 vol.% flows into the bottom of the soil column. Assuming a density of dry air at 25°C equal to 1.19×10^{-3} g cm⁻³, these F_T^B values correspond to wind speeds of 3.20×10^{-4} to 3.20×10^{-2} cm s⁻¹. For reference, the mean wind speed measured by *Lewicki et al.* [in review] over a one month period (sample frequency equal to one sample every 30 minutes) at the SAF site was 66.8 cm s⁻¹, significantly higher than the values we use in models. The [CO₂] of F_T^B was then varied from 0.04 to 1.0 vol.%, similar to the range of [CO₂] values measured by *Lewicki et al.* [in review] at the base of [CO₂] profiles at the SAF and CF sites (Figure 22), while fixing $F_{CO_2}^B$ to 2.31×10^{-9} g cm⁻²s⁻¹.

Soil ϕ was varied over a one-m thick soil column in five cases: 1) ϕ_1 for $L_1 = 20$ cm and $\phi_2 = 0$, with F_T^B ; 2) ϕ_1 for $L_1 = 40$ cm and $\phi_2 = 0$, with F_T^B ; 3) ϕ_1 for $L_1 = 40$ cm and ϕ_2 for $L_2 = 60$ cm at one third the rate of ϕ_1 , with F_T^B ; 4) ϕ_1 for $L_1 = 20$ cm and $\phi_2 = 0$, without F_T^B ; 5) ϕ_1 for $L_1 = 40$ cm and ϕ_2 for $L_2 = 60$ cm at one third the rate of ϕ_1 , without F_T^B . In each of these cases, the total CO₂ flux resulting from soil ϕ integrated over the soil column ranged from 1.50×10^{-8} to 6.37×10^{-8} g cm⁻²s⁻¹. The low and high CO₂ flux values correspond to the means of the CO₂ flux populations measured by *Lewicki et al.* [in review] within grids at off-fault background study sites in Parkfield and in Hollister, CA, respectively. Soil ϕ values are unknown at *Lewicki et al.* [in review]'s study sites and are likely variable in space and time. We therefore use a range of ϕ values in models that, when integrated over a 1 m

thick soil column, equal the lowest (Parkfield) and highest (Hollister) mean CO₂ fluxes of background study site populations.

We examine the influence of each of the system parameters on steady state [CO₂] and [air] profile shapes and relative contribution of advective versus diffusive gas flux through the soil column. Therefore, as each parameter was varied, all other parameters were held constant at their medium values (with the exception of the set of models in which [CO₂] of F_T^B was maintained at its low value (0.04 vol.%) as B_k , D_i^* , ϕ , and F_T^B were varied).

In diffusion-only models, total surface and soil column pressure were held constant at 1,013,250 g cm⁻¹s⁻² and CO₂ partial pressure at the surface was held constant at 405 g cm⁻¹s⁻². Soil D_i^* was varied as described for advection-diffusion models with ϕ_1 ($L_1 = 40$ cm) constant at its medium value, $\phi_2 = 0$, and no $F_{CO_2}^B$. Soil ϕ was varied in the following cases with soil D_i^* held at its medium value without $F_{CO_2}^B$: 1) ϕ_1 for $L_1 = 20$ cm and $\phi_2 = 0$; 2) ϕ_1 for $L_1 = 40$ cm and $\phi_2 = 0$; 3) ϕ_1 for $L_1 = 40$ cm and ϕ_2 for $L_2 = 60$ cm (one third the rate of ϕ_1). In each of these cases, ϕ was varied over the range described for advection-diffusion models. $F_{CO_2}^B$ was varied (without air) over the same range as in advection-diffusion models, first without soil CO₂ production and then with constant ϕ_1 ($L_1 = 40$ cm) fixed at its medium value.

3.4 Results

3.4.1 Diffusion-only models

We examine the influence of each of the system parameters on steady state soil $[\text{CO}_2]$ profile geometry when CO_2 is transported through the soil column by molecular diffusion in air (Figure 25). At steady state, at any given point in the soil column, the $[\text{CO}_2]$ gradient must be such that all CO_2 produced below that point in the soil column is removed by upward diffusion. Soil ϕ produces profile curvature, whereas $F_{\text{CO}_2}^B$ controls profile slope. In all steady state $[\text{CO}_2]$ profiles modeled, $[\text{CO}_2]$ increases or remains constant with depth. Maximum $[\text{CO}_2]$ in soil columns ranges from approximately 0.05 to 4.5 vol.%, except in the case of low soil D_i^* (Figure 25a), where $[\text{CO}_2]$ reaches approximately 15 vol.%.

Figure 25a shows the effect of decreasing D_i^* . The surface CO_2 flux in each of these cases is the same; therefore, the near-surface $[\text{CO}_2]$ gradient increases as D_i^* decreases. In Figures 25b-d, we explore the effects of changing production rate and production zone geometry. As ϕ increases, profile curvature increases. However, the overall geometry of profiles varies depending on the thickness of the soil layer(s) in which ϕ occurs; decreasing ϕ over larger zones (to retain constant surface flux) decreases profile curvature. Figure 25e demonstrates the effect of varying $F_{\text{CO}_2}^B$ with $\phi = 0$; the slope of the linear profile increases with increasing $F_{\text{CO}_2}^B$. Likewise, when there is production in the column (constant ϕ) (Figure 25f), overall profile slope increases with increasing basal flux.

Response times of all diffusion models (Figures 26 and 27) are within approximately 1.8 days, except in the case of low soil D_i^* (Figure 26a), which has a response time of approximately 11.6 days. This time decreases with increasing soil D_i^* and increases with increasing ϕ , thickness of the soil layer(s) in which ϕ occurs, and $F_{CO_2}^B$.

3.4.2 Advection-diffusion models

In advection-diffusion models where F_T^B of sufficient magnitude is maintained to produce total pressure gradients, advective gas flow occurs. Also, large F_{air}^B relative to $F_{CO_2}^B$ applied in models favors advective transport of CO_2 within the airflow upward through the soil column. Where CO_2 is dominantly carried by air in the column, $[CO_2]$ remains close to a value determined by the ratio of the basal mass fluxes of the two components. As this air/ CO_2 mixture rises through the CO_2 production zone, $[CO_2]$ increases as contribution of CO_2 to the bulk flow increases. As the air/ CO_2 flow approaches the surface, juxtaposition of elevated $[CO_2]$ in the production zone with atmospheric $[CO_2]$ results in steep near-surface $[CO_2]$ gradients. As these gradients steepen, the contribution of diffusive transport to the CO_2 flow increases.

From these relationships, we expect the following general trends in CO_2 transport processes throughout the steady state column: 1) Near the base of the soil column, due to large the contribution of air relative to CO_2 to the total gas flow, CO_2 is carried advectively upward by airflow. $[CO_2]$ and $[air]$ remain relatively constant as the surface is approached. 2) Within the production zone, $[CO_2]$ rises. This increased $[CO_2]$ towards the surface results in downward CO_2 diffusion. However, because the magnitude of the upward advective CO_2 flux is greater than that of the downward diffusive flux, the net

CO₂ flux is upward. 3) As the surface is approached, steep near-surface [CO₂] gradients favor upward diffusion of CO₂. This causes the relative contribution of advective to total CO₂ flow to decrease near the surface. Contrary to CO₂, we expect transport of air to be dominantly advective upward throughout the column when significant F_T^B is maintained. However, when no air is allowed to leave or enter the bottom of the column, any diffusive air transport due to CO₂ production within the column must be balanced by an advective air flux of equal magnitude, but in the opposite direction. Finally, the changes in total pressure in soil columns are very small compared to the average total pressure in columns [Lewicki *et al.*, 2001]; therefore, a change in P_i in a given direction in the soil column is approximately balanced by a change in P_j in the opposite direction.

3.4.2.1 Effect of soil diffusivity

Figures 28a and b show the effect of soil D_i^* on the geometry of [CO₂] and [air] profiles. With increase in D_i^* , concentration profiles show decrease in curvature. Maximum [CO₂] values in profiles decrease with increasing soil D_i^* (from approximately 0.6 to 0.3 vol.%). Figures 28c, e, and g demonstrate the influence of soil D_i^* on the relative magnitudes of advective and diffusive CO₂ fluxes through the soil column. At low D_i^* (Figure 28c), advective and diffusive surface CO₂ fluxes are approximately equal. From the bottom of the column to near the surface, CO₂ flux is dominantly advective in the upward direction. Increasing D_i^* increases the size of the diffusion-dominated upper section of the [CO₂] profile. At medium and high D_i^* , the surface CO₂ flux is dominantly diffusive and the magnitude of diffusive CO₂ fluxes through the zone of CO₂ production increase, relative to the case of low D_i^* .

3.4.2.2 Effect of soil permeability

Figures 29a and b demonstrate that the curvature of $[\text{CO}_2]$ and $[\text{air}]$ profiles increases with B_k . Varying B_k from low to medium and medium to high values results in large and small changes in profile geometry, respectively. Maximum $[\text{CO}_2]$ in profiles increases with soil B_k (from approximately 0.15 to 0.4 vol.%). Figures 28c, e, and g show that CO_2 transport across the soil/air interface remains dominantly diffusive. Advective transport dominates CO_2 flow through most of the soil column when B_k is medium or high. At low B_k (Figure 28c), simultaneous advective upward and diffusive downward flow is observed; however, near the surface, both mechanisms control gas flow to the surface. Although $[\text{CO}_2]$ gradients are largely reduced through the soil column at low B_k , the relative contribution of diffusive to total CO_2 flow increases. Relative magnitudes of advective and diffusive air fluxes through the soil column are largely insensitive to soil B_k (Figures 28d, f, and h).

3.4.2.3 Effect of basal gas flux

Figures 30a and b indicate that $[\text{CO}_2]$ and $[\text{air}]$ profile geometry is sensitive to $F_{\text{CO}_2}^B$; with increasing $F_{\text{CO}_2}^B$, profile curvature generally decreases. Maximum $[\text{CO}_2]$ values observed in profiles decrease with increasing $F_{\text{CO}_2}^B$ (from approximately 1.0 to 0.1 vol%). Figures 30c, e, and g show that $F_{\text{CO}_2}^B$ strongly affects transport of CO_2 across the soil/air interface; low and high $F_{\text{CO}_2}^B$ result in dominantly diffusive and advective surface fluxes, respectively. This change in transport persists into the upper soil column as increasing $F_{\text{CO}_2}^B$ creates sufficiently large total pressure gradients to drive advective flow at the expense of diffusive flow. Air flux through the soil column is

dominantly advective upward over the range of $F_{CO_2}^B$ values modeled (Figures 30d, f, and h). However, at low $F_{CO_2}^B$, relatively small diffusive fluxes of air are observed in the soil column that are balanced by advective air fluxes in the opposite direction.

The effect of changing chemical composition of F_T^B is shown in Figure 30. Increasing $[CO_2]$ in F_T^B decreases $[CO_2]$ and $[air]$ gradients in the lower part of the column while increasing them in the upper part. Maximum $[CO_2]$ values increase with $[CO_2]$ of F_T^B (from approximately 0.4 to 1.3 vol.%). Figures 31c, e, and g demonstrate that CO_2 fluxes across the soil/air interface and within the upper part of the column are relatively insensitive to change in $[CO_2]$ of F_T^B ; the surface CO_2 flux is dominantly diffusive over the range of values modeled. As the magnitude of this upward diffusive CO_2 transport increases with increasing $[CO_2]$ of the basal gas flux, so does the magnitude of the downward counterdiffusive flux of air into the soil.

3.4.2.4 Effect of soil CO_2 production

Figures 32 and 33 show the effect of varying ϕ_1 for $L_1=20$ cm and for $L_1=40$ cm, respectively. Figure 34 shows the effect of varying ϕ_1 for $L_1=40$ cm with ϕ_2 for $L_2=60$ cm. In general, the curvature of concentration profiles within the production zone increases with increasing ϕ . In addition, increasing ϕ causes a small decrease in the contribution of diffusive to total surface CO_2 fluxes (Figures 32, 33, and 34c, e, and g). However, $[CO_2]$ gradients created by the range of ϕ values modeled remain large enough to maintain dominantly diffusive surface CO_2 fluxes. Also, the relative contributions of advective and diffusive to total CO_2 fluxes through the soil column are not strongly influenced by changing ϕ at any given thickness of the soil layer(s) in which production

occurs. Distribution of CO_2 production over progressively larger areas while fixing the surface flux decreases profile curvature. Maximum $[\text{CO}_2]$ values observed in profiles increase with ϕ . Air fluxes through the soil column are dominantly advective upwards over the range of ϕ magnitudes and spatial distributions modeled (Figures 32, 33, and 34d, f, and h).

Figure 35 shows the effect of varying ϕ_1 for $L_1=40$ cm when $F_T^B = 0$. Figure 36 shows the effect of varying ϕ_1 for $L_1=40$ cm with ϕ_2 for $L_2=60$ cm when $F_T^B = 0$. $[\text{CO}_2]$ increases or remains constant with depth in all profiles. Also, profile curvature increases with increasing ϕ . For all cases, CO_2 flux is dominantly diffusive in the upward direction and decreases with depth to zero at the base of the soil layer(s) where CO_2 is produced (Figures 35 and 36 c, e, and g). Both profile geometry and fluxes are similar to those of purely diffusive CO_2 transport (Figures 25c and d). Finally, downward diffusion of air into the soil is balanced by upward advection of air to the soil surface. Our results indicate that at medium soil D_i^* and B_k values, modeled ϕ values are unable to produce total pressure gradients sufficient to drive significant advective CO_2 flow without F_T^B .

3.4.2.5 Effect of model parameters on response time

Figures 37-39 show average $\partial M_i / \partial t$ values for advection-diffusion model domains plotted as a function of model run time. These plots are used to estimate the length of time required for model conditions to approximate steady state. All advection-diffusion models equilibrate within 4.6 days. In advection-diffusion models with F_T^B , [air] profiles have lower response times than $[\text{CO}_2]$ profiles. Without F_T^B , both [air] and $[\text{CO}_2]$ profiles have comparable response times to diffusion model $[\text{CO}_2]$ profiles determined for

equivalent system parameters. Overall, the time required for [air] and [CO₂] profiles to reach steady state will depend on the relative contributions of advective and diffusive to total transport of these gases in soil columns. Because air transport is dominantly advective when F_T^B is present and CO₂ transport is some combination of advection and diffusion, [air] profiles generally reach steady state in significantly shorter periods of time than [CO₂] profiles.

Figure 37 shows that with increasing soil D_i^* , [CO₂] profile response time decreases to a small extent (from approximately 4 to 3 hours). B_k has little effect on [CO₂] profile response time when medium to high values are used (approximately 3 hours); however, at low soil B_k , this time increases to approximately 4.6 days (Figure 37). With increasing F_T^B (Figure 37), [CO₂] profile response time decreases significantly (from approximately 7 hours to 17 minutes), whereas increasing [CO₂] in F_T^B increases the response time (from approximately 3 to 14 hours). Figures 38 and 39 demonstrate that for any given soil layer thickness in which ϕ occurs, profile response time increases with increasing ϕ . Also, response time increases with thickness of the soil layer(s) in which ϕ occurs.

3.5 Discussion

3.5.1 Comparison of model results to field observations

We compare our results for steady state diffusion and advection-diffusion models to soil gas data collected by *Lewicki et al.* [in review] along the San Andreas and Calaveras faults, CA (Figure 22). However, to make close comparisons between model

results and field observations, it is necessary to know soil physical properties and boundary conditions at field sites. These parameters were largely unknown at the SAF and CF study sites and were suggested to vary in both space and time [Lewicki *et al.*, in review]. Therefore, we attempt to constrain system parameters to values which may be appropriate for study sites and discuss the conditions under which field observations are consistent with models. Where consistencies exist, we are able to make inferences about gas flow processes operating in soil columns at the SAF and CF sites.

Lewicki *et al.* [in review] estimated that maximum D_i^* values for SAF and CF site soils range from 0.03616 to 0.05369 cm^2s^{-1} , based on measured soil total porosities and temperatures. These values fall between medium and high soil D_i^* values used in models and provide an upper limit to soil diffusivities that we consider in this discussion. Soil texture at the SAF site was silty clay loam [Cook, 1978] which we expect to have a B_k value within the range of 10^{-12} to 10^{-8} cm^2 [e.g., Terzaghi and Peck, 1968]. However, extensive ground cracking was observed at study sites [Lewicki *et al.*, in review]. The effect of increasing soil fracture density has been shown to have a similar effect on gas flow to increasing soil B_k [e.g., Holford *et al.*, 1993]; therefore, we consider soil B_k to be largely unconstrained at study sites and assess the full the range of soil B_k values modeled. As described above, F_T^B and soil ϕ were modeled over ranges assumed to be reasonable for the SAF and CF study sites and so we consider these full ranges in comparisons of field and model results.

Measured Category I-type profiles (Figure 22) show an increase in $[\text{CO}_2]$ with soil depth and were interpreted by Lewicki *et al.* [in review] to reflect diffusion of soil CO_2 to the atmosphere. Estimated contribution of diffusive to total surface CO_2 fluxes suggest

that in some cases (SAF2, CF2, and CF4 profiles), diffusion may account entirely for surface fluxes above profiles, whereas in other cases (SAF1, SAF3, and CF3 profiles), a component of advective CO₂ transport across the soil/air interface may be important. The general shape of Category I profiles and the maximum [CO₂] values measured in these profiles compare well with both steady state diffusion-only models where ϕ was held constant within two soil layers without $F_{CO_2}^B$ (Figure 25d) and where $F_{CO_2}^B$ was maintained with constant ϕ in the upper soil layer (Figure 25f). These results suggest that for soil properties and boundary conditions considered reasonable for the SAF and CF study sites, steady state diffusive soil CO₂ flow may account entirely for some observed [CO₂] profiles and corresponding surface CO₂ fluxes. However, for those Category I profiles where a component of advective gas transport is suggested to be important (i.e., SAF1, SAF3, and CF3), alternative gas flow models must be invoked. Most advection-diffusion models where advective CO₂ flow occurs within soil columns (i.e., where F_T^B is maintained) are not consistent with the overall geometry of SAF1, SAF3, and CF3 profiles (Figures 22 and 28-34). One model that might be invoked to explain these profiles is the presence of a basal gas flux with relatively high [CO₂] (e.g., 1-2 vol.%) to maintain relatively high [CO₂] at the base of the soil column, but also with greater total magnitude than we modeled, to generate total pressure gradients sufficient to drive near-surface advective CO₂ flow.

Category II profiles display an increase, then decrease in [CO₂] with soil depth. Estimated contribution of diffusive to total surface CO₂ fluxes suggest that in some profiles (SAF5, SAF7, and CF5), advective CO₂ transport across the soil/air interface is important, whereas in others (SAF4 and SAF6), diffusive transport may account entirely

for surface CO₂ fluxes. Our steady state diffusion-only models cannot account for the overall shape of Category II profiles. However, Category II-type profiles have been observed in soils after periods of heavy rainfall and/or during the growing season [e.g., *DeJong and Schappert*, 1972; *Osozawa and Hasegawa*, 1995] and interpreted to represent transient diffusive CO₂ flow. In this case, decreased air-filled pore space available for CO₂ flow and/or increased soil ϕ may cause CO₂ accumulation in the shallow soil, generating a Category II-type profile. While this interpretation may explain some data sets well, evidence of advective surface CO₂ fluxes above many SAF and CF profiles [*Lewicki et al.*, in review] indicate that an alternative gas transport model is required for these sites. Also, the shapes of SAF and CF profiles showed no consistent relationship with rainfall events, soil temperature, observed vegetation density and type, and measurement date [*Lewicki et al.*, in review].

Lewicki et al. [in review] inferred relatively low [CO₂] at depth in these profiles to be related to wind-driven atmospheric airflow through fractured soils. In this scenario, atmospheric air would flow from the soil surface through soil fracture networks that intersect the base of profiles, creating a F_T^B . The shape of most measured Category II profiles (as well as the maximum [CO₂] values in these profiles) are consistent with our advection-diffusion model results where soils have moderate to high B_k values and F_T^B with relatively low [CO₂] (0.04-0.10 vol.%) is maintained. The magnitude of F_T^B was demonstrated to strongly influence the magnitude of the advective surface CO₂ flux. Therefore, in Category II profiles where diffusion accounts entirely for surface fluxes above profiles, F_T^B ranging from the low to medium values used in models are reasonable. In these situations, advective transport of CO₂ upward through most of the soil

column is important, but diffusive transport dominates across the soil/air interface. If higher F_T^B is maintained, advective CO₂ transport across the soil/air interface becomes important, consistent with SAF5, SAF7, and CF5 profiles. In all F_T^B cases, air transport is dominantly advective upward through the entire soil column. Maximum [CO₂] values measured in and at the base of the CF5 profile are higher than those observed in other Category II profiles and most advection-diffusion models with F_T^B . Also, the surface CO₂ flux above CF5 is approximately an order of magnitude greater than those measured above other Category II profiles. One explanation for these observations, as well as the large advective component of surface CO₂ flux above this profile, may be the combined effects of higher soil ϕ in the CF5 column and higher F_T^B .

Category III profiles show a more complicated pattern of repeated increase and decrease in [CO₂] with soil depth. As observed for Category I and II profiles, maximum estimated per-cent diffusive of total surface CO₂ fluxes above these profiles suggest that in some profiles advective CO₂ transport across the soil/air interface is important, whereas in others, this flux is entirely diffusive. The general shape of these profiles is not consistent with our steady state diffusion model results. *Lewicki et al.* [in review] suggested that lateral airflow through fractures at depth may account for relatively low observed [CO₂] values in these soil columns. Also, stable carbon isotopic compositions of soil CO₂ were determined in the SAF12 profile (Figure 22) and suggest addition of atmospheric air (perhaps wind-driven) at -60 cm depth where [CO₂] is relatively low [*Lewicki et al.*, in review]. Although a multi-dimensional model is required to fully examine lateral airflow in soil columns, our models approximate this airflow by considering a fracture that ends at the base of our Category II-type modeled profiles and originates

at the soil surface. We may therefore treat the upper portion of Category III profiles, where $[\text{CO}_2]$ increases, then decreases with soil depth, as Category II profiles. As a result, the same basic features of gas flow we observe in our Category II-type models may apply to the upper sections of measured Category III profiles.

Lewicki et al. [in review]’s interpretations of measured $[\text{CO}_2]$ profiles required that steady state gas flow was approximated in soil columns. To assess the temporal variation of $[\text{CO}_2]$ profiles, they repeated measurements of two profiles (a Category I profile where diffusion accounted entirely for associated surface CO_2 fluxes and a Category III profile where advective CO_2 flow across the soil/air interface was important) over a one month period. *Lewicki et al.* [in review] found that the general shape of both profiles was remarkably stable over the measurement period. Also, repeated measurements of the Category I and III profiles were spatially well correlated on temporal scales up to one month and approximately 15 days, respectively. These observations suggested steady state conditions in those soil columns. Our results show that the response times of all diffusion models are within approximately 11.6 days; however, disregarding the case of low soil D_i^* , model response times are within 1.8 days. Response times of all advection-diffusion models where F_T^B is maintained are within approximately 4.6 days. We therefore conclude that *Lewicki et al.* [in review]’s assumption of steady state conditions in soil columns was reasonable.

3.5.2 Implications for fault zone soil gas studies

Our results show that F_T^B of small magnitude (relative to surface wind speeds) can produce total pressure gradients sufficient to drive advective gas flow through soil

columns. Also, relative to total atmospheric pressure, these pressure gradients in the soil are themselves small. These results agree with previous field, laboratory, and numerical studies [e.g., *Thorstenson and Pollock*, 1989; *Massmann and Farrier*, 1992] indicating that very small total pressure gradients can produce advective gas fluxes in soils that overwhelm diffusive fluxes. It is therefore important for soil gas studies to consider the possible effects of wind-driven airflow through faulted/fractured soils (as well as other shallow processes) on gas transport and resulting soil gas concentration profiles and surface fluxes. The effects of these shallow processes on soil gas flow must be understood in order to meaningfully interpret fault zone soil gas flux and concentration measurements.

CO₂ fluxes measured by the accumulation chamber method must consider the influence of advective gas (air and CO₂) transport across the soil/air interface on the flux measurement [*Evans et al.*, 2001]. *Evans et al.* [2001] demonstrated in laboratory experiments that when an accumulation chamber placed on the soil surface encounters upward advective gas flow, the chamber can disturb the pressure gradient, causing the gas flow to be diverted around the chamber. The authors proposed that this gas flow diversion may be responsible for systematic underestimation of surface CO₂ fluxes measured by the accumulation chamber method. While *Evans et al.* [2001] focussed their investigation on gas transport in high CO₂ emission volcanic-metamorphic environments, the results of our study indicate that similar transport processes may affect CO₂ flux measurements in areas where CO₂ derives mainly from soil respiration.

Our model results show that gas transport processes through soils are sensitive to both soil physical properties and boundary conditions over the range of values we

modeled. In particular, the magnitude and chemical composition of F_T^B strongly influence both the dominant transport mechanisms through soil and the geometry of gas concentration profiles. Also, gas transport and profile geometry were shown to be sensitive to soil D_i^* and B_k . Relative to varying other model parameters, the contributions of advective and diffusive CO_2 flow through soil columns seemed to be less sensitive to varying soil ϕ ; however, for any given ϕ , the thickness of the soil layer(s) in which ϕ occurs influences these relative contributions. The wide range of gas flow behavior observed over parameter values that may vary temporally and spatially in natural systems [Lewicki *et al.*, in review] indicates that field data must be collected to constrain model parameters contemporaneously with soil gas measurements in two to three dimensions. We recommend $[\text{CO}_2]$ and total gas pressure measurements within three-dimensional arrays in the soil, along with corresponding surface CO_2 fluxes above each $[\text{CO}_2]$ /total pressure profile. In addition, multi-dimensional measurements should be made of soil water content, total porosity, and texture to constrain D_i^* . Soil crack densities and air permeabilities as a function these densities should also be measured. Furthermore, the influence of surface wind speed and direction on soil total pressure gradients should be established to better understand the relationship between wind and advective gas flow through fractured soils. With these constrained parameters, meaningful tests of multi-dimensional gas flow models applied to natural systems may be made.

3.6 Conclusions

We draw the following conclusions based on our soil gas transport modeling results:

1) The shape of $[\text{CO}_2]$ profiles modeled for one-dimensional diffusion of CO_2 in air is sensitive to both properties of the soil and boundary conditions. An increase in profile curvature is caused by increasing soil CO_2 production rate (ϕ) and decreasing the soil diffusion coefficient (D_i^*). Increasing the basal flux of CO_2 ($F_{\text{CO}_2}^B$) causes an overall increase in profile slope.

2) Models of combined advective and diffusive transport of CO_2 and air indicate that contribution of advective versus diffusive CO_2 flow through the soil column and the geometry of gas concentration profiles are highly sensitive to the magnitude and chemical composition of the total basal gas flux (F_T^B). Increasing F_T^B causes increasing upward advective CO_2 flow through the entire soil column. Increasing $[\text{CO}_2]$ of F_T^B (and corresponding decreasing F_{air}^B) causes increasing diffusive CO_2 flow through the soil column. At all F_T^B magnitudes, transport of air is dominantly advective upward through the soil. Without F_T^B , modeled soil ϕ values are insufficient to generate total pressure gradients to drive significant advective gas flow; CO_2 fluxes are dominantly diffusive upwards and net air flux is zero.

3) Advective and diffusive soil gas transport processes and shape of concentration profiles are sensitive to soil D_i^* . With increasing D_i^* , the contribution of diffusive to total CO_2 flow through the soil column increases and curvature of concentration profiles decreases.

4) Soil gas transport and concentration profile shape are sensitive to soil permeability (B_k). Increase in soil B_k from low to medium values causes the contribution of advective to total CO_2 flow through most of the soil column to increase; however, CO_2 transport across the soil/air interface is largely insensitive to varying B_k . Varying B_k

from low to medium values also causes an increase in curvature of concentration profiles. Gas transport processes through the soil column and concentration profile shape show little change from medium to high B_k values.

5) Compared to other parameters, the relative contributions of advective and diffusive to total CO₂ fluxes through the soil column seem to be less sensitive to ϕ , in areas of the soil column in which production occurs. However, the geometry of concentration profiles is sensitive to ϕ ; increasing ϕ causes curvature of profiles to increase.

6) Model response time is sensitive to the relative contributions of advective and diffusive to total gas flow through soil columns; therefore, varying model parameters that influence these contributions affects response time. The response time of models where diffusive gas transport dominates through the soil column is generally higher than models where advective transport is important. Similarly, because air transport through most of the soil columns where F_T^B is maintained is mainly advective and CO₂ transport is some combination of advection and diffusion, most [air] profiles have significantly shorter response times than [CO₂] profiles.

7) [CO₂] profiles modeled for one-dimensional diffusion of CO₂ in air using soil properties and boundary conditions considered reasonable for the SAF and CF study sites compare well with the geometry of Category I-type [CO₂] profiles measured by *Lewicki et al.* [in review] at these sites. However, while cases where diffusion accounts entirely for measured surface CO₂ fluxes above observed Category I profiles may be explained well by diffusive soil CO₂ transport models, alternative gas transport models must be invoked for measured profiles where a component of advective surface CO₂ transport is indicated.

8) One-dimensional models of advective-diffusive gas flow in which soils have moderate to high B_k values and F_T^B with relatively low $[\text{CO}_2]$ is maintained compare well with the geometry of Category II-type $[\text{CO}_2]$ profiles measured by *Lewicki et al.* [in review] and the estimated contribution of advective to total surface CO_2 fluxes above these profiles. While other gas transport models may also account for these field observations, consistency between field observations and our model results suggests that wind-driven airflow through fractured soils along the San Andreas and Calaveras faults may cause significant advective CO_2 flow at these study sites, as proposed by *Lewicki et al.* [in review].

9) Our model results suggest that relatively small magnitude F_T^B can produce total pressure gradients sufficient to drive advective gas flow through soil columns. Therefore, interpretations of soil gas data collected in faulted/fractured terrain should consider the effects of wind-driven airflow through soils on gas transport and resulting soil gas concentration profiles and surface fluxes. Also, the effects of this advective gas flow on soil CO_2 flux measurements by the accumulation chamber method should be taken into account.

10) To extend our one-dimensional advection-diffusion models to the study of gas flow in complex heterogeneous soils typical of faulted/fractured areas, we recommend that laboratory experiments first be conducted to determine if our models adequately approximate real gas flow in simple systems where the system parameters are well known. If so, multi-dimensional models should be developed, complemented by multi-dimensional field measurements of soil physical properties, soil gas concentrations and fluxes, and meteorological parameters.

3.7 Appendix I

Under steady-state conditions in a soil column with thickness of L , Equation 3.5 is solved analytically to yield C_{CO_2} as a function of soil depth z . We consider the case where CO_2 is produced in the soil at constant rates ϕ_1 and ϕ_2 through soil layers with lengths L_1 and L_2 , respectively, where

$$L = L_1 + L_2 \quad (3.17)$$

and the following boundary conditions exist

$$atz = 0, \quad C_{CO_2} = C_{CO_2}^o \quad (3.18)$$

$$atz = -L, \quad Q_{CO_2}^D = F_{CO_2}^B \quad (3.19)$$

where $C_{CO_2}^o$ is the atmospheric molar density of CO_2 and $F_{CO_2}^B$ is a constant molar flux of CO_2 applied to the base of the soil column.

We initially solve for $Q_{CO_2}^D$ as a function of z in the upper soil layer from $-L$ to $-L_1$, and then in the lower soil layer from $-L_1$ to the soil surface. For the upper soil layer, the mass conservation equation (Equation 3.3) reduces to

$$\left[\frac{\partial Q_{CO_2}^D}{\partial z} \right]_2 = \phi_2 \quad (3.20)$$

Integration of Equation 3.20 gives

$$Q_{CO2,2}^D(z) = \phi_2 z + c_1 \quad (3.21)$$

where c_1 is the constant of integration. We implement the lower boundary condition (Equation 3.19) to give

$$Q_{CO2,2}^D(-L_1 - L_2) = \phi_2(-L_1 - L_2) + c_1 = F_{CO2}^B \quad (3.22)$$

We then rearrange Equation 3.22 to solve for c_1 and substitute into Equation 3.22 to yield $Q_{CO2,2}^D$ as a function of soil depth from $-L$ to $-L_1$:

$$Q_{CO2,2}^D(z) = \phi_2 z + \phi_2(L_1 + L_2) + F_{CO2}^B \quad (3.23)$$

For the upper soil layer, the mass conservation equation (Equation 3.3) is

$$\left[\frac{\partial Q_{CO2}^D}{\partial z} \right]_1 = \phi_1 \quad (3.24)$$

To solve for $Q_{CO2,1}^D(z)$ in the upper soil layer, we first integrate Equation 3.24:

$$Q_{CO2,1}^D(z) = \phi_1 z + c_2 \quad (3.25)$$

where c_2 is the constant of integration. Q_{CO2}^D leaving the top of the bottom soil layer must enter the bottom of the top soil layer, at $z = -L_1$. To merge the top and bottom soil layers, we first solve for c_2 at $z = -L_1$ and require Q_{CO2}^D at $z = -L_1$ in the upper layer to equal Q_{CO2}^D at $z = -L_1$ in the bottom layer to yield

$$c_2 = \phi_1 L_1 + Q_{CO2,1}^D(-L_1) = \phi_1 L_1 + Q_{CO2,2}^D(-L_1) \quad (3.26)$$

We then find $Q_{CO2,2}^D$ (Equation 3.23) at $z = -L_1$:

$$Q_{CO2,2}^D(-L_1) = -\phi_2 L_1 + \phi_2(L_1 + L_2) + F_{CO2}^B \quad (3.27)$$

We solve for c_2 as a function of Q_{CO2}^D at the top of the bottom soil layer by substituting Equation 3.27 into 3.26:

$$c_2 = \phi_1 L_1 + \phi_2 L_2 + F_{CO2}^B \quad (3.28)$$

and then substituting c_2 (Equation 3.28) into 3.25 to give

$$Q_{CO2,1}^D(z) = \phi_1(z + L_1) + \phi_2 L_2 + F_{CO2}^B \quad (3.29)$$

Next, we solve for $C_{CO2}(z)$ in the upper soil layer. Substitution of Equation 3.29 into Fick's law (Equation 3.1) yields

$$\left[\frac{\partial C_{CO2}}{\partial z} \right]_1 = -\frac{1}{D_i^*} \left[\phi_1 z + \phi_1 L_1 + \phi_2 L_2 + F_{CO2}^B \right] \quad (3.30)$$

Integration of Equation 3.30 gives

$$C_{CO2,1}(z) = -\frac{1}{D_i^*} \left[\frac{\phi_1}{2} z^2 + \phi_1 L_1 z + \phi_2 L_2 z + F_{CO2}^B z \right] + c_3 \quad (3.31)$$

where c_3 is a constant of integration. Implementation of the upper boundary condition (Equation 3.18) by setting $c_3 = C_{CO_2}^o$ provides C_{CO_2} as a function of soil depth from $-L_1$ to the soil surface:

$$C_{CO_2,1}(z) = -\frac{z}{D_i^*} \left[\frac{\phi_1}{2} z + \phi_1 L_1 + \phi_2 L_2 + F_{CO_2}^B \right] + C_{CO_2}^o \quad (3.32)$$

We then solve for $C_{CO_2}(z)$ in the lower soil layer. We substitute Equation 3.23 into Fick's law (Equation 3.1) to give

$$\left[\frac{\partial C_{CO_2}}{\partial z} \right]_2 = -\frac{1}{D_i^*} \left[\phi_2 z + \phi_2 (L_1 + L_2) + F_{CO_2}^B \right] \quad (3.33)$$

and integrate Equation 3.33 to find

$$C_{CO_2,2}(z) = -\frac{z}{D_i^*} \left[\frac{\phi_2}{2} z + \phi_2 (L_1 + L_2) + F_{CO_2}^B \right] + c_4 \quad (3.34)$$

where c_4 is the constant of integration. We solve for c_4 by requiring $C_{CO_2,2}$ at the top of the bottom soil layer to equal $C_{CO_2,1}$ at the bottom of the top layer (i.e., Equation 3.34 = Equation 3.32 at $z = -L_1$) and substitute into Equation 3.34:

$$C_{CO_2,2}(z) = -\frac{z}{D_i^*} \left[\frac{\phi_2}{2} z + \phi_2 (L_1 + L_2) + F_{CO_2}^B \right] + \frac{L_1}{D_i^*} \left[\frac{\phi_1 L_1}{2} - \frac{\phi_2 L_1}{2} \right] + C_{CO_2}^o \quad (3.35)$$

Equations 3.35 and 3.32 are used to calculate soil $[CO_2]$ profiles from $-L$ to $-L_1$ and from $-L_1$ to the soil surface, respectively.

Table 5. Notation of model parameters.

Notation	Parameter	Dimensions
B_k	Soil intrinsic permeability	L^2
C_{air}	Molar density of air	$\text{mol } L^{-3}$
C_{CO_2}	Molar density of CO_2	$\text{mol } L^{-3}$
C_i	Molar density of component i	$\text{mol } L^{-3}$
C_{air}^o	Atmospheric molar density of air	$\text{mol } L^{-3}$
$C_{CO_2}^o$	Atmospheric molar density of CO_2	$\text{mol } L^{-3}$
D_i^*	Diffusion coefficient of component i in soil	$L^2 t^{-1}$
D_{air-CO_2}	Binary diffusion coefficient of air in CO_2	$L^2 t^{-1}$
D_{CO_2-air}	Binary diffusion coefficient of CO_2 in air	$L^2 t^{-1}$
D_{i-j}	Binary diffusion coefficient of component i in j	$L^2 t^{-1}$
$F_{CO_2}^B$	Basal flux CO_2	$\text{mol } L^{-2} t^{-1}$
F_{air}^B	Basal flux air	$\text{mol } L^{-2} t^{-1}$
F_T^B	Total basal gas flux	$\text{mol } L^{-2} t^{-1}$
L	Thickness of soil column	L
L_1	Thickness of upper layer of soil column	L
L_2	Thickness of lower layer of soil column	L
M_i	Mass of component i	M
M_{air}	Mass of air	M
M_{CO_2}	Mass of CO_2	M
n_a	Soil air-filled porosity	
P	Total pressure	$M L^{-1} t^{-2}$
P_{air}	Partial pressure of air	$M L^{-1} t^{-2}$
P_{CO_2}	Partial pressure of CO_2	$M L^{-1} t^{-2}$
P_i	Partial pressure of component i	$M L^{-1} t^{-2}$
Q_i^D	Diffusive flux of component i	$\text{mol } L^{-2} t^{-1}$
Q_i^T	Total flux of component i	$\text{mol } L^{-2} t^{-1}$
R	Ideal gas constant	$M L^2 t^{-2} T^{-1} \text{mol}^{-1}$
t	Time	t
T	Absolute temperature	T
z	Soil depth	L
ϕ	Soil CO_2 production rate	$\text{mol } L^{-3}$
ϕ_1	CO_2 production rate in upper layer of soil column	$\text{mol } L^{-3}$
ϕ_2	CO_2 production rate in lower layer of soil column	$\text{mol } L^{-3}$
μ	Gas viscosity	$M L^{-1} t^{-1}$
τ	Soil tortuosity	

Table 6. Gas parameters used in models.

Parameter	Units	CO ₂	air
Molecular weight	g mol ⁻¹	44.0	28.9
Gas viscosity μ	g cm ⁻¹ s ⁻¹	0.000147	0.000181
Atmospheric partial pressure	g cm ⁻¹ s ⁻²	405	1,012,845
Diffusion coefficient in air D_{CO_2-air}	cm ² s ⁻¹	0.15323	–
Diffusion coefficient in CO ₂ D_{air-CO_2}	cm ² s ⁻¹	–	0.15323

Table 7. Range of parameter values used in models. Ranges of basal flux air and CO₂ values correspond to [CO₂] of the basal air-CO₂ gas mixture equal to 0.04 vol.%.

Parameter	Units	Low	Medium	High
Soil intrinsic permeability B_k	cm ²	1E-13	1E-08	1E-04
Soil porosity x tortuosity $n_a\tau$		0.02	0.26	0.50
Basal flux CO ₂ $F_{CO_2}^B$	g cm ⁻² s ⁻¹	2.31E-10	2.31E-09	2.31E-08
Basal flux air F_{air}^B	g cm ⁻² s ⁻¹	3.80E-07	3.80E-06	3.80E-05
Basal gas flux [CO ₂]	vol. %	0.04	0.10	1.0
1.) CO ₂ production rate ϕ_1 ($L_1=20$ cm)	g cm ⁻³ s ⁻¹	7.52E-10	2.08E-09	3.18E-09
2.) CO ₂ production rate ϕ_1 ($L_1=40$ cm)	g cm ⁻³ s ⁻¹	3.76E-10	1.04E-09	1.59E-09
3.) CO ₂ production rate ϕ_1 ($L_1=40$ cm)	g cm ⁻³ s ⁻¹	2.51E-10	6.94E-10	1.06E-09
ϕ_2 ($L_2=60$ cm)	g cm ⁻³ s ⁻¹	8.36E-11	2.31E-10	3.54E-10

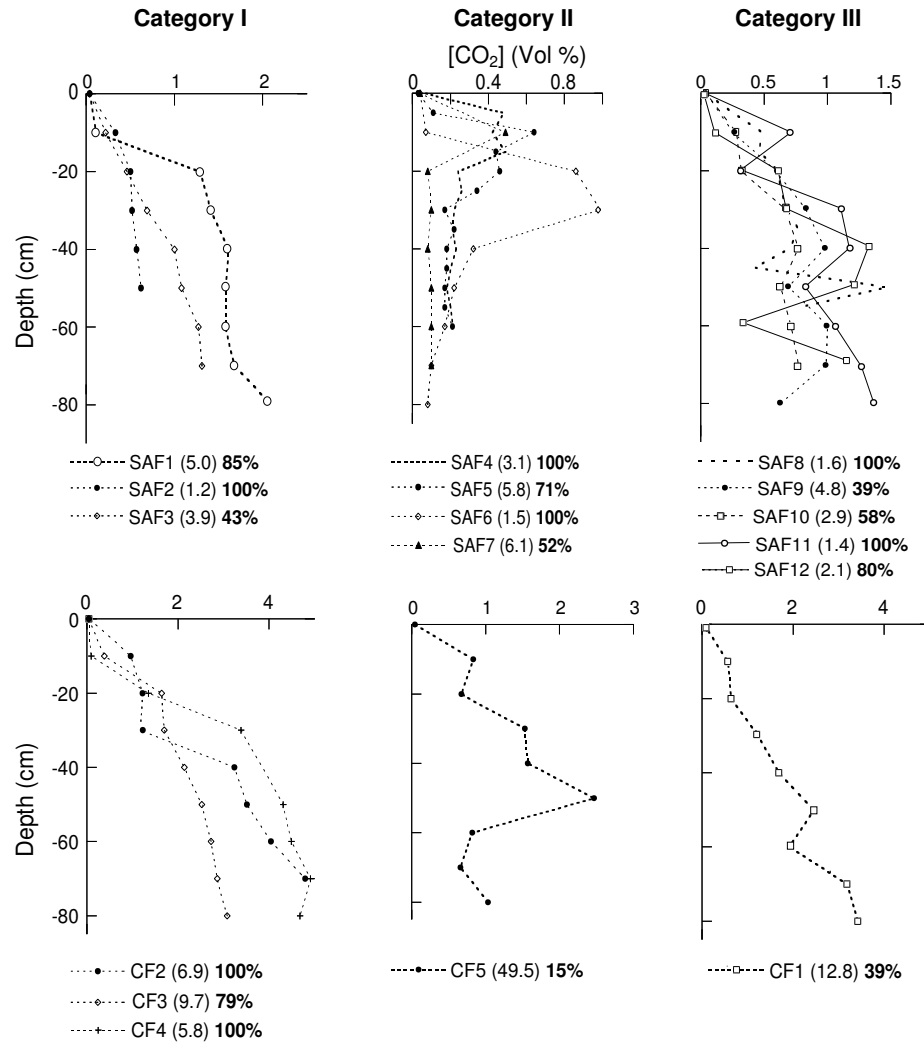


Fig. 22. Soil [CO₂] profiles measured within SAF and CF grids (modified from *Lewicki et al.* [in review]). Also shown are corresponding surface CO₂ fluxes in parentheses (in $10^{-8} \text{ g cm}^{-2} \text{ s}^{-1}$) and estimated per-cent diffusive of total surface CO₂ fluxes in bold (see *Lewicki et al.* [in review]) for description of this calculation using Fick's law). Profiles were categorized based on general shape: Category I profiles show [CO₂] increase with depth; Category II profiles exhibit [CO₂] increase followed by decrease with depth; Category III profiles exhibit a saw-tooth pattern with repeated increase and decrease in [CO₂] with depth. *Lewicki et al.* [in review] interpreted Category I profiles to reflect diffusion of CO₂ to the atmosphere, whereas the observed decrease(s) in [CO₂] with depth in Category II and II profiles were attributed to wind-driven atmospheric airflow through fractured soil. A consistent relationship was not observed between profile category and distance from the fault trace, measurement date, soil temperature, rainfall event, or vegetation density and type.

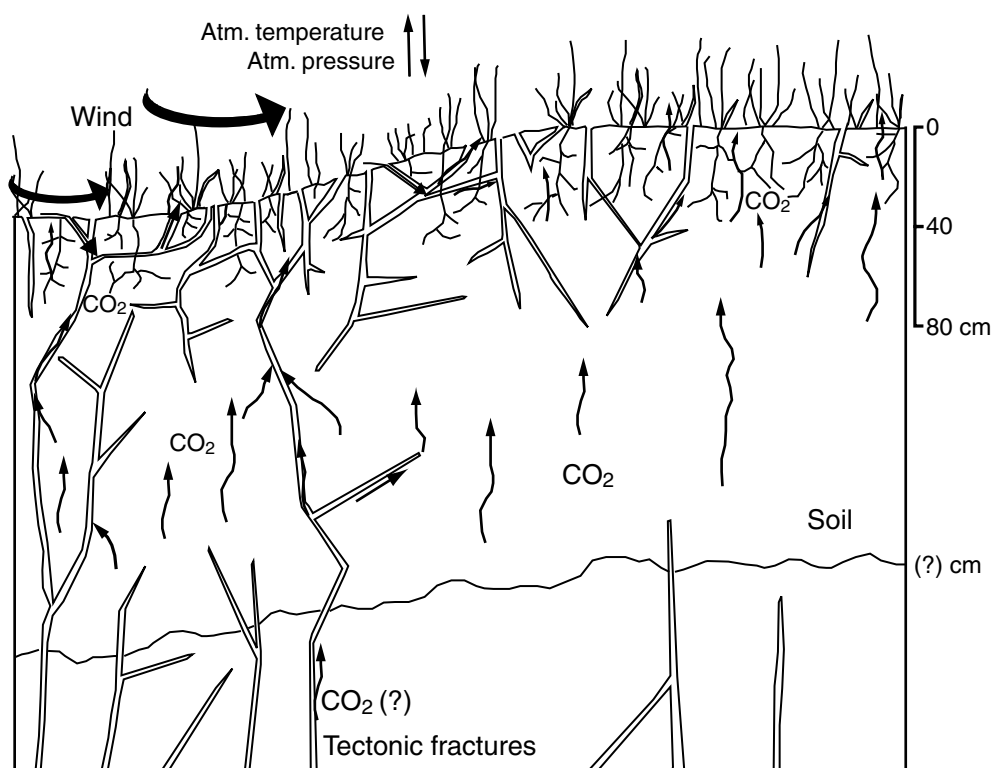


Fig. 23. Schematic of gas flow in fractured terrain proposed by *Lewicki et al.* [in review] showing movement of soil CO₂ to the atmosphere. Sources of CO₂ may include root respiration, heterotrophic bacteria, and seasonal groundwater degassing. Highly permeable fractures (tectonic and non-tectonic) may focus and enhance CO₂ flow. Temporal fluctuations in meteorological parameters may modulate transport of soil CO₂ to the atmosphere by disturbing soil [CO₂] and total pressure gradients. In particular, *Lewicki et al.* [in review] suggested that wind-driven atmospheric air flow through fractures acts as a carrier gas for soil CO₂, resulting in enhanced surface CO₂ flux. Soil depth is unknown at SAF and CF study sites. Fracture depth and density are not to scale.

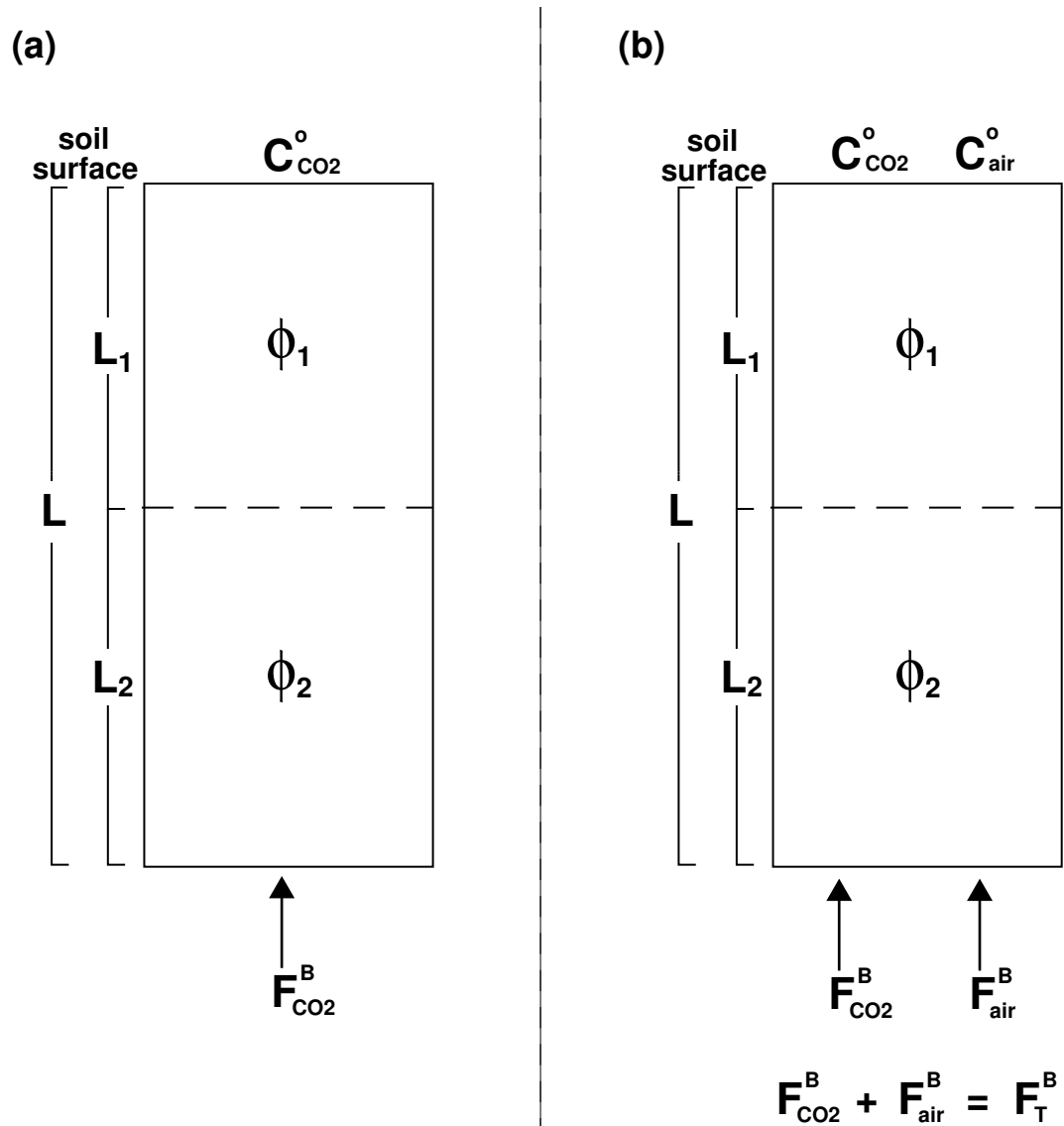


Fig. 24. (a) Boundary conditions for model of one-dimensional diffusive CO₂ flow through a soil column where CO₂ is produced in the soil at constant rates ϕ_1 and ϕ_2 through zones with thicknesses L_1 and L_2 , respectively. $C_{CO_2}^o$ is constant surface [CO₂] and $F_{CO_2}^B$ is constant molar flux of CO₂ at the base of the soil column. (b) Boundary conditions for model of one-dimensional combined advective and diffusive air and CO₂ flow through a soil column where CO₂ is produced in the soil at constant rates ϕ_1 and ϕ_2 through zones with thicknesses L_1 and L_2 , respectively. C_{air}^o and $C_{CO_2}^o$ are constant surface [CO₂] and [air], respectively, and F_{air}^B and $F_{CO_2}^B$ are constant molar fluxes of air and CO₂ at the base of the soil column, respectively.

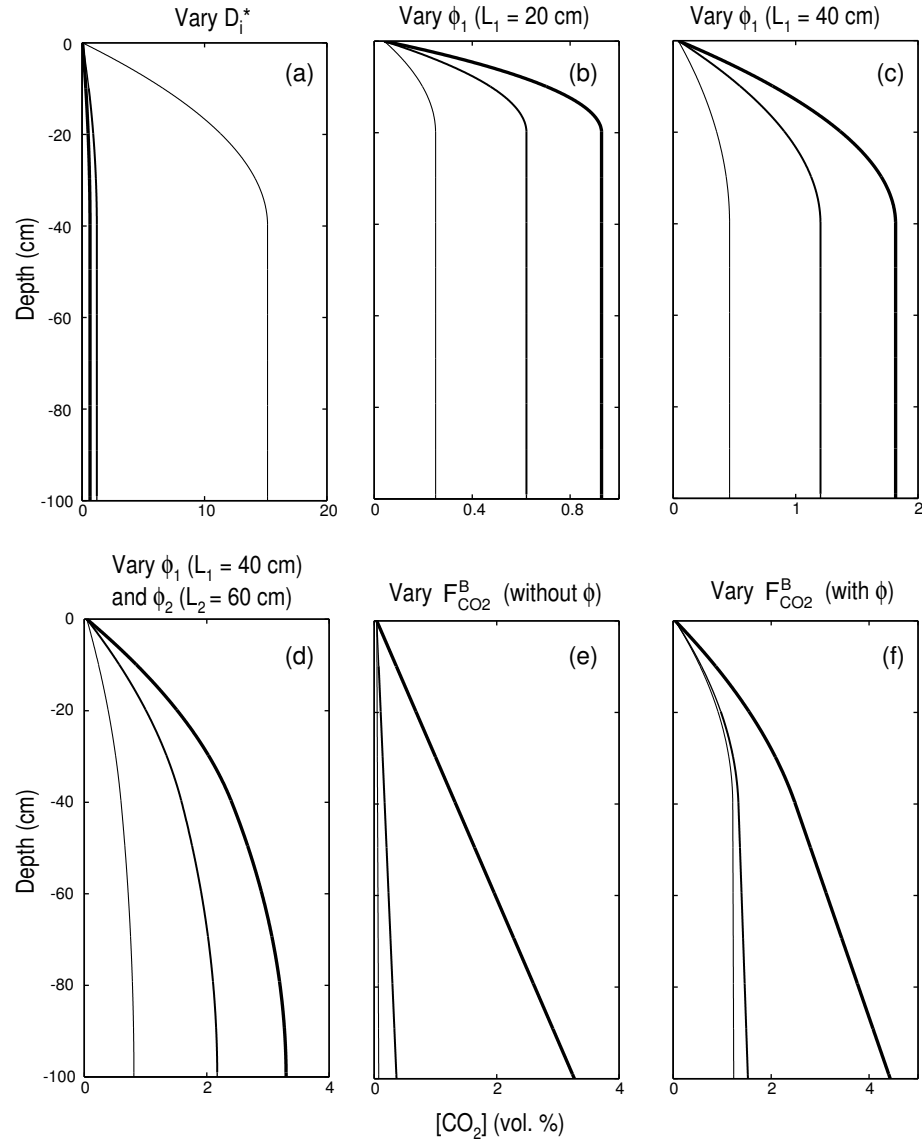


Fig. 25. Effect of varying diffusion model parameters on soil $[CO_2]$ profile shape. Light, medium, and heavy weighted lines represent low, medium and high model parameter values, respectively (Table 7).

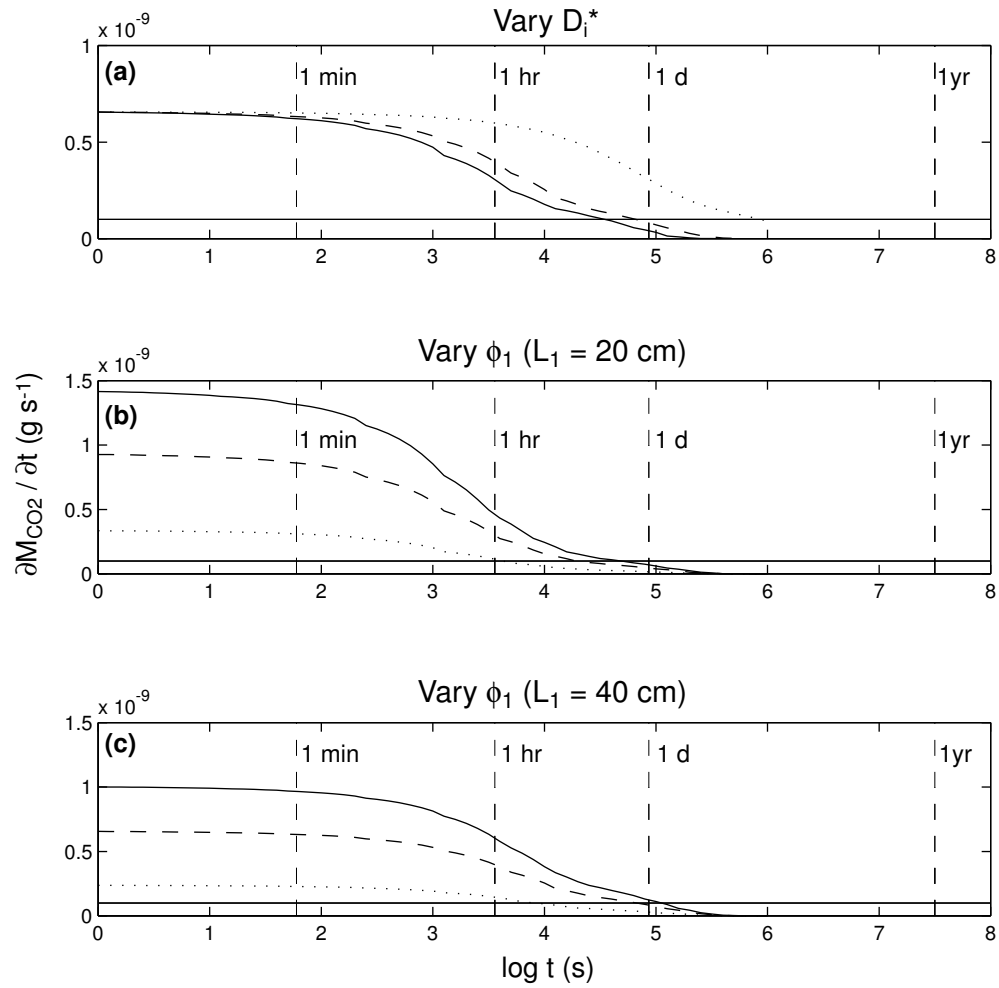


Fig. 26. Average rate of change of CO₂ mass in diffusion model domains ($\partial M_{CO_2}/\partial t$) as a function of model run time t for cases where (a) soil D_i^* , (b) ϕ_1 for $L_1=20 \text{ cm}$, and (c) ϕ_1 for $L_1=40 \text{ cm}$ were varied. Dotted, dashed and solid lines represent low, medium, and high parameter values. Response times for soil [CO₂] profiles are shown when $\partial M_{CO_2}/\partial t = 10^{-10} \text{ g s}^{-1}$ (solid horizontal lines). See text for complete model descriptions.

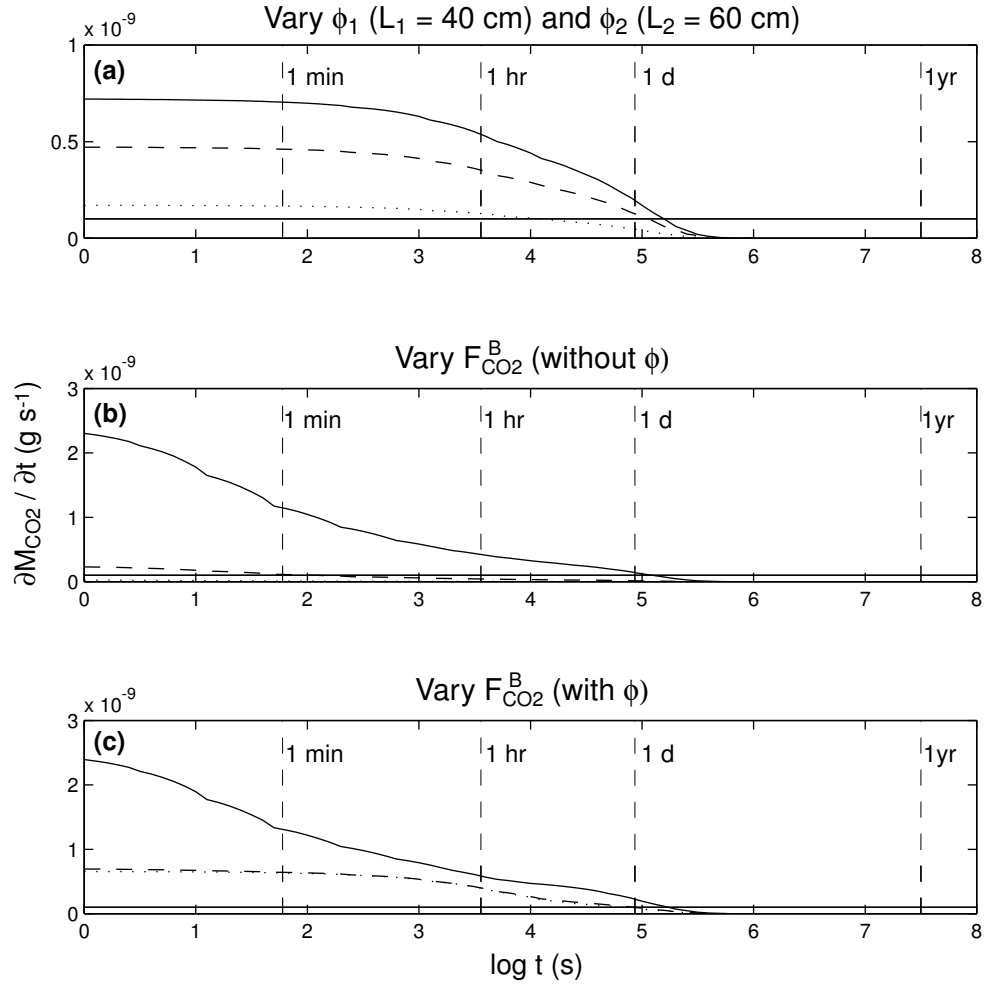


Fig. 27. Average rate of change of CO₂ mass in diffusion model domains ($\partial M_{CO_2}/\partial t$) as a function of model run time t for cases where (a) ϕ_1 for $L_1=40$ cm and ϕ_2 for $L_2=60$ cm, (b) $F_{CO_2}^B$ without soil ϕ , and (c) $F_{CO_2}^B$ with soil ϕ ($L_1=40$ cm) were varied. Response times for soil [CO₂] profiles are shown when $\partial M_{CO_2}/\partial t = 10^{-10} g s^{-1}$ (solid horizontal lines). See text for complete model descriptions.

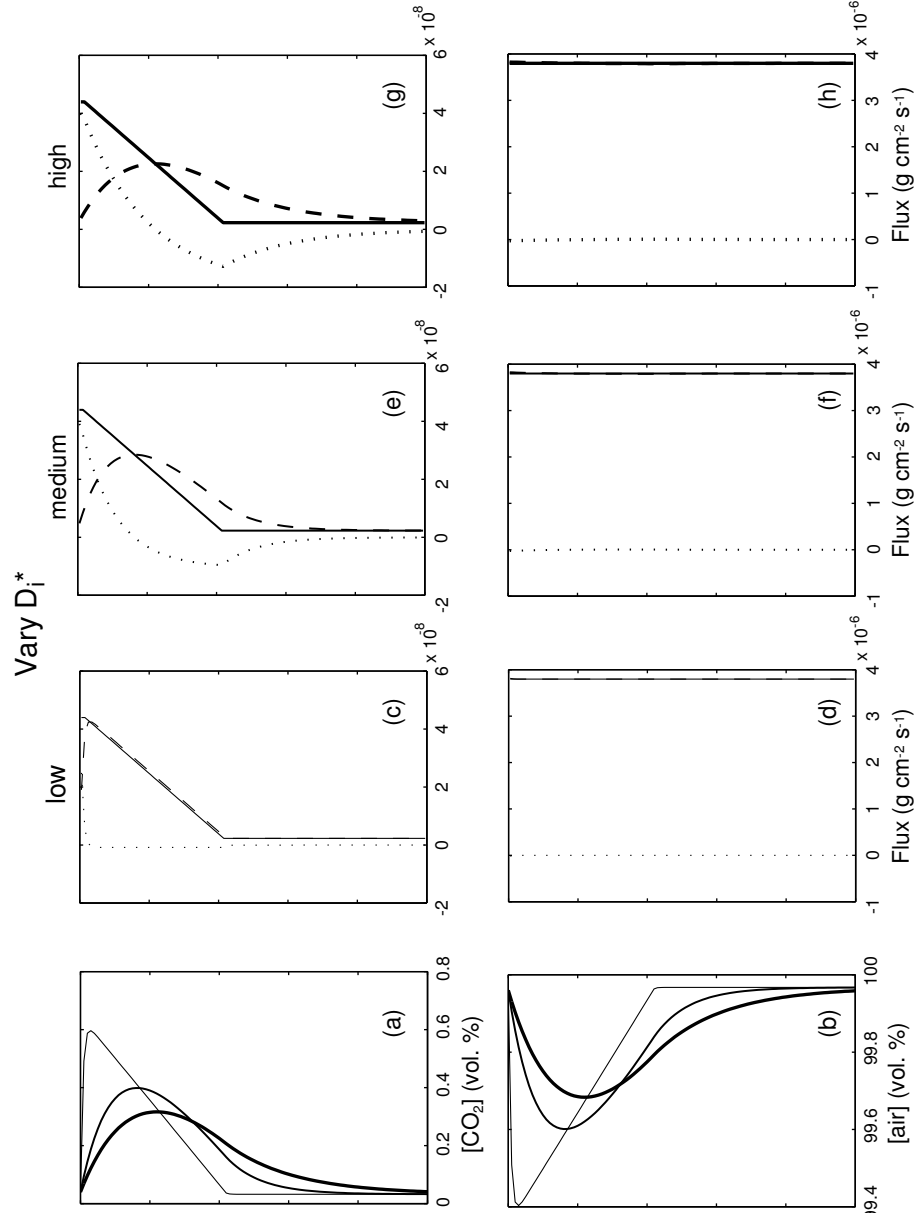


Fig. 28. Effect of varying soil diffusivity, D_i^* (Equation 3.2), on soil (a) $[\text{CO}_2]$ and (b) $[\text{air}]$ profile shape. Light, medium, and heavy weighted lines represent low, medium and high D_i^* values. Also shown is effect of varying D_i^* on magnitude of total (solid lines), advective (dashed lines), and diffusive (dotted lines) fluxes through soil column for (c, d) low, (e, f) medium, and (g, h) high D_i^* values, respectively (top and bottom rows are CO_2 and air fluxes, respectively). Positive and negative flux magnitudes represent upward and downward fluxes, respectively.

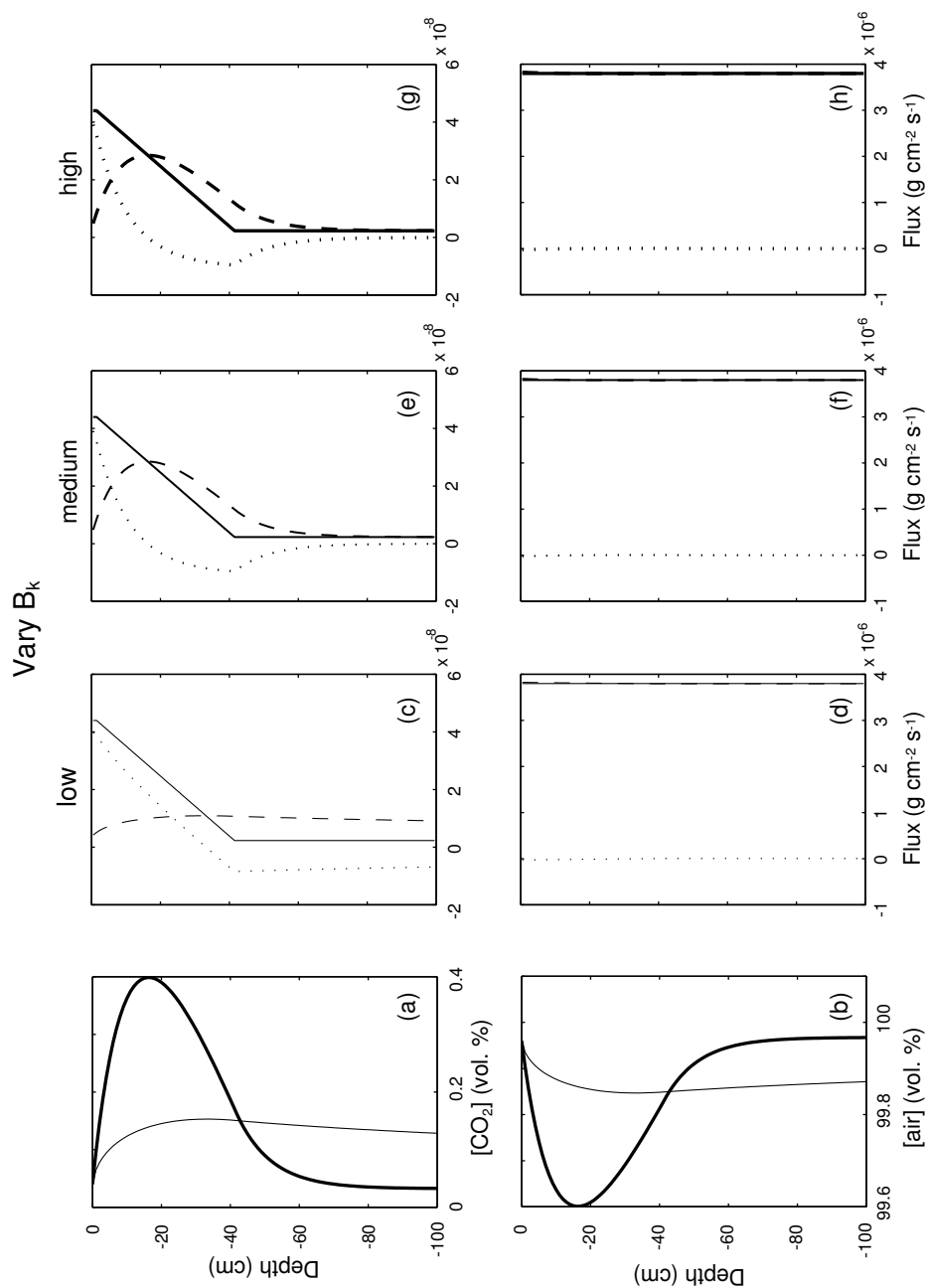


Fig. 29. Effect of varying soil permeability, B_k , on (a) $[\text{CO}_2]$ and (b) $[\text{air}]$ profile shape and (c-h) magnitude of total, advective, and diffusive CO_2 and air fluxes through soil column (see Figure 28 for complete figure explanation).

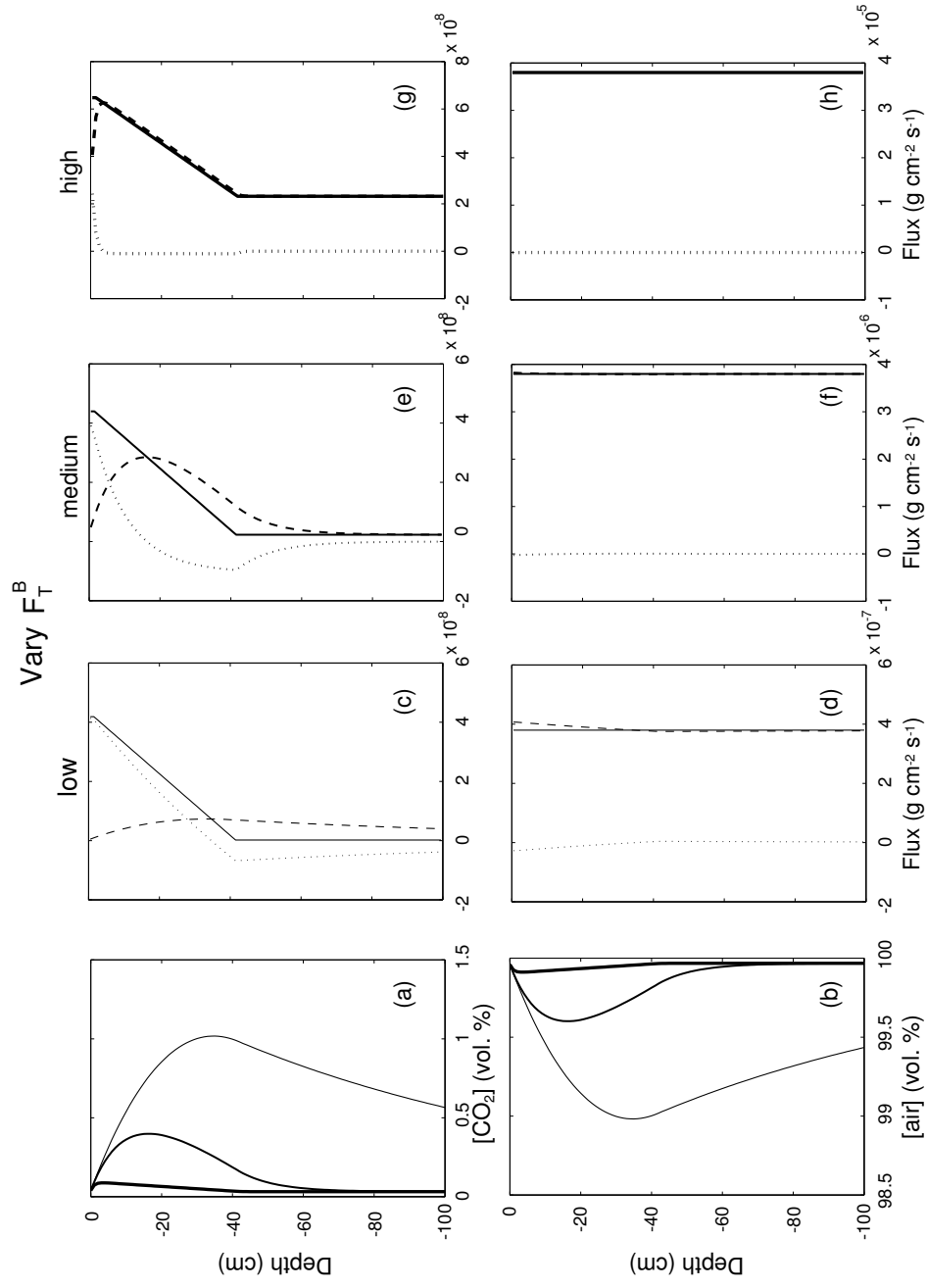


Fig. 30. Effect of varying total basal gas flux, F_T^B , on soil (a) $[\text{CO}_2]$ and (b) $[\text{air}]$ profile shape and (c-h) magnitude of total, advective, and diffusive CO_2 and air fluxes through soil column (see Figure 28 for complete figure explanation).

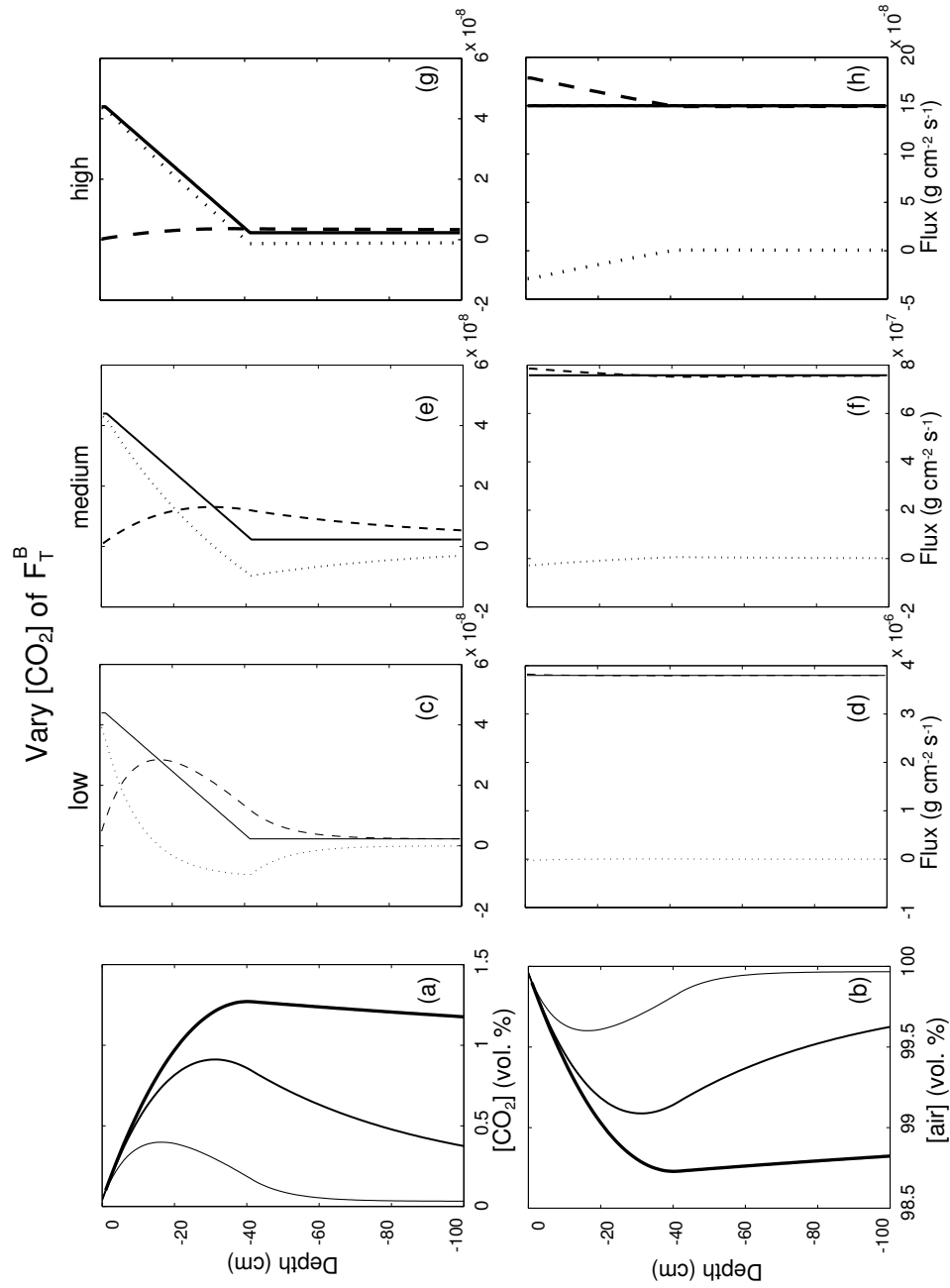


Fig. 31. Effect of varying $[\text{CO}_2]$ of F_T^B on (a) $[\text{CO}_2]$ and (b) $[\text{air}]$ concentration profile shape and (c-h) magnitude of total, advective, and diffusive CO_2 and air fluxes through soil column (see Figure 28 for complete figure description).

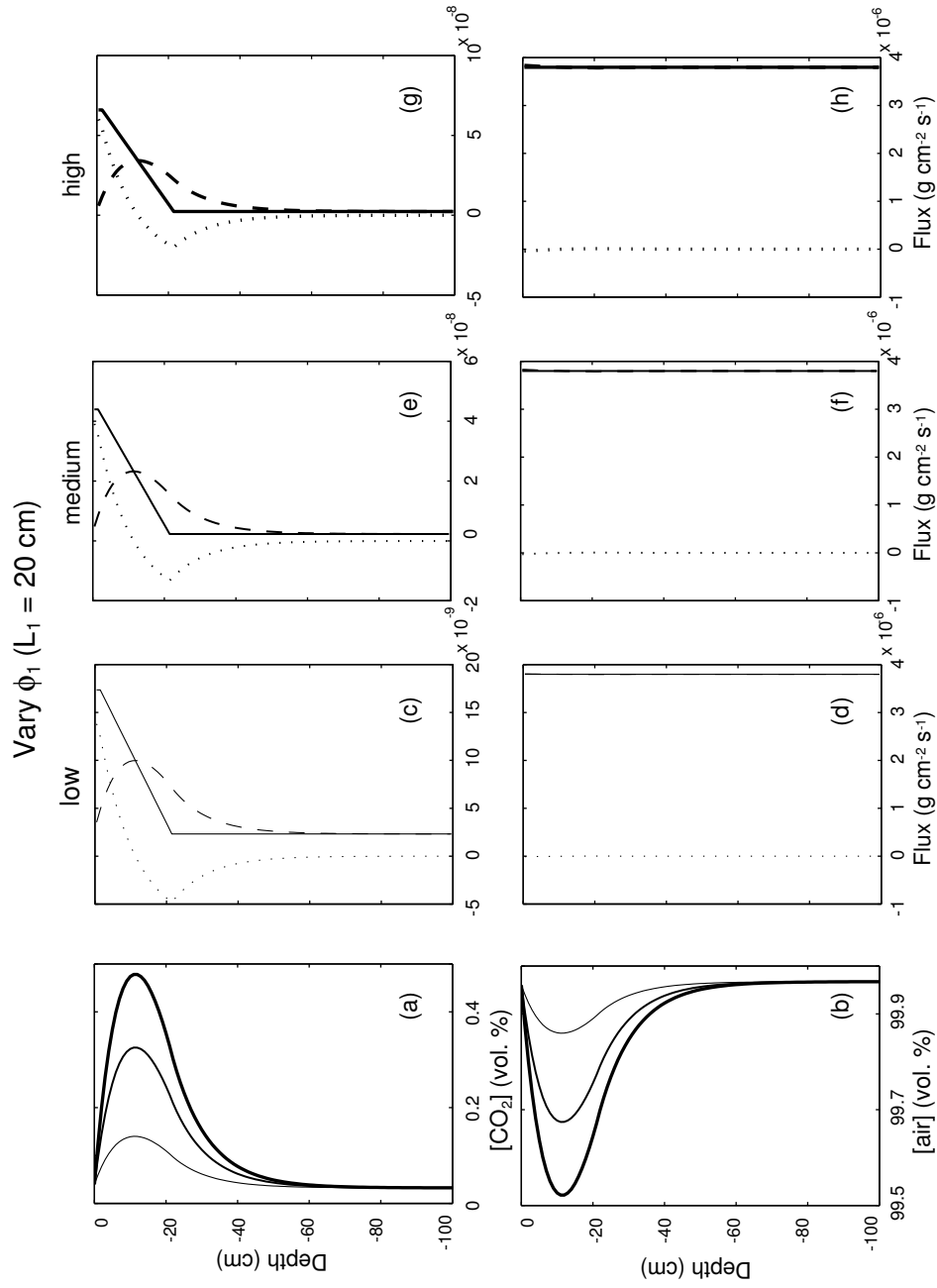


Fig. 32. Effect of varying soil CO₂ production rate within the upper soil layer, ϕ_1 , for thickness of this layer $L_1=20$ cm on soil (a) $[CO_2]$ and (b) $[air]$ profile shape and (c-h) magnitude of total, advective, and diffusive CO₂ and air fluxes through soil column (see Figure 28 for complete figure explanation).

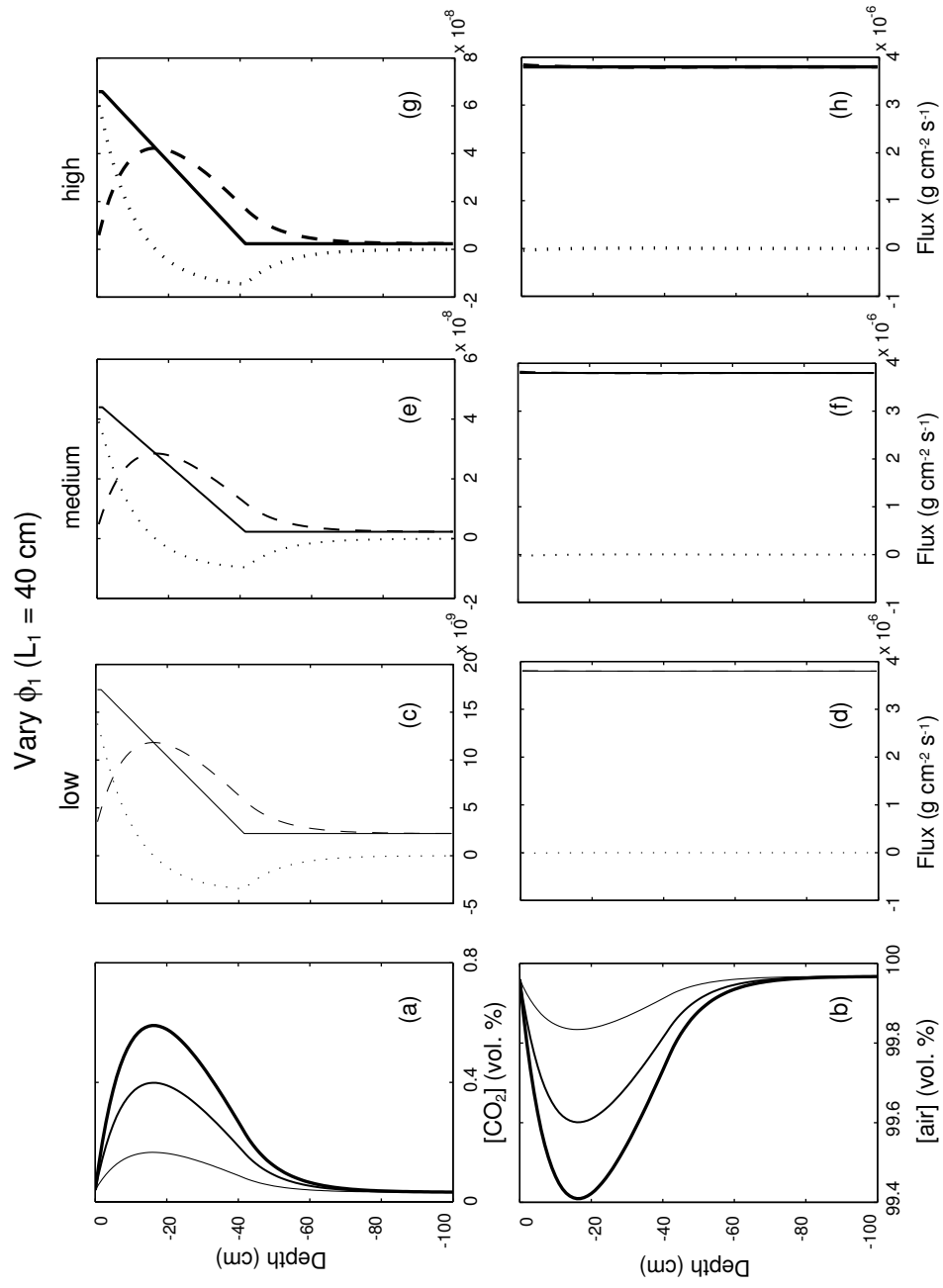


Fig. 33. Effect of varying ϕ_1 for $L_1 = 40$ cm on (a) $[\text{CO}_2]$ and (b) $[\text{air}]$ profile shape and (c-h) magnitude of total, advective, and diffusive CO_2 and air fluxes through soil column (see Figure 28 for complete figure explanation).

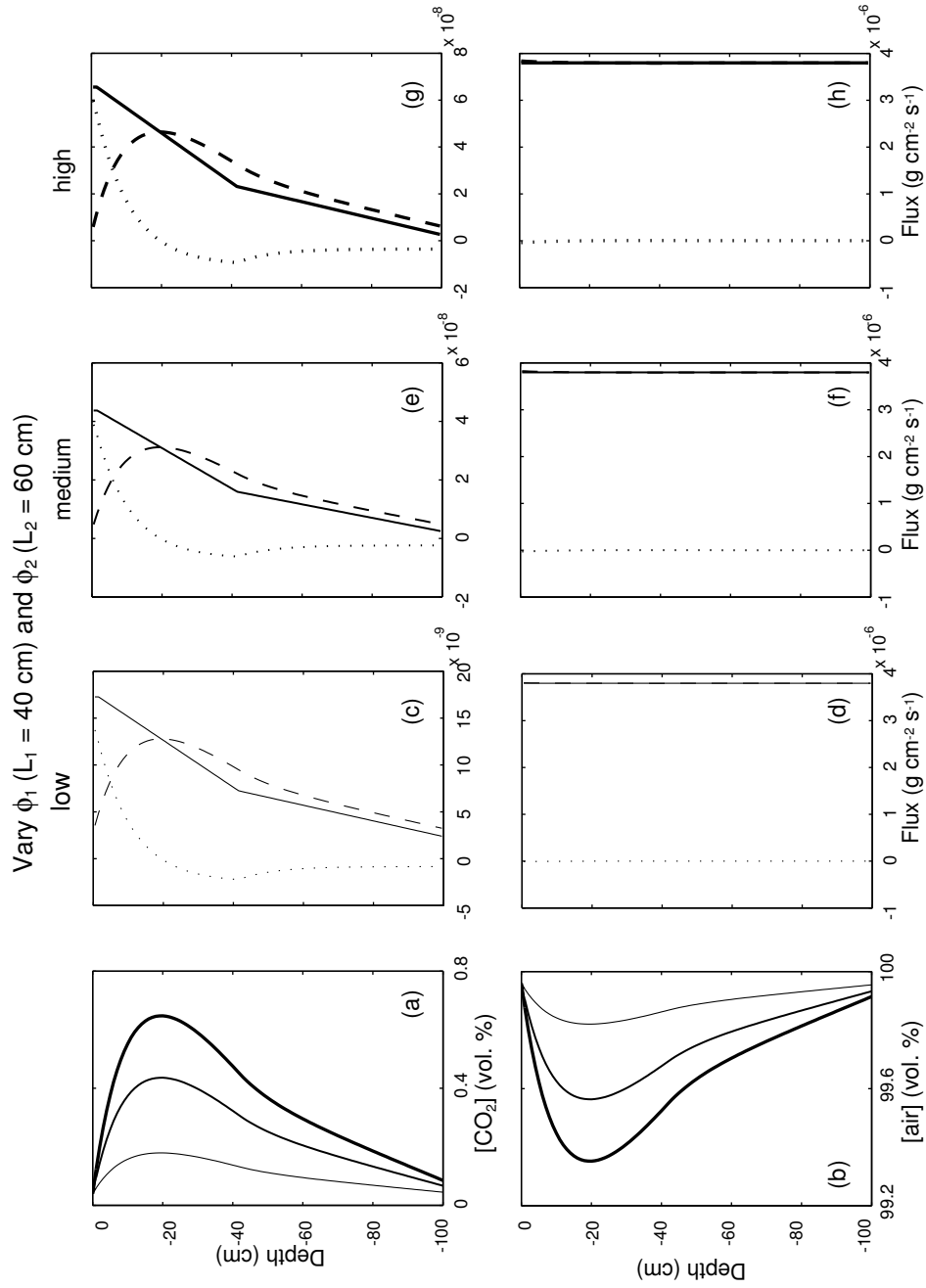


Fig. 34. Effect of varying ϕ_1 for $L_1=40$ cm and ϕ_2 for $L_2=60$ cm on soil (a) [CO₂] and (b) [air] profile shape and (c-h) magnitude of total, advective, and diffusive CO₂ and air fluxes through soil column (see Figure 28 for complete figure explanation).

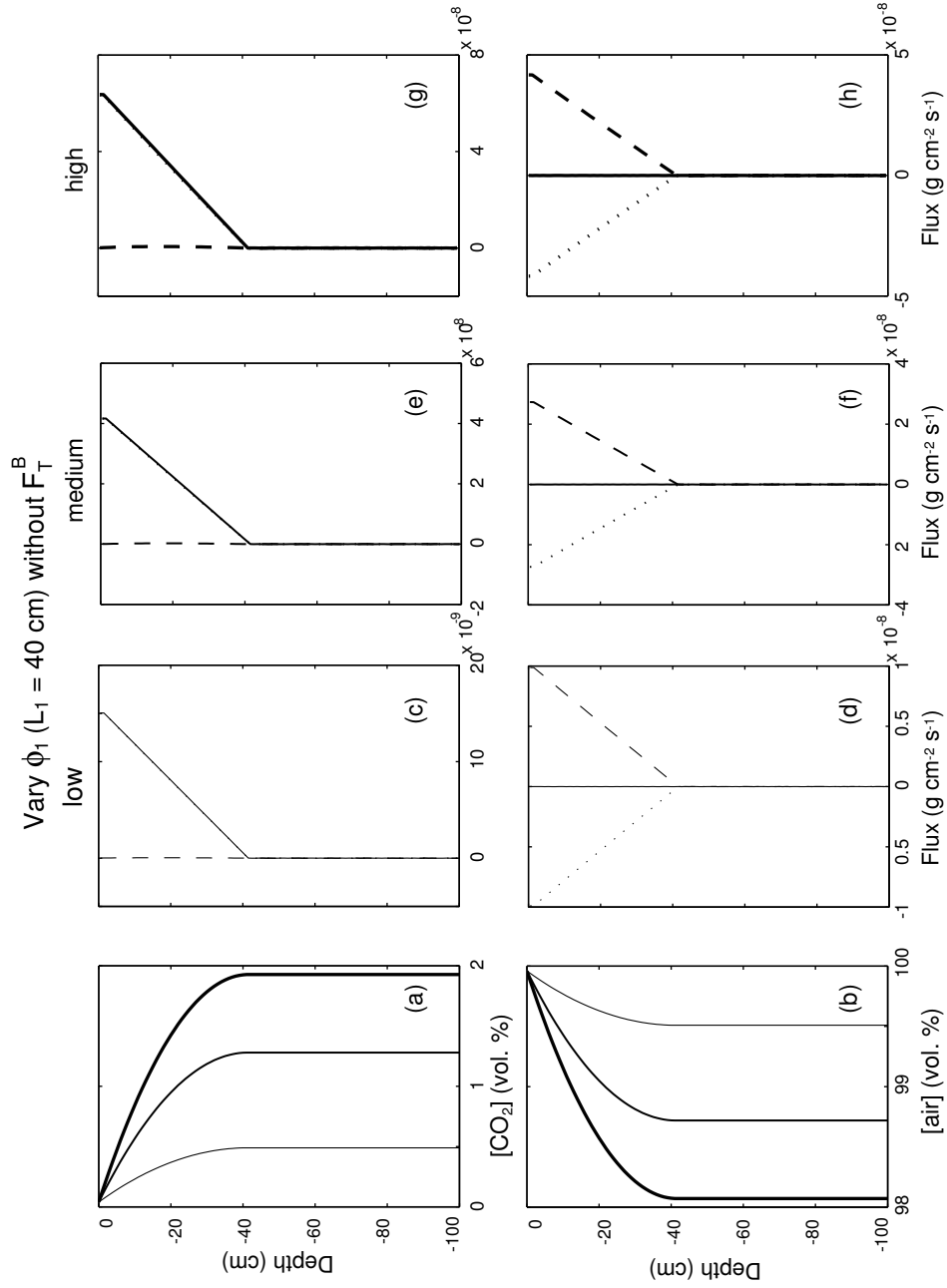


Fig. 35. Effect of varying ϕ_1 for $L_1 = 40$ cm in the absence of F_T^B on (a) $[\text{CO}_2]$ and (b) $[\text{air}]$ profile shape and (c-h) magnitude of total, advective, and diffusive CO_2 and air fluxes through soil column (see Figure 28 for complete figure explanation).

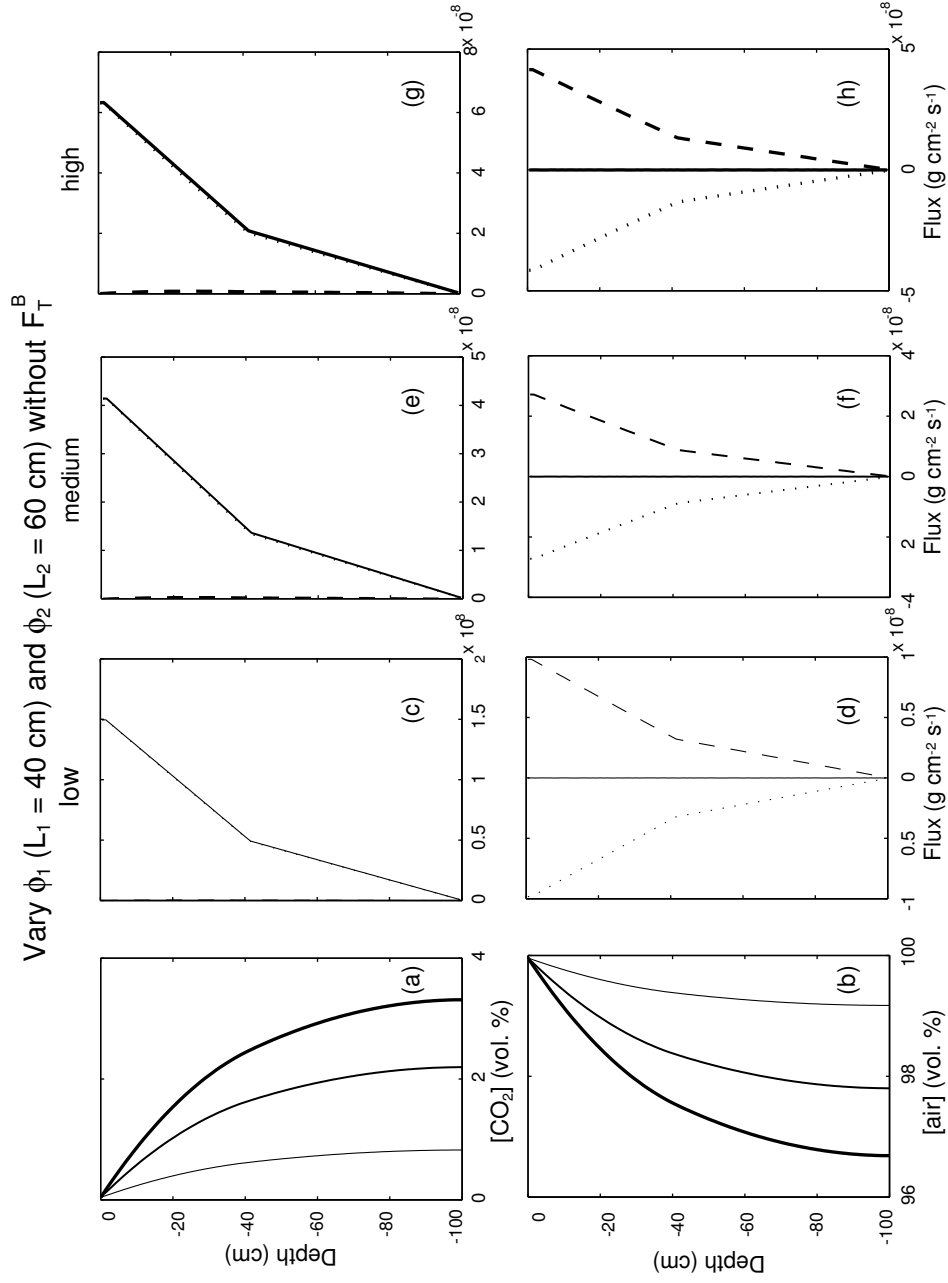


Fig. 36. Effect of varying ϕ_1 for $L_1=40$ cm and ϕ_2 for $L_2=60$ cm (without F_T^B) on soil (a) $[\text{CO}_2]$ and (b) $[\text{air}]$ profile shape and (c-h) magnitude of total, advective, and diffusive CO_2 and air fluxes through soil column (see Figure 28 for complete figure explanation).

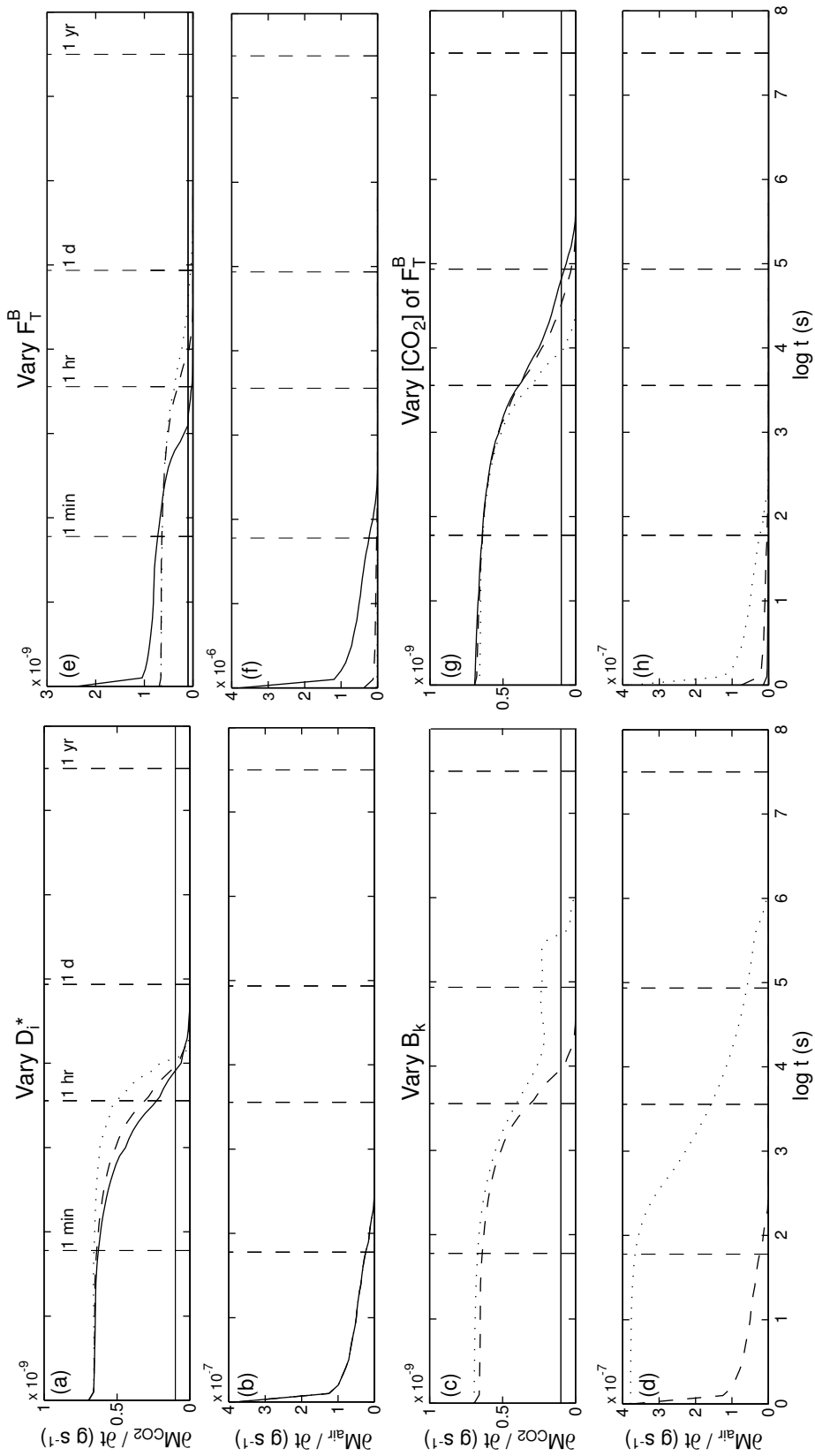


Fig. 37. Average rate of change of mass of gas i in two-component advection-diffusion model domains ($\partial M_i / \partial t$) as a function of model run time t . (a) and (b) Soil D_i^* was varied. (c) and (d) Soil B_k was varied. (e) and (f) F_T^B was varied. (g) and (h) $[\text{CO}_2]$ of F_T^B was varied. Dotted, dashed, and solid lines represent low, medium, and high parameter values, respectively. Response times for soil $[\text{CO}_2]$ and $[\text{air}]$ profiles are shown when $\partial M_{\text{CO}_2} / \partial t = 10^{-10} \text{ g s}^{-1}$ (solid horizontal lines). See text for complete model descriptions.

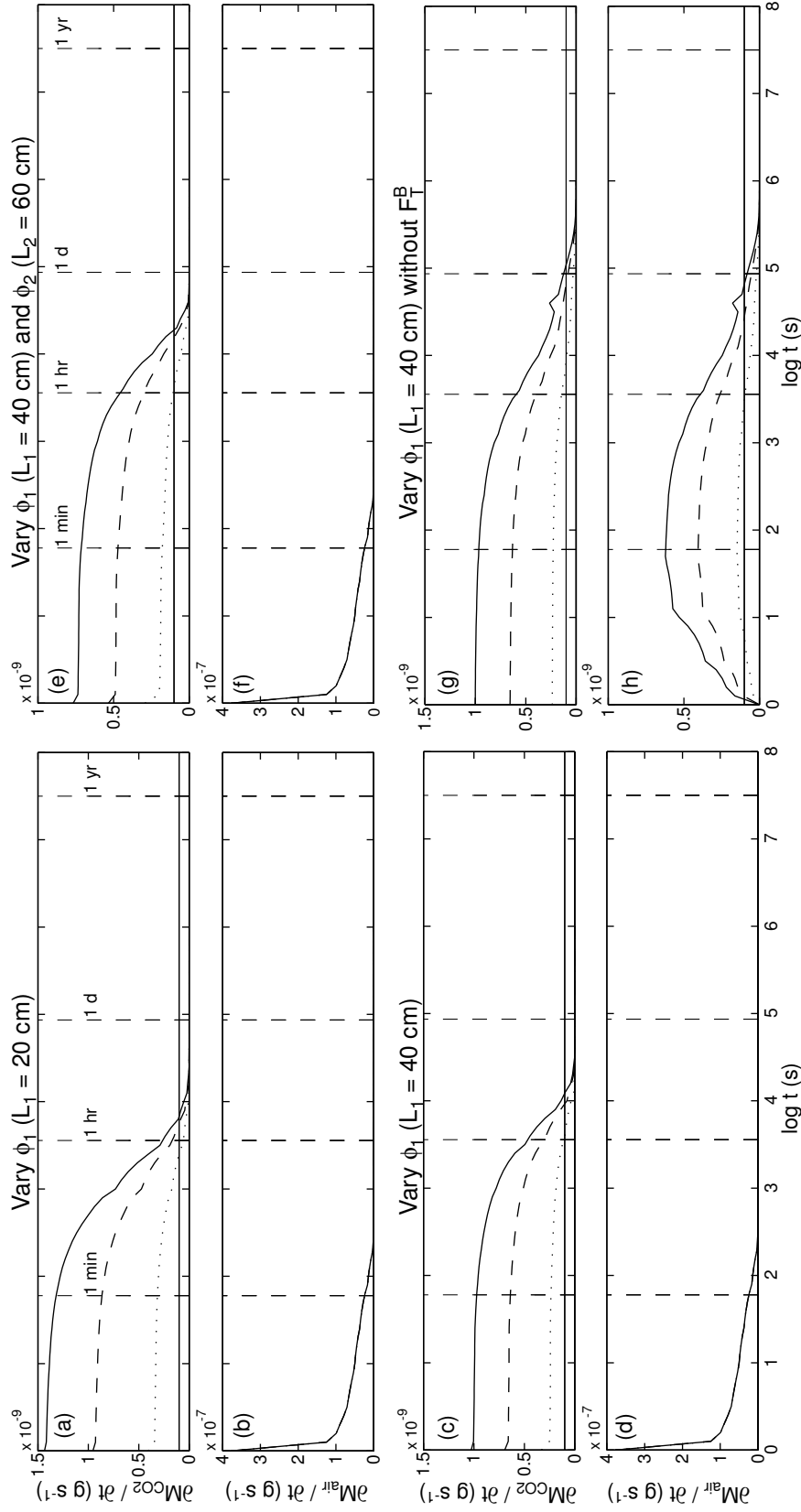


Fig. 38. Average rate of change of mass of gas i in two-component advection-diffusion model domains ($\partial M_i / \partial t$) as a function of model run time t . (a) and (b) ϕ_1 for $L_1 = 20$ cm was varied. (c) and (d) ϕ_1 for $L_1 = 40$ cm was varied. (e) and (f) ϕ_1 for $L_1 = 40$ cm and ϕ_2 for $L_2 = 60$ cm were varied. (g) and (h) ϕ_1 for $L_1 = 40$ cm without F_T^B was varied. Dotted, dashed, and solid lines represent low, medium, and high parameter values, respectively. Response times for soil $[\text{CO}_2]$ and $[\text{air}]$ profiles are shown when $\partial M_{\text{CO}_2} / \partial t = 10^{-10} \text{ g s}^{-1}$ (solid horizontal lines). See text for complete model descriptions.

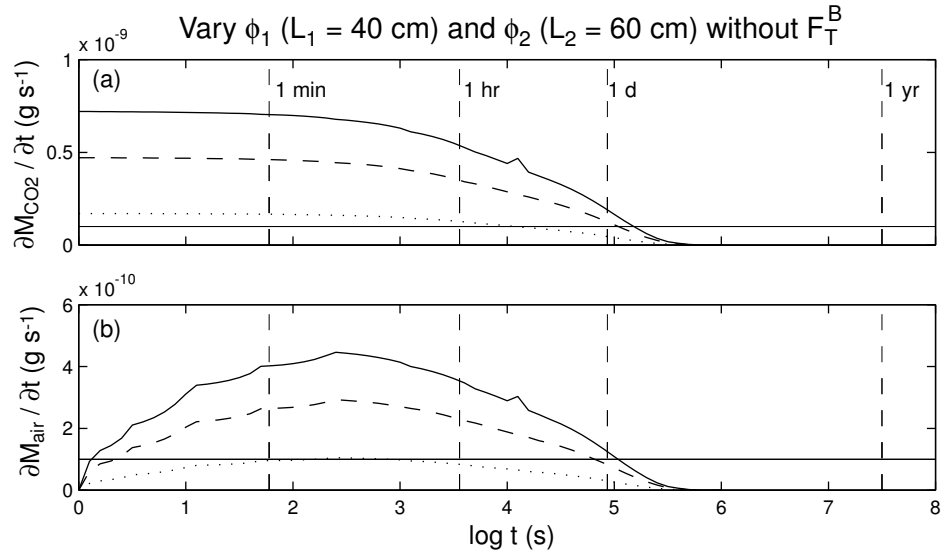


Fig. 39. Average rate of change of mass of gas i in two-component advection-diffusion model domains ($\partial M_i / \partial t$) as a function of model run time t . (a) and (b) ϕ_1 for $L_1 = 40$ cm and ϕ_2 for $L_2 = 60$ cm were varied without F_T^B . Dotted, dashed, and solid lines represent low, medium, and high parameter values, respectively. Response times for soil $[CO_2]$ and $[air]$ profiles are shown when $\partial M_{CO_2} / \partial t = 10^{-10} g\ s^{-1}$ (solid horizontal lines). See text for complete model descriptions.

References

- Abriola, L. M., C.-S. Fen, and W. W. Reeves, *Proc. Int. Assoc. Hydrol. Conf. Subsurf. Contamin. Immisc. Fluids*, chap. Numerical simulation of unsteady organic vapor transport in porous media using the dusty gas model, A. A. Balkema, Rotterdam, Netherlands, 1992.
- Amundson, R. G., and E. A. Davidson, Carbon dioxide and nitrogeneous gases in the soil atmosphere, *J. Geochem. Explor.*, *38*, 13–41, 1990.
- Bakun, W. H., and A. G. Lindh, The Parkfield, California earthquake experiment, *Science*, *229*, 619–624, 1985.
- Barnes, I., W. P. Irwin, and D. E. White, Global distribution of carbon dioxide discharges and major zones of seismicity, *U.S. Geological Survey, Water Resources Investigations*, *78-39*, 1–12, 1978.
- Bird, R. B., W. E. Stewart, and E. N. Lightfoot, *Transport phenomena*, John Wiley, New York, 1960.
- Bredehoeft, J. D., and S. E. Ingebritsen, *The role of fluids in the crust*, chap. Degassing of carbon dioxide as a possible source of high pore fluid pressures in the crust, National Academy Press, Washington, D.C., 1990.
- Byerlee, J., Friction, overpressure, and fault normal compression, *Geophys. Res. Lett.*, *17*, 2109–2112, 1990.
- Cerling, T. E., D. K. Solomon, J. Quade, and J. R. Bowman, On the isotopic composition of carbon in soil carbon dioxide, *Geochim. Cosmochim. Acta*, *55*, 3403–3405, 1991.

- Chen, C., D. M. Thomas, and R. E. Green, Modeling of radon transport in unsaturated soil, *J. Geophys. Res.*, *100*, 15,517–15,525, 1995.
- Chiodini, G., G. R. Cioni, M. Guidi, B. Raco, and L. Marini, Soil CO₂ flux measurements in volcanic and geothermal areas, *Appl. Geochem.*, *5*, 543–552, 1998.
- Ciotoli, G., M. Guerra, S. Lombardi, and E. Vittori, Soil gas survey for tracing seismogenic faults: A case study in the Fucino basin, central Italy, *J. Geophys. Res.*, *103*, 23,781–23,794, 1998.
- Cook, T. D., *Soil survey of Monterey County, California*, National Cooperative Soil Survey, Washington, D. C., 1978.
- David, M., *Geostatistical ore reserve estimation*, Elsevier, New York, 1977.
- Davidson, G. R., The stable isotopic composition and measurement of carbon in soil CO₂, *Geochim. Cosmochim. Acta*, *59*, 2485–2489, 1995.
- DeJong, E., and H. J. V. Schappert, Calculation of soil respiration and activity from CO₂ profiles in the soil, *Soil Sci.*, *113*, 328–333, 1972.
- Dörr, H., and K. O. Münnich, Carbon-14 and carbon-13 in soil CO₂, *Radiocarbon*, *22*, 909–918, 1980.
- Dörr, H., and K. O. Münnich, Annual variation in soil respiration in selected areas of the temperate zone, *Tellus*, *39B*, 114–121, 1987.
- Duddridge, G. A., P. Grangier, and E. M. Durrance, Fault detection using soil gas geochemistry, *Q. J. Eng. Geol.*, *24*, 427–435, 1991.

- Etiope, G., Subsoil CO₂ and CH₄ and their advective transport from faulted grassland to the atmosphere, *J. Geophys. Res.*, *104*, 16,889–16,894, 1999.
- Evans, W. C., M. L. Sorey, B. M. Kennedy, D. A. Stonestrom, J. D. Rogie, and D. L. Shuster, High CO₂ emissions through porous media: transport mechanisms and implications for flux measurement and fractionation, *Chem. Geol.*, *177*, 15–29, 2001.
- Finney, D. J., On the distribution of a variate whose logarithm is normally distributed, *J. Royal Statist. Soc. Suppl.*, *7*, 144–161, 1941.
- Freeze, R. A., and J. A. Cherry, *Groundwater*, Prentice Hall, Englewood Cliffs, 1979.
- Gaudinski, J. B., S. E. Trumbore, E. A. Davidson, and S. Zheng, Soil carbon cycling in a temperate forest: radiocarbon-based estimates of residence times, sequestration rates and partitioning of fluxes, *Biogeochem.*, *51*, 33–69, 2000.
- Glinski, J., and W. Stepniewski, *Soil aeration and its role for plants*, CRC Press, Inc., Boca Raton, 1985.
- Holford, D. J., S. D. Schery, J. L. Wilson, and F. M. Phillips, Modeling radon transport in dry, cracked soil, *J. Geophys. Res.*, *98*, 567–580, 1993.
- Irwin, W. P., and I. Barnes, Effect of geologic structure and metamorphic fluids on seismic behavior of the San Andreas fault system in central and northern California, *Geology*, *3*, 713–716, 1975.
- Johnson, P. A., and T. McEvilly, Parkfield seismicity: Fluid-driven?, *J. Geophys. Res.*, *100*, 12,937–12,950, 1995.

- Kennedy, B. M., Y. K. Kharaka, W. C. Evans, A. Ellwood, D. J. DePaolo, J. Thordsen, G. Ambats, and R. H. Mariner, Mantle fluids in the San Andreas fault system, *Science*, *278*, 1278–1281, 1997.
- Kharaka, Y. K., J. J. Thordsen, and W. C. Evans, *Geochemistry of the Earth's Surface*, chap. CO₂ of mantle and crustal origins in the San Andreas fault system, California, Balkeema, Rotterdam, Netherlands, 1999.
- King, C.-Y., Gas geochemistry applied to earthquake prediction: an overview, *J. Geophys. Res.*, *91*, 12,269–12,281, 1986.
- King, C.-Y., W. Zhang, and B. King, Radon anomalies on three kinds of faults in California, *Pageoph.*, *141*, 111–124, 1993.
- King, C.-Y., B.-S. King, W. C. Evans, and W. Zhang, Spatial radon anomalies on active faults in California, *Appl. Geochem.*, *11*, 497–510, 1996.
- Klusman, R. W., *Soil gas and related methods for natural resource exploration*, John Wiley, New York, 1993.
- Klute, A., and A. L. Page (Eds.), *Methods of Soil Analysis*, Soil Science Society of America, Madison, Wis., 1986.
- Koepnick, K. W., S. L. Brantley, J. M. Thompson, G. L. Rowe, A. A. Nyblade, and C. Moshy, Volatile emissions from the crater and flank of Oldoinyo Lengai volcano, Tanzania, *J. Geophys. Res.*, *101*, 13,819–13,830, 1996.
- Levin, I., and B. Kromer, Twenty years of atmospheric ¹⁴CO₂ observations at Schauinsland Station, Germany, *Radiocarbon*, *39*, 205–218, 1997.

- Lewicki, J. L., and S. L. Brantley, CO₂ degassing along the San Andreas fault, Parkfield, California, *Geophys. Res. Lett.*, *27*, 5–8, 2000.
- Lewicki, J. L., W. C. Evans, G. E. Hilley, M. L. Sorey, J. D. Rogie, and S. L. Brantley, Soil gas transport along the San Andreas fault, Parkfield, CA: field observations and numerical modeling, *Eos Trans. AGU*, *82*, 2001.
- Lewicki, J. L., W. C. Evans, G. E. Hilley, M. L. Sorey, J. D. Rogie, and S. L. Brantley, Soil CO₂ flow in fractured terrain I: observations from the San Andreas and Calaveras faults, CA, *J. Geophys. Res.*, in review.
- Marrero, T. R., and E. A. Mason, Gaseous diffusion coefficients, *J. Phys. Chem. Ref. Data*, *1*, 3–118, 1972.
- Massmann, J., and D. Farrier, Effects of atmospheric pressures on gas transport in the vadose zone, *Water Resour. Res.*, *28*, 777–791, 1992.
- Norman, J. M., R. Garcia, and S. B. Verma, Soil surface CO₂ fluxes and the carbon budget of a grassland, *J. Geophys. Res.*, *97*, 18,845–18,853, 1992.
- Ohmoto, H., and R. Rye, *Geochemistry of hydrothermal ore deposits*, chap. Isotopes of sulfur and carbon, John Wiley and Sons, New York, 1979.
- O’Leary, M. H., Carbon isotopes in photosynthesis, *Bioscience*, *38*, 328–336, 1988.
- Osozawa, S., and S. Hasegawa, Diel and seasonal changes in carbon dioxide concentration and flux in an andisol, *Soil Sci.*, *160*, 117–124, 1995.
- Ouyang, Y., and C. Zheng, Surficial processes and CO₂ flux in soil ecosystem, *J. Hydrol.*, *234*, 54–70, 2000.

- Penman, H. L., Gas and vapor movements in the soil. i. The diffusion of vapors through porous solids, *J. Agr. Sci.*, *30*, 437–462, 1940a.
- Penman, H. L., Gas and vapor movements in the soil. ii. The diffusion of carbon dioxide through porous solids, *J. Agr. Sci.*, *30*, 570–581, 1940b.
- Pinault, J.-L., and J.-C. Baubron, Signal processing of soil gas radon, atmospheric pressure, moisture, and soil temperature data: a new approach for radon concentration modeling, *J. Geophys. Res.*, *101*, 3157–3171, 1996.
- Pineau, F., and M. Javoy, Carbon isotopes and concentrations in mid-oceanic ridge basalts, *Earth Planet. Sci. Lett.*, *62*, 239–257, 1983.
- Raich, J. W., and W. H. Schlesinger, The global carbon dioxide flux in soil respiration and its relationship to vegetation and climate, *Tellus*, *44B*, 81–99, 1992.
- Reimer, G. M., Use of soil-gas helium concentrations for earthquake prediction: limitations imposed by diurnal variation, *J. Geophys. Res.*, *85*, 3107–3114, 1980.
- Rice, J. R., *Fault mechanics and transport properties of rocks*, chap. Fault stress states, pore pressure distributions, and the weakness of the San Andreas fault, Academic Press, San Diego, 1992.
- Rogie, J. D., D. M. Kerrick, M. L. Sorey, G. Chiodini, and D. L. Galloway, Dynamics of carbon dioxide emission at Mammoth Mountain, California, *Earth Planet. Sci. Lett.*, *188*, 535–541, 2001.
- Scanlon, B. R., J. P. Nicot, and J. M. Massmann, *Handbook of Soil Science*, chap. Soil Gas Movement in Unsaturated Systems, CRC Press, New York, 1999.

- Schery, S. D., and D. Siegel, The role of channels in the transport of radon from the soil, *J. Geophys. Res.*, *91*, 12,366–12,374, 1986.
- Schery, S. D., D. H. Gaeddert, and M. H. Wilkening, Factors affecting exhalation of radon from a gravelly sandy loam, *J. Geophys. Res.*, *89*, 7299–7309, 1984.
- Shampine, L. F., and M. K. Gordon, *Computer Solution of Ordinary Differential Equations: the Initial Value Problem*, W. H. Freeman, San Francisco, 1975.
- Sichel, H. S., New methods in the statistical evaluation of mine sampling, *London Inst. Mining Met. Trans.*, *61*, 261–288, 1952.
- Sleep, B. E., and J. F. Skyes, Modeling the transport of volatile organics in variably saturated media, *Water Resour. Res.*, *25*, 81–92, 1989.
- Sorey, M. L., W. C. Evans, B. M. Kennedy, C. D. Farrar, L. J. Hainsworth, and B. Hausback, Carbon dioxide and helium emissions from a reservoir of magmatic gas beneath Mammoth Mountain, California, *J. Geophys. Res.*, *103*, 15,303–15,323, 1998.
- Southon, J. R., et al., Progress in AMS measurements at the LLNL spectrometer, *Radiocarbon*, *34*, 473–477, 1992.
- Terzaghi, K., and R. B. Peck, *Soil mechanics in engineering science*, John Wiley, New York, 1968.
- Thorstenson, D. C., and D. W. Pollock, Gas transport in unsaturated zones: multi-component systems and the adequacy of Fick's laws, *Water Resour. Res.*, *25*, 477–507, 1989.

- Toutain, C.-Y., and B.-S. Baubron, Gas geochemistry and seismotectonics: a review, *Tectonophys.*, *304*, 1–27, 1999.
- Unsworth, M. J., P. Malin, G. Egbert, and J. Booker, Internal structure of the San Andreas fault at Parkfield, California, *Geology*, *25*, 359–362, 1997.
- Wood, B. D., C. K. Keller, and D. L. Johnstone, Carbon dioxide as a measure of microbial activity in the unsaturated zone, *Water Resour. Res.*, *29*, 647–659, 1993.
- Zoback, M. D., et al., New evidence on the state of stress of the San Andreas fault system, *Science*, *238*, 1105–1111, 1987.

Vita

Jennifer L. Lewicki

Jennifer L. Lewicki was born in Stamford, Connecticut on December 13, 1971. She is the daughter of John and Marilyn Lewicki. She attended Hamilton College from 1990 to 1994 where she completed a thesis titled "Mineralogical and Geochemical Variation in Andesites from Imbabura and Puluagua Volcanoes, Northern Ecuador" with Professor David Bailey and received the B.A. degree in Geology, *cum laude*. Jennifer attended Arizona State University from 1995 to 1997 where she completed a thesis titled "Geochemical and Isotopic Variation in Fumarolic Gases and Thermal Waters from Cumbal Volcano, Colombia" with Professor Stanley Williams and received the M. S. degree in Geology. In 1998, she enrolled in the Ph. D. program in Geosciences at The Pennsylvania State University and from 1998 to 2002 worked with Professor Susan Brantley in the Department of Geosciences. From 1998 to 1999, she was employed in the Department of Geosciences as a teaching assistant. In 2000, she was a visiting instructor in the Department of Geology at Bucknell University. Jennifer received a NASA Earth System Science Fellowship in 1999 and from 1999 to 2002 was a research fellow at Penn State. During her graduate career, she conducted research in the areas of volcano gas and thermal water geochemistry, measurement and interpretation of CO₂ fluxes from faulted and volcanically active areas, and unsaturated zone gas transport, published several refereed journal articles on these subjects, and presented her research at national and international professional meetings.